

# Modeling biochemical reaction networks in complex intracellular environments

Présentée le 9 octobre 2020

à la Faculté des sciences de base  
Laboratoire de biotechnologie computationnelle des systèmes  
Programme doctoral en chimie et génie chimique

pour l'obtention du grade de Docteur ès Sciences

par

**Daniel Robert WEILANDT**

Acceptée sur proposition du jury

Prof. A.-C. Corminboeuf, présidente du jury  
Prof. V. Hatzimanikatis, Prof. B. Fierz, directeurs de thèse  
Prof. I. Sbalzarini, rapporteur  
Prof. R. Grima, rapporteur  
Prof. B. Smit, rapporteur



# Acknowledgements

Writing these acknowledgments after four years of working and learning as a Ph.D. student, I come to realize that over my whole academic life, numerous people contributed to the completion of this thesis.

First and foremost, I wish to thank Prof. Vassily Hatzimanikatis for being a great advisor and mentor. He taught me how to identify critical problems and address those by thinking in a complex and non-linear way. I am grateful for both the freedom and guidance he provided me throughout the entire period of my Ph.D., allowing me to grow both as a person and scientist. Thank you, Vassily, for an inspiring Ph.D., your trust, critique, and most of all, for believing in me.

I also want to thank Prof. Beat Fierz for his co-supervision and mentorship. I always enjoyed our insightful discussions about science and politics. Our collaboration taught me a great deal about the challenges and opportunities at the interface of computational and experimental science.

Next, I want to express my gratitude to the members of my Ph.D. thesis committee: Prof. Anne-Clémence Corminboeuf, Prof. Ivo F. Sbalzarini, Prof. Ramon Grima, and Prof. Berend Smit. Thank you for your efforts to make this thesis defense happen despite a global pandemic and other complications, for the insightful review of my thesis and valuable feedback. They all made my thesis defense and the following discussion and enjoyable and inspiring experience. I especially want to thank Prof. Corminboeuf as president of the committee for handling the complicated situation with confidence and determination.

At this point, I also want to thank all the teachers and professors supporting me throughout this journey. I want to issue a special thank you to Prof. Harald Mandel, Dr. David Kauzlaric, and Dr. Andreas Greiner for their support during the application process for this very position.

An exceptional thanks to Maria and Pierre for being incredible friends throughout my Ph.D.

## Acknowledgements

---

and having an open ear when frustration was high and for epic nights out in Lausanne. Thank you, Maria, for always having time for a decompressing coffee break for all the listening and all the talking. Thank you, Pierre, for having that twisted, non-differentiable humor making for incredible conversations with continuous laughs and making all times, fun times.

I also want to thank all the other members of LCSB, especially Misko, Robin, and Georgios Fengos, with whom I had the honor to work on kinetic models. Thank you for your valuable comments and inspiring discussions. And thank you, Robin, for all the off-topic break discussions on vehicle engineering they were fun trips back to my mechanical engineering times. Another thank you goes out to Homa and Zahleh for their contagious positivity and their support on many of the different side projects. I cannot forget to thank Sophia and our discussion on Musicals and our nostalgic video game history. Also, I want to thank Anush for her support and hospitality during my Postdoc applications. Likewise, thank you to my long term office mates Jasmin and Noushin. Thank you for fun times, messing around, and making not too much fun about me stressing out on the small things in life. Including a wholehearted thank you to all the remaining people of the LCSB family to Evangelia, Anastasia, Liliana, Joana, Meric, Tiziano, Yves, Stepan, Vikash, Milenko, Tuure, Omid, and Georgios Savoglidis. Thank you for being incredible colleagues in- and outside the office. I also want to thank my first master students Asli, Remi that did incredible work during their Master theses. It was and still is a pleasure working with you. A special thank you also to Christine Kupper for her advice, administrative support, and her efforts in maintaining the coffee supply for two labs.

Another thank you goes out to the people from the LBCM, especially my coauthors Lousie, Andreas, Sinan, and Carolin, as well as to Nora. She helped me find my way into the world of chromatin and nucleosomes.

Eventually, I want to thank my family, to all my brothers and sisters, Simon, Christoph, Miriam, Johanna, Isabel, and Lea, my mother and father, my grandmothers Grete and Renate, and my aunt Sabine and my uncle Axel and my cousin Oliver. Thank you, dear siblings, for all the late-night discussions on engineering, philosophy, and society. Thank you, mum and dad, for always fighting for my childhood opportunities even when it was always not easy. Thank you, Renate and Grete, for your love and care throughout the years, I am glad to have you still with me. Thank you, Sabine, for the experience of another way of life and showing me that the world is much bigger than Karlsruhe. Axel, thank you for being an academic role model in our family. Oliver, thank you for your support and hospitality to leave the old continent for the first time and experience a different world.

## Acknowledgements

---

Finally, I want to thank my dear girlfriend, Friederike, for always believing in me even when I was not. Thank you for your love, patience, and all the fun times we have while discovering the world near and far.

*Lausanne, May 21, 2020*

D. R. Weilandt

PS: Funding for this work was generously provided by the European Union's Horizon 2020 research and innovation program under grant agreement numbers 686070 and 814408.



# Abstract

Whether one aims to design treatments for diseases such as cancer or diabetes, engineer cells to produce valuable biochemicals sustainably, or to grasp the behavior of living organisms, it is essential to understand how cells react to genetic, environmental, and biochemical perturbations. Responses of living systems to such perturbations are tied to the dynamics of the biochemical networks implementing the various biological functions necessary for its survival. Thus, knowledge about the dynamics of these biochemical networks is crucial to understand how living entities react to changes in their environment, genes, or biochemistry. The environment within cells is filled with proteins, lipids, polysaccharides, RNA, and DNA, creating various kinds of structures such as droplets, aggregates, and filaments and occupying up to 40% of the intracellular volume. Many of the reactions within the biochemical reaction networks can only be studied in detail when isolated from the intracellular environment. Interaction of the reactants with these structures and other molecules within the cellular volume affects the dynamics properties of the biochemical reactions. The data obtained from experiments that measure the reaction dynamics isolated from the intracellular environment in a dilute setup, omit the effects originating from the interactions with this complex intracellular environment. This discrepancy can result in misinformed models unable to capture the cellular responses. Theoretical and computational models can provide insight into how the reaction kinetics is altered due to the structures inside the cell.

In this thesis, we studied the behavior of reactions confined to different structures inside the cell. Therefore, we focused our efforts on the dynamic capture of chromatin-binding proteins as well as the effects of macromolecular crowding on enzyme kinetics and enzyme reaction networks. Firstly, we used computational modeling and parameter estimation methods to identify the binding mechanism of a heterochromatin effector protein binding to a posttranslational modification mark. We then identified the key parameters of this binding mechanism to investigate the potential effects of the intracellular environment on the binding behavior. Secondly, we investigated the reaction kinetics of enzymes in a solution of macromolecules, such

## Abstract

---

as other enzymes, proteins, DNA, and others. We, therefore, developed a new computational framework that allowed us to parameterize approximate reaction kinetic based on particle simulations. This method allowed us to show that maximal enzyme rates and Michaelis-Menten constants are reduced up to 10 fold upon introducing macromolecules into the system. We continued the analysis of crowded enzyme kinetics by developing a new theoretical model of crowded diffusion-controlled reaction networks. We then used this model to study the role of diffusion in crowded enzyme kinetics. Thirdly, we combined the approximate kinetics with the theoretical model to investigate the impact of crowding on prototypical metabolic networks consisting of multiple enzymatic reactions. Our results suggest that crowding can have significant and unintuitive effects on the sensitivities of the reaction network, making a strong for the application of the derived methods in large scale metabolic models. Finally, we outline the path towards application-specific *in vivo* like models from the integration of reevaluated *in vitro* data.

## Keywords

Chemical kinetics, protein binding, chromatin, epigenetic factors, macromolecular crowding, enzyme kinetics, metabolic control analysis.



# Zusammenfassung

Möchte man neuartige Therapien für Krankheiten wie Krebs oder Diabetes entwickeln, Chemikalien mittels genmodifizierter Zellen nachhaltig produzieren oder das biochemische Verhalten lebender Organismen begreifen, ist es erforderlich zu verstehen, wie Zellen auf Veränderungen in ihrer Umwelt, in ihrem Genom oder auf biochemischer Ebene reagieren. Die Antwort der biochemischen Signale lebender Organismen auf solche Veränderungen ist an das dynamische Verhalten der biochemischen Interaktionen gebunden, welche die verschiedenen überlebensnotwendigen, biologischen Funktionen beinhalten. Deshalb ist das Wissen über das dynamische Verhalten dieser biochemischen Interaktionen ausschlaggebend, um zu verstehen, wie Lebewesen auf diese Veränderungen reagieren. Die Umgebung im Zellinneren ist voller Proteine, Lipide, Polysaccharide, RNA und DNA. Diese Makromoleküle formen verschiedene Strukturen, wie zum Beispiel Tröpfchen, Aggregate oder Filamente und füllen somit bis zu 40% des Zellvolumens aus. Viele der biochemischen Reaktionen innerhalb dieser Reaktionsnetzwerke können nur untersucht werden, wenn diese aus der intrazellulären Umgebung isoliert werden. Interagieren die an diesen Reaktionen beteiligten Moleküle mit den Strukturen und Makromolekülen innerhalb des Zellinneren, verändert dies die dynamischen Eigenschaften der biochemischen Reaktionen. Experimentelle Daten, die durch das Extrahieren dieser Reaktionen aus ihrer intrazellulären Umgebung, erhoben werden, vernachlässigen die Effekte, die durch die Interaktion mit dieser komplexen Umgebung stammen. Diese Diskrepanz zwischen der *in vitro* Messung und der *in vivo* Dynamik kann dazu führen, dass Modelle mit falschen Informationen gefüttert werden und nicht in der Lage sind, das komplexe Verhalten der biochemischen Interaktionen zu reproduzieren. Theoretische und informationstechnische Modelle können dabei helfen, die Veränderungen der Reaktionsdynamik innerhalb einer Zelle zu bestimmen .

In dieser Arbeit haben wir das Verhalten von biochemischen Reaktionen untersucht, bei denen die Reaktionspartner in ihrer Mobilität durch zelluläre Strukturen beschränkt sind. Dabei haben wir uns auf das Erforschen des dynamischen Verhaltens von Chromatin-bindenden

## Zusammenfassung

---

Proteinen sowie dem Untersuchen von Molecular Crowding-Effekten auf den Michaelis-Menten Mechanismus und auf Metabolische Reaktionsnetzwerke fokussiert. In einem ersten Schritt nutzen wir Computer Simulationen und Parameter Identifikationsverfahren, um den Bindungsmechanismus eines Heterochromatin-Effektor-Proteins zu charakterisieren. Anschließend haben wir die Schlüsselparameter des Bindungsmechanismus identifiziert, um die potenziellen Effekte der intrazellulären Umgebung auf das Bindungsverhalten zu analysieren. In einem zweiten Schritt untersuchen wir die Reaktionskinetik von Enzymen in einer Lösung aus Makromolekülen, wie Proteinen, Lipiden, Polysacchariden, RNA und DNA. Dafür haben wir ein neuartiges, computerbasiertes Framework geschaffen, das es uns erlaubt, approximier- te Reaktionsgeschwindigkeitsgesetze mithilfe von Partikelsimulationen zu parametrisieren. Diese Methodik erlaubt es uns zu zeigen, dass die maximale Reaktionsgeschwindigkeit und die Michaelis-Menten Konstante um das 10-fache reduziert werden, wenn Makromoleküle in das System eingebracht werden. Wir haben diese Analyse fortgesetzt und ein theoretisches Model für diffusionslimitierte Reaktionsnetzwerke mit Crowding Effekten entwickelt. Folgend konnten wir mit diesem Model das Zusammenspiel von Diffusion und Molecular Crowding-Effekten auf die Enzymkinetik analysieren. In einem nächsten Schritt kombinierten wir das approximierte Reaktionsgeschwindigkeitsgesetz mit dem theoretischen Modell, um den Einfluss von Molecular Crowding-Effekten auf prototypische Reaktionsnetzwerke zu untersuchen. Unsere Resultate zeigen, dass Crowding-Effekte zu signifikanten und unerwarteten Veränderungen der Systemsensitivitäten führen. Abschließend geben wir einen Überblick über die Aufgaben, die für die Integration von in vitro Daten in applikationsspezifische Modelle mit in vivo artigem Verhalten notwendig sind.

## Stichwörter

Chemische Reaktionsgeschwindigkeit, Protein Adsorption, Chromatin, Epigenetische-Faktoren, Molecular Crowding, Enzymkinetik, Metabolische-Kontroll-Analyse

# Contents

<b>Acknowledgements</b>	<b>i</b>
<b>Abstract (English/Deutsch)</b>	<b>v</b>
<b>List of Figures</b>	<b>xiii</b>
<b>List of Tables</b>	<b>xix</b>
<b>1 Background and Scope</b>	<b>1</b>
1.1 Confinement of biochemical reactions . . . . .	2
1.2 <i>In silico</i> reevaluation of <i>in vitro</i> data . . . . .	7
1.3 Thesis overview . . . . .	9
<b>2 Modeling of multivalent protein binding on chromatin</b>	<b>11</b>
2.1 Introduction . . . . .	11
2.2 Experimental data . . . . .	13
2.3 Mathematical model . . . . .	15
2.4 Parameter identification . . . . .	15
2.5 Stochastic simulations of protein binding <i>in vitro</i> . . . . .	20
2.6 Sensitivity analysis . . . . .	20
2.7 Discussion . . . . .	24
<b>3 Particle-based modeling of crowding effects on enzyme kinetics</b>	<b>27</b>
3.1 Introduction . . . . .	27
3.2 Modeling enzyme kinetics . . . . .	31
3.2.1 Approximation of non ideal enzyme kinetics . . . . .	31
3.2.2 Generalized elementary Michaelis-Menten kinetics . . . . .	33
3.2.3 A hard sphere model for macromolecular crowding . . . . .	36
3.2.4 Measuring effective reaction rate constants . . . . .	37
3.2.5 Modeling framework . . . . .	38

## Contents

---

3.2.6	Weighted linear regressions . . . . .	41
3.2.7	Computational details . . . . .	41
3.3	Effects of crowding on the reversible Michaelis Menten kinetics . . . . .	41
3.3.1	Validation of GEEK . . . . .	42
3.3.2	Impact of crowding on the elementary reaction level . . . . .	43
3.3.3	Effect on the Michaelis Menten parameters . . . . .	46
3.3.4	Influence of crowder size on the Michaelis Menten kinetics . . . . .	49
3.4	Discussion . . . . .	51
<b>4</b>	<b>Theoretical model of crowded kinetics</b>	<b>53</b>
4.1	Introduction . . . . .	53
4.2	Mathematical model . . . . .	55
4.2.1	Pairwise reaction-diffusion model . . . . .	56
4.2.2	Finite element model . . . . .	58
4.3	Effects of crowding on the model parameters . . . . .	61
4.3.1	Equilibrium radial distribution function . . . . .	61
4.3.2	Effective dissociation constant . . . . .	63
4.3.3	Effective diffusion constant . . . . .	67
4.4	Apparent reaction rates at equilibrium . . . . .	68
4.5	Non-equilibrium effects on steady-state reaction rates . . . . .	70
4.5.1	Elementary reactions . . . . .	71
4.5.2	Enzymatic reactions . . . . .	71
4.6	Discussion . . . . .	76
<b>5</b>	<b>Crowded metabolic control</b>	<b>79</b>
5.1	Introduction . . . . .	79
5.2	Modeling perturbations in metabolic networks . . . . .	80
5.2.1	Metabolic kinetic models . . . . .	80
5.2.2	(Log)linear formulation of Metabolic Control Analysis . . . . .	81
5.3	Introducing crowding into metabolic reaction networks . . . . .	82
5.3.1	Generalized elementary enzyme model . . . . .	82
5.3.2	An approximate model for crowded elementary reactions . . . . .	84
5.3.3	Generalized enzyme elasticities . . . . .	87
5.4	Crowded control on prototypical networks . . . . .	90
5.4.1	Linear pathway . . . . .	91
5.4.2	Branched pathway . . . . .	92

5.5 Discussion . . . . .	93
<b>6 Conclusions and Perspectives</b>	<b>97</b>
6.1 Conclusions . . . . .	97
6.2 Future perspectives . . . . .	101
6.2.1 Membrane thermodynamics and reaction kinetics . . . . .	101
6.2.2 Active processes . . . . .	102
6.2.3 Phase separation . . . . .	102
<b>A Supplementary information particle methods</b>	<b>105</b>
A.1 Measuring the bimolecular elementary rate constants . . . . .	105
A.2 Regression for GEEK parameters . . . . .	105
A.3 Validation of GEEK . . . . .	109
A.3.1 Computational details of the validation simulations . . . . .	109
A.3.2 Validation of GEEK based on hard-sphere Brownian reaction dynamics .	110
A.3.3 Validation of GEEK based on the crowder free Cichocki-Hinsen algorithm	111
A.3.4 Discussion on the results of the HSBRD and CFCH simulations . . . . .	113
<b>Bibliography</b>	<b>115</b>
<b>Curriculum Vitae</b>	<b>135</b>



# List of Figures

1.1	Illustrations of different categories of confined reactions systems in a prokaryotic cell. A) A membrane-bound enzyme (yellow) is catalyzing membrane-bound substrates (red) to membrane-bound products (blue). B) A membrane-bound enzyme (yellow) catalyzing substrates (red) to products (blue) that diffuse through the cytosolic space. C) Proteins (green), e.g., Transcription factors, binding to DNA (red) D) Enzymes (yellow) catalyzing, substrates (red) to products (blue) within the crowded cytosol (grey). . . . .	4
2.1	Detection of effector–chromatin interactions on the single-molecule level. A) Schematic representation of the smTIRF imaging experimental setup showing HP1 interacting with a chromatin fiber B) Representative microscopy images showing the localization of the chromatin fibers (left panel) and individual HP1 $\alpha$ molecules bound to chromatin (right panel). The scale bar is 5 $\mu$ m. B) Characteristic time trace (blue) of HP1 $\alpha$ binding dynamics to a single chromatin fiber and fitted with a step function (red). Each intensity peak represents one binding event. C) Dissociation kinetics: cumulative histograms of HP1 $\alpha$ dwell times of 100 traces fitted with a double-exponential function. D) Association kinetics: cumulative histogram of times between each binding event of the same 100 traces, fitted with a mono-exponential function . . . . .	14
2.2	Full reaction network model of HP1 chromatin interactions. All reactions between the indicated states are reversible and governed by equilibrium and rate constants. . . . .	16
2.3	A) Histogram of the events with in log space with event cutoff (left) and B) without event cutoff (right). C-D) Comparison of the stochastic simulations of E) HP1 $\alpha$ wt. with D) a simulation where the dimerization is inhibited i.e. the equilibrium constant of the dimer was increased by a factor of $10^3$ . . . . .	21

## List of Figures

---

- 2.4 A) Full kinetic model of HP1-chromatin interactions, showing the pathways associated with high flux (arrow thickness). Gray arrows denote reactions associated with low but non-zero flux. Arrowhead size indicates the direction of net flux. B) Dependence of simulated HP1 dissociation rate constants ( $k_{off} = 1/\tau_{off,1}$ ) on relative changes in  $K_{PTM}$  and  $K_{DNA}$ . Parameters for circle: HP1 $\alpha$ , cross: HP1 $\beta$ , square: HP1 $\gamma$ . The color code and contour lines indicate changes in the dissociation on a logarithmic scale. C) Dependence of simulated HP1 binding rate constants ( $k_{on}$ ) on relative changes in methyllysine (KPTM) and DNA (KDNA) interactions. Parameters for O: Parameters for circle: HP1 $\alpha$ , cross: HP1 $\beta$ , square: HP1 $\gamma$ . The color code and contour lines indicate changes in the binding rate on a logarithmic scale. . . . . 23
- 2.5 Fold change of the model outputs in GSA. The tenfold change of the model outputs (HP1 bound,  $\tau_{off,1}$ ,  $\tau_{off,2}$ ,  $A_2$ ) is plotted vs the tenfold change of the most important model parameters. Data is given as blue dots. The slope of the red lines indicates the mean fold-change of the output parameters with respect to a fold-change in the input parameter . . . . . 24
- 3.1 Modeling framework for crowded generalized elementary kinetics (GEEK). The input for the modeling framework is an arbitrary elementary step model containing in vitro data for the enzyme kinetics. 1) This model is then translated into an equivalent in vitro particle model of the enzymatic reaction. 2) The space is filled with inert molecules that are drawn from a size distribution  $p(r)$  until the fraction  $\phi$  of the simulation space is occupied. 3) A reference concentration state is then chosen for the GEEK model, and 4) the space around the concentration space is sampled. 5) The  $k$  particle model realizations are then simulated for each concentration sample, i.e., repeat step 2 and simulate. 6) From the resulting particle traces, the effective rate constants are measured from the particle collision frequencies and the locally available volume. 7) These effective reaction rate constants are log transformed, and a linear regression is performed with respect to the scaled logarithmic concentrations. The output of the linear regression directly links to the GEEK parameters; see Eqs. 7 and 8. 8) Finally, the GEEK model can approximate the crowded kinetics using ODEs. . . . . 39
- 3.2 Size distribution function of the inert particles, numerically calculated from the mass distribution and empirical mass size relation as reported for proteins in *E. coli* by Kalwarczyk et al. (2012). . . . . 45



- 3.3 (a)  $[P]/[S]$  dynamics determined for mass-action and GEEK models for different initial substrate concentrations  $[S]_{init}$  and different occupied volume fractions ( $\phi$ ) for the *E. coli* molecular weight distributions. The light dashed lines represent the dilute mass-action model, whereas the thin solid lines represent a population of 100 resampled GEEK models. (b) Time to half-equilibrium  $t_{eq}/2$  as a function of the occupied volume fraction for different initial substrate concentrations  $[S]_{init}$  is shown. The colors of the lines denote the different initial concentrations: blue corresponds to  $[S]_{init} = [S]_{ref}/4$ , yellow to  $[S]_{init} = [S]_{ref}$ , green to  $[S]_{init} = 2[S]_{ref}$ , and red to  $[S]_{init} = 4[S]_{ref}$ . . . . . 48
- 3.4 Effective Michaelis-Menten parameters (a)  $K_{M,S}$  and  $K_{M,P}$  and (b)  $V_{max}^+$  and  $V_{max}^-$  as a function of volume fraction. The gray dashed lines represent the effective parameters when all concentrations are scaled to an effective volume  $V_{eff} = V(1 - \phi)$  that excludes the volume occupied by inert molecules. The errors in the values calculated from uniformly resampling the GEEK parameters are smaller than 2% of the mean. . . . . 50
- 3.5 Effects of the particle size distribution. (a) Time to half-equilibrium  $t_{eq}/2$ , (b) enzyme saturation  $[ES]/[E]_{tot}$  for  $[S]_{ref} = 49 \mu\text{M}$ , and (c) apparent standard free energy of the reaction measured as  $RT \log([P]_{eq}/[S]_{eq})$  under different crowding conditions are shown. The circles represents the apparent equilibrium measured from the *E. coli* size distribution; crosses, diamonds, and squares are obtained using a single size of inert molecules corresponding to the lower quartile, the median quartile, and the upper quartile of the *E. coli* size distribution, respectively. The error bars denote the upper and lower quartile of the resulting population that was obtained by resampling the GEEK model parameters within their confidence bounds. The horizontal black line denotes the equilibrium constant calculated from the in vitro kinetic parameters. . . . . 51
- 4.1 A) Comparison of the analytical solution for the pair-distribution function  $\rho_{mn}$  for an irreversible reaction  $m + n \rightarrow l$  with constant constant concentrations and at steady state at different discretizations  $N_E$ . B) Error at of the pair distribution  $\rho_{mn}$  function at the collision interface as a function of  $N_E$  and  $L$ . . . . . 61
- 4.2 A) Equilibrium radial disitrbution functions for a pair pair  $m, n$  with  $R_m = 1 \text{ mn}$  and  $R_n = 3 \text{ mn}$  in a mixture of hard-spheres with  $\phi = 0.0$  (line),  $\phi = 0.2$  (dashed) and  $\phi = 0.4$  (dotted) fraction of macromolecules following the discrete size distribution given in B) Discrete (bars) and continous (line) size distribution of macromolecules Kalwarczyk et al. (2012). . . . . 63

## List of Figures

---

- 4.3 Calculation of the excess free energy, based on the thermodynamic equivalence of i) introducing a pair into an ideal solution, separating it and introducing crowded molecules, and ii) introducing the pair in contact into a solution with the same crowding properties and then separate it. . . . . 64
- 4.4 Change of the relative dissociation constant calculated using the hard-sphere model of PGM as presented in the previous chapter (circles and crosses) compared to the theoretical model derived in this chapter (solid line). The changes for the theoretical model are calculated based on the size distribution of macromolecules by Kalwarczyk et al. (2012) and for species  $l$  with  $R_n = 3$  mn dissociating into pairs  $m, n$  with sizes  $R_m = 1$  mn and  $R_n = 3$  mn. . . . . 66
- 4.5 Effective diffusion coefficient as a function of the macromolecular volume fraction for species with  $R_1 = 1$  mn (circles),  $R_1 = 2$  mn (crosses) and  $R_1 = 3$  mn (squares) in a hard-sphere mixture following the size distribution given in Kalwarczyk et al. (2012). . . . . 68
- 4.6 A) Enzyme essay at different volume occupacys,  $\phi_M = 0.0$ , (sold)  $\phi_M = 0.2$  (dashed),  $\phi_M = 0.4$  (dotted), for a reaction controlled enzyme  $d_{E,S \rightarrow ES} = d_{E,P \rightarrow EP} = 10^{-2}$ . B) Enzyme essay in log-lin-scale normalized by the apparent maximal velocity  $V_{max}^{app}$  to illustrate the change of  $K_{M,S}$  in corwded conditions. . . . . 73
- 4.7 A) Relative change in maximal enzyme rate  $V_{max}/V_{max}^0$  compared to the relative change in dissociation rate constant (solid line) as well as B) relative change of the Michaelis-Menten parameter  $K_{M,S}/K_{M,S}^0$  compared to the change of the equilibrium constant of the association reaction (solid line), C) relative pair distribution function between products and enzymes at highest substrate concentration  $\rho_{E,P}/[E][P]$  and D) relative pair distribution function between substrates and enzymes at highest substrate concentration  $\rho_{E,S}/[E][S]$  as a function of macromolecular volume fraction for enzymes with different diffusion-controlled ratios  $d = 10^{-6}$  (crosses),  $10^{-2}$  (circles),  $10^0$  (squares). . . . . 75
- 4.8 Normalized pair distribution function at the contact radius  $\rho_{E,P}(R_{E,P})/[E][P]$  at steady state as a function the substrate concentration with illustrations of the increasing local concentration of product (blue) around the enzyme (yellow) surrounded by macromolecules (grey). . . . . 76

4.9 Comparing the A) maximal enzyme rate  $V_{max}/V_{max}^0$  and B) relative change of the Michaelis-Menten parameter  $K_{M,S}/K_{M,S}^0$  as a function of macromolecular volume fraction for enzymes with different diffusion-controlled ratios  $d = 10^{-6}$  (diamonds),  $10^{-2}$  (circles),  $10^0$  (squares) between the original model (empty symbols) and the model corrected for product accumulation in proximity to the enzyme (filled symbols). . . . . 77

5.1 Double logarithmic plot of the relative change of the effective reaction rate constants with respect to the dilute rate constant for the substrate association and dissociation reactions  $(m, 1)$ ,  $(m, 2)$  as well as the product dissociation and association reaction  $(m, 5)$ ,  $(m, 6)$  as a function of the enzyme species concentrations calculated using the theoretical reaction-diffusion model presented in chapter 4. 86

5.2 Enzyme flux elasticities with respect to substrate, product and total enzyme concentrations calculated with mass-action kinetics (blue), dilute (orange) and crowded (green) ( $\phi_M = 0.3$ ) GEEK for A) diffusion controlled enzyme  $d = 10^0$  and B) a reaction controlled enzyme  $d = 10^{-2}$ . . . . . 90

5.3 Control coefficients of the linear pathway for the total enzyme concentrations  $[E_{1,T}]$ ,  $[E_{2,T}]$  and  $[E_{3,T}]$  calculated with mass-action kinetics (blue), dilute (orange) and crowded (green) ( $\phi_M = 0.3$ ) GEEK for A) diffusion controlled enzyme  $d = 10^0$  and B) a reaction controlled enzyme  $d = 10^{-2}$ . . . . . 92

5.4 Control coefficients of the fluxes  $v_1$ ,  $v_2$  and  $v_3$  in the branched pathway with respect to the total enzyme concentrations  $[E_{1,T}]$ ,  $[E_{2,T}]$  and  $[E_{3,T}]$  calculated with mass-action kinetics (blue), dilute (orange) and crowded (green) ( $\phi_M = 0.3$ ) GEEK for A), C) and E) a diffusion controlled enzyme  $d = 10^0$  as well as B) D) and F) for a reaction controlled enzyme  $d = 10^{-2}$  . . . . . 94

A.1 Left column time traces of collision events between E and S as a function of time and the running mean over 100 time intervals. Right column histograms of all data point of the collisions time trace (All), the first (Beginning), and the last (End) 100 data points compared with a binomial distribution where  $p = \langle c(E, S) \rangle / N_E N_S$  and  $n = N_E N_S$ . The upper row show the results with  $\phi = 0\%$  the lower row for  $\phi = 40\%$  for the crowding size distribution in E. coli. . . . . 106

A.2 Model results for OLS and WLS for the model output  $Y_i = \log(k_{1,f,eff}/k_{1,f,0})$ . Left column: Residuals vs. fitted output values  $Y_i'$  Right column: Probability density of the residuals. Upper row: Residuals of the OLS model. Lower row: Effective residuals of the WLS model. . . . . 107

## List of Figures

---

A.3	Projection of the simulated data points onto the respective concentration axis for (blue) $\phi = 0\%$ (orange) $\phi = 30\%$ and (green) $\phi = 50\%$ inert volume fraction with the E. Coli size distribution. The black line denoted the conditional mean, and the dashed line denoted the conditional 5% and 95% percentiles at the corresponding concentration value for $\phi = 50\%$ inert volume fraction. . . . .	108
A.4	Concentration of $[A]$ as a function of time $t$ for $\phi = 0$ for GEEK (blue) and openbread (red) (left column) and concentration in equilibrium for different $\phi$ (right column). For the reaction controlled case (upper row) and the diffusion controlled case (lower row). . . . .	110
A.5	Initial reaction rate measured as the mean change of $[A]$ for GEEK (blue) and openbread (red) measured for different $\phi$ , for the reaction controlled case (left) and the diffusion controlled case (right). . . . .	111
A.6	Concentration of $[A]$ as function of time $t$ for $\phi = 0$ for GEEK-CFCH (blue) and CFCH (red) (left column) and concentration in equilibrium for different $\phi$ (right column). For the reaction controlled case (upper row) and the diffusion controlled case (lower row). . . . .	112
A.7	Initial reaction rate measured as the mean change of $[A]$ for GEEK- CFCH (blue) and CFCH (red) measured for different $\phi$ , for the reaction controlled case (left) and the diffusion controlled case (right). . . . .	112
A.8	Comparison of different propagation schemes. a) Brownian motion where the propagation is simply determined by the velocity $v$ drawn from the respective velocity distribution function. b) Explicit elastic hard-sphere collision, particles are moved with the initial velocity $v$ until time $t + \Delta t_1$ when the collision occurs. The velocities are updated according to the law of momentum conservation then propagated for the remaining part of the time step $\Delta t_2 = \Delta t - \Delta t_1$ . c) Propagation according to the Cichoki-Hinsen algorithm where the collision is simply rejected if the hypothetical positions after the time $\Delta t$ lead to overlap with another particle.	114

# List of Tables

2.1	Fit results from smTIRF measurements of HP1 $\alpha$ , $\beta$ and $\gamma$ chromatin interactions. *Values taken from Kilic et al. (2015) . . . . .	14
2.2	Thermodynamic constraints on the equilibrium parameters . . . . .	17
2.3	A list of all dimensionless model variables given a short description and expres- sion in terms of the reference concentrations. . . . .	18
2.4	A list of all dimensionless model variables given a short description and expres- sion in terms of the reference concentrations. . . . .	18
2.5	A list of all dimensionless forward rates. The first half of the table denotes the reaction rates for the three-dimensional reactions and the second half of the table denotes the reaction rates for the migration rates. . . . .	19
3.1	<i>In vitro</i> Michaelis-Menten parameters and calculated elementary rate constants for PGM in <i>E. coli</i> , as found by Fraser et al. (1999) . . . . .	43
3.2	Molecular Properties of the Reacting Particles, data obtained from: a) Perry (1973), calculated according to the approximations suggested by b) Gameiro et al. (2016) as well as obtained from c) Gameiro et al. (2016) . . . . .	44
3.3	Microscopic reaction rates per reacting particle (p), or per collision (c), and diffusion-limited rate constants of the bimolecular reactions. . . . .	44
3.4	Parameters of the generalized elementary kinetics, i.e. $\alpha_{ij}$ and $\beta_j$ , for all ele- mentary reactions at different inert volume fractions, where * denotes GEEK parameters with a significance of $p \leq 0.05$ . . . . .	46
5.1	Mass-action terms for the three step Michaelis-Menten mechanism . . . . .	83
5.2	Logarithmic sensitivities $\alpha_{m,i,j}$ for the association rate constants $i \in [1,6]$ in dilute and crowded $\phi_M = 0.3$ conditions for diffusion controlled and reaction controlled enzymes. . . . .	86

## List of Tables

---

5.3	Concentration elasticities of the elementary reactions for a three-step Michaelis-Menten mechanism, as denoted in equation 5.6, with $[X_i]$ denoting all species of the system that are not involved in the enzyme mechanism . . . . .	87
5.4	Elementary parameter elasticities with respect to the total enzyme concentration.	88
5.5	Enzyme parameters for the linear pathway . . . . .	91
5.6	Enzyme parameters for the branched pathway . . . . .	93

# 1 Background and Scope

Living cells reproduce by consuming energy-rich nutrients in their environment and use the energy and their atoms to create new molecules that make up their very own building blocks. This process, called metabolism, sustains every living organisms and is the foundation of our existence. Cells have evolved a piece of sophisticated machinery to sustain this reproductive behavior. This machinery allows them to transform information stored in the form of polymeric molecules, deoxyribonucleic acid (DNA), into functional polymer units called proteins. Therefore the information stored centrally on the DNA is transcribed into other polymers, messenger ribonucleic acid (mRNA), by some part of this machinery, RNA polymerase, to allow. The mRNA then provides this information to the Ribosomes, a piece of the machinery that uses the recipe transcribed into the mRNA to assemble a protein as a sequence of specific amino acids. These proteins then implement biological functionalities by binding to other proteins (Jones and Thornton, 1996), change their configuration (Pivovarov et al., 2018; Skou, 1957; Deng et al., 2014), assemble into structures (Pieters et al., 2015), catalyze biochemical reactions (Buchner, 1897; Sumner, 1935) or by a combination of these principles (Boyer, 1997). Enzymes, proteins catalyzing biochemical reactions, allow cells to breakdown molecules from their environment and create new molecules from their fragments and the energy harvested by breaking the original molecules down. Some organisms, such as plants and cyanobacteria, even evolved proteins that use the energy stored in light photons directly, allowing them to utilize low energy molecules such as carbon dioxide (CO<sub>2</sub>) to construct the molecules necessary for their reproduction (Tabita et al., 2007). Other proteins implement signaling networks that allow cells to process chemical signals from their environment and then execute response programs to adapt to changes in the environment in a time- and space-dependent manner (Kornberg and Tabata, 1993; Goehring et al., 2011). Therefore, proteins located at the periphery of the cell modify proteins within the cells to delay the input signal to the location of

the DNA to regulate which information on the DNA is translated to proteins. The interactions between the modified proteins and the proteins to be activated and repressed can, in this way, implement complex programs in response to the biochemical information outside the cells. The display of specific proteins on the cell surface or the expression of transported proteins allow then further to send chemical signals between cells enabling them to coordinate their responses. The dynamics of these biochemical reaction networks are crucial for understanding and predicting how living entities, such as cells and organisms, react upon genetic and environmental perturbations.

### 1.1 Confinement of biochemical reactions

All this complex biochemical machinery that allows the cell to adaptively produce its components, including the components necessary to build and maintain this machinery, is confined within a small membrane-enclosed space (Lombard, 2014). In eukaryotic cells, the interior of this membrane-enclosed space is further separated into compartments with specialized functions, resulting in a different composition of macromolecules for every separated compartment (Alberts, 2014). The biochemical reactions that govern the cellular functions occur within these membrane-enclosed spaces. The molecules participating in these reactions are thus traveling through a complex and diverse environment shaped by the different kinds of macromolecules inside these spaces. The complexity of the environment has a significant effect on the transport properties of the molecules involved in the biochemical reactions (Benichou et al., 2010; Zhou et al., 2008). These transport properties are essential for the characteristics of biochemical reactions. As for a reaction to occur, the reactants need to be in close proximity. The relative transport dynamics between the reactants are thus the determining factor for the dynamic behavior of the biochemical reactions.

The most prominent of the macromolecules inside the intracellular subvolumes are proteins, lipids, polysaccharides, RNA, and DNA (Ellis, 2001). Proteins are the most abundant among these macromolecules implementing most of the cellular functions. Proteins can form many different structures, such as filaments (Dominguez and Holmes, 2011; Carlier and Pantaloni, 1981), aggregates (Pieters et al., 2015), or phase-separated droplets (Hyman et al., 2014). However, many of the proteins do not participate in any structure, diffusing throughout the complex solute along with the small molecules. Further, a significant fraction of proteins participate in biochemical reactions as enzymes. Thus, their transport properties are relevant to many biological functions.



## 1.1. Confinement of biochemical reactions

---

Lipids make up the very membranes that enclose these subvolumes but also form smaller structures such as micelles and vesicles Gorter and Grendel (1925); Šegota and Težak (2006). Vesicles enclose themselves small subspaces creating small separated environments. These lipid membranes can further bind proteins from the intercellular space that are bound to a lipid anchor (Ferguson, 1991). Other proteins are directly synthesized as transmembrane proteins and, therefore, only functioning when assembled across as well as tightly bound to it (Vinothkumar and Henderson, 2010). Proteins that are bound to a membrane are restricted in their movement to two dimensions, exhibiting thus different transport properties. Polysaccharides can often be secreted and can form layers at the periphery of the extracellular space (Flemming and Wingender, 2010) or aggregate at specific cellular locations to be used as long term energy storage (Robyt, 2001) or to form support structures (Pauly and Keegstra, 2016). RNA and DNA molecules are filamentous structures that act as binding sites for different kinds of proteins. Their string-like structure leaves the molecules binding unspecifically to the molecules with a single spatial degree of freedom, resulting in diffusion along with the DNA or RNA molecules.

Filamentous protein structures such as actin (Dominguez and Holmes, 2011) and microtubules (Carlier and Pantaloni, 1981; Desai and Mitchison, 1997) can bind specific proteins that are then actively driven by the dephosphorylation of adenosine triphosphate (ATP) to *walk* along the filament, resulting in an actively driven transport along the protein structure (Sweeney and Houdusse, 2010). Depending on the cell type, compartment, and spatial localization, these macromolecules can occupy up to 40% of the intracellular volume (Ellis, 2001; Ellis and Minton, 2003; Minton, 2001), resulting in a reduced accessible volume for the molecules that diffuse through this space. The reduced volume also increases the probability of collisions between molecules. These collisions lead to deflections along the path of diffusion, changing the effective transport properties of all the molecules in the solution (McGuffee and Elcock, 2010; Jeon et al., 2016).

Based on the cellular structures and transport mechanisms, we may classify the confinement of the biochemical reactions into several different categories. Therefore, we classify the confinement transport problems based on two criteria i) their molecular transport mechanism and ii) the ideal dimension of their accessible space. This dimension considers the ideal spatial degrees of freedom of the reactants. Based on the molecular transport mechanism, we can distinguish between active and passive transport. Active transport involves a transport mechanism that uses chemical energy for a directed movement, such as the use of ATP dephosphorylation by myosin to sustain a directed movement along an actin filament (Sweeney

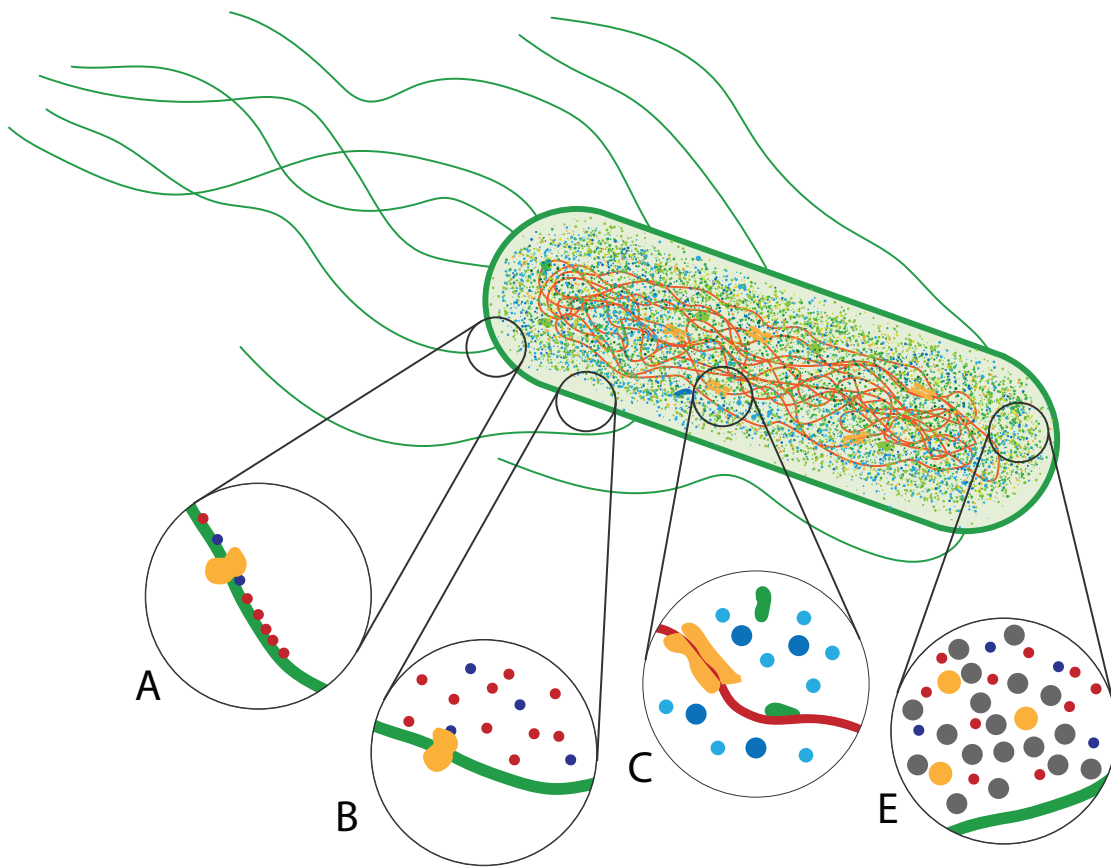


Figure 1.1 – Illustrations of different categories of confined reactions systems in a prokaryotic cell. A) A membrane-bound enzyme (yellow) is catalyzing membrane-bound substrates (red) to membrane-bound products (blue). B) A membrane-bound enzyme (yellow) catalyzing substrates (red) to products (blue) that diffuse through the cytosolic space. C) Proteins (green), e.g., Transcription factors, binding to DNA (red) D) Enzymes (yellow) catalyzing, substrates (red) to products (blue) within the crowded cytosol (grey).

and Houdusse, 2010). Passive transport inside the cell is transport by thermal diffusion and diffusion along a concentration gradient. Based on the ideal dimension of the accessible space, we find three different scenarios in the cases described above i) three-dimensional (3D) transport inside the intracellular space, ii) two-dimensional transport (2D) of membrane-bound molecules, and iii) one-dimensional transport (1D) of species bound to string-like structures such as RNA, DNA and protein fibers. Considering that the reacting part of the molecules is linked rigidly to the part of the molecule binding to a structure, confined biochemical reactions can be classified by the transport properties of the respective educts and products. It should be noted here that if the structure-bound part of the molecules is linked flexibly to the reactive part, adding a layer of complexity to this classification.

## 1.1. Confinement of biochemical reactions

---

All the effective transport spaces are crowded with different kinds of macromolecules. Each transport mode, active or passive, and in 1D, 2D, or 3D is differently affected by this macromolecular crowding. All of the transport modes are affected by some form of anomalous diffusion (Hofling and Franosch, 2013). So it has been shown that for transcription factors diffusion along a DNA string, other transcription factors on the DNA facilitate the dissociation resulting in a mixed 1D, 3D transport model for the transcription factor binding dynamics (Li et al., 2009). It was also shown that static obstacles decrease the mean first passage times for targets in close proximity as opposed to those far away and that this relation holds in two and three dimensions for any diffusion-based transport mechanism (Benichou et al., 2010). Crowding in 3D domains can introduce anisotropic diffusion effects (Grima et al., 2010). Further, heterogenous crowding conditions in three dimensions can direct the motion of molecules by introducing an advective like velocity component directed towards less crowded regions. (Smith et al., 2017).

As mentioned above, the change in the transport properties between the reactants affects their reaction dynamics (Examples in figure 1.1). This has been shown in the work of (Smoluchowski, 1927). He could show already that if every encounter leads to the diffusion and the capture radius, drive the kinetics of the reaction. His work was then generalized to include partially absorbing boundary conditions to consider that not all encounters lead to a successful reaction (Collins and Kimball, 1949a,b) However, the overall reaction dynamics are affected by more than merely the transport between the reactants. They are also impacted by the structure of the fluid and the thermodynamics of the solution. One of the early works on macromolecular crowding revealed that volume exclusion shifts the thermodynamic equilibrium of reactions Minton (1981). The fluid-structure also has an impact on the reaction dynamics. It was first shown by Debye (1942) as he was the first to consider electrostatic forces in irreversible diffusion-limited reactions. These results were then later generalized to include any other forces and partially absorbing boundary conditions (Szabo, 1989; Berezhkovskii and Szabo, 2016). Finally, the Smoluchowski theory was generalized to describe reaction networks close to equilibrium (Gopich and Szabo, 2002, 2018). Despite these efforts, no conclusive theoretical model has been developed that accounts for i) the thermodynamics, ii) the fluid-structure as well as the changes in iii) transport properties for diffusion-controlled biochemical reactions in crowded environments. Instead, crowding effects on reaction kinetics were usually investigated using lattice-based monte claro methods (Schnell and Turner, 2004; Grima and Schnell, 2007, 2008; Grima, 2010; Mourao et al., 2014; Sturrock, 2016), or Brownian reaction dynamics simulations (Schoneberg and Noe, 2013; Biedermann et al., 2015; Smith and Grima, 2017). Although these methods potent to investigate stochastic and inhomogeneous systems as they

## Chapter 1. Background and Scope

---

allow to characterize noise, they are computationally relatively expensive. Generally speaking, the lattice-based models are computationally less expensive but limited in their spatial resolution, whereas the Brownian reaction-based methods allow introducing a wide range of particle sizes. However, especially when the system dynamics span across multiple orders of magnitude in their characteristic times, the computational cost starts to increase significantly. Even the comprehensive simulation of a partial reaction network of an organism in crowded conditions, e.g., glycolysis, is a task still to be completed. Also, simulations of crowded reaction dynamics have so far been limited to species diffusing in three or two dimensions, leaving out mixed scenarios of cytosolic enzymes that adsorb to the membrane and catalyze reactions involving the lipids on the membrane.

Intuitively macromolecular crowding effects can be separated into two counteracting contributions i) the decrease of the effective diffusion constant and ii) the reduction of the available volume. The diffusion constant decreases since the average diffusion path between two reactants increases as these have to diffuse around the macromolecules. Additionally, collisions of the reactants with the macromolecules reduce their diffusion as these collisions deflect the path of free diffusion, further increasing the average diffusion path. This decrease of the effective diffusion constant of the respective reactants results in a reduced collision frequency and with that in a reduction of the effective reaction rate constant. On the other hand, the macromolecular crowding decreases the available volume for the respective reactants. This decrease of the available volume has two contributions i) the volume occupied by the macromolecules themselves ii) and the volume that is not available to the reactant due to its interaction with the macromolecules. The second contribution depends strongly on the relative size of the macromolecules and the reactants and vanishes in the limit of large macromolecules and small reactants and increases in the reverse case. The reduction in the available volume effectively increases the concentrations of the reactants. This effective increase in the concentration increases the collision frequency and, therefore, the effective reaction rate constants counteracting the effect of decreased diffusion. The effect of macromolecular crowding on the effective reaction rates depends thus on the relative contributions of the reduction in diffusion constant and the reduction of the available volume of the individual reactants. The relative size distributions of different reactants, such as enzymes and substrates is thus a key factor for the rate of the effective reaction rates.

### 1.2 *In silico* reevaluation of *in vitro* data

The intracellular environment has a significant effect on the biochemical reaction kinetics, introducing several layers of complexity. Thus, when extracting components from the cell to study them in a *in vitro* setup, this complexity is lost, and the transport properties of the biochemical reactants simplify to their dilute transport properties. Thus the dynamic properties of biochemical reactions observed *in vitro* are not the ones we expect in the intracellular environment. Nevertheless, *in vitro* studies are an essential tool to decipher cellular function experimentally as they offer tools to perturb biochemical systems in a controlled setting, excluding unknown factors from the cellular systems (Shaw et al., 1990; Visco et al., 2016; Su et al., 2016). They further allow us to study enzyme reaction kinetics by perturbing the substrate concentrations and measuring turnover rates, an experiment that in within the cellular environment would not be possible as the enzyme concentration, as well as the metabolite concentrations, would need to be measured, controlled and varied within a living cell (Brooks et al., 2004). With the amount of *in vitro* kinetic enzyme data available, it is thus tempting to reconstitute the partial subsystems characterized *in vitro* to complete systems using computational methods (Schomburg et al., 2013; Wittig et al., 2012). Such an approach is widely used for building kinetic models (Emiola et al., 2015; Watterson et al., 2013). Here enzyme rate laws characterized *in vitro* are directly incorporated into kinetic models and then used to analyze the properties of the system. Such an approach assumes that the reaction kinetics within the cellular environment are the same as the ones reconstituted *in vitro*. As we have discussed in detail above, this is most likely not the case for most biochemical reactions.

The other most common way to gain information on the biochemical parameters inside the cell is by using parameter identification methods such as genetic algorithms (Deb et al., 2002; Deb and Jain, 2014), covariance matrix adaptation evolutionary strategy (Hansen et al., 2003; Igel et al., 2007) as well as other strategies based on optimal transport (Öcal et al., 2019) or adaptive sampling (Asmus et al., 2017). In all these parameter identification methods, a set of experimental perturbations is used to match to find a set or sets of parameters for a model so that its predictions are in agreement with measured data. Thereby an objective function is used to evaluate the agreement between simulated and measured data, and the parameters are changed until one or multiple satisfying parameter sets are found. The different parameter identification methods differ mainly in two aspects i) how these parameter sets generated ii) how the parameter sets are selected. The different methods of generating and selecting data sets aim to optimize the parameter identification methods for various tasks, such as finding parameter sets that full fill the objective functions with large variability in the parameter sets

## Chapter 1. Background and Scope

---

(Asmus et al., 2017), identifying trade-offs between multiple objective functions (Deb et al., 2002; Deb and Jain, 2014; Igel et al., 2007) or dealing with uncertainty in the determination of the objective function (Öcal et al., 2019).

By using directly the data from perturbation experiments done in living cells, we can gain insight into the effective parameters within the cell. As the knowledge of cellular biochemistry grows with increasing speed, models become more and more detailed. In contrast, the quantitative data on the system in question is often limited as it is expensive to generate. With increasing network complexity, the parameter uncertainty increases. This increase in uncertainty can be circumvented by including more experimental data to fit the model. To circumvent this increase in parameter uncertainty models are often simplified (Mayer et al., 2010). On the other hand, generating a purposefully smaller model reduces the pre-existing knowledge of the structure of the biochemical reactions network, thus reducing the model's structural information. With this, the parameter identification problem becomes a theoretical information problem where the information within the data is information to be extracted into the information on the model parameters (the more information, the less uncertainty (Shannon, 1948)) given a set of structural information. From a theoretical information point of view, it is easy to argue that the model with most structural information and parameter information is the best model as it can extract the most from the data. This might not be the case anymore when using the model to address a biological or an engineering question. Since, as soon as the question is asked, the information within the network, i.e., the parameters and the model structure, becomes differently important. Therefore not model with the most information, but the model with the most information regarding the question becomes the most useful model to identify the model parameters.

In this thesis, we advocate for increasing the amount of information in those models by making use of a combinatorial approach that utilizes both i) parameter identification using *in vivo* perturbation experiments and ii) the integration of *in vitro* measured data. To integrate these two approaches successfully, we propose to use theoretical and computational models to reconstitute the *in vitro* data in an *in vivo* like environment to find appropriate corrections of the effective reaction kinetic parameters. Such a two-fold approach may help address the shortcomings of both parametrization methods and make the most of the already existing information. To apply the *in silico* reconstitution of *in vitro* experimental data in an *in vivo* like environment on a large scale new efficient computational methods will be essential. In this thesis, we provide methods and studies that aid this development.

### 1.3 Thesis overview

This thesis is organized into six chapters. We here give a brief overview of the content discussed in this thesis. In this first chapter, we introduced the concept of confined reaction kinetics and the concepts of parameter estimation and parameter correction.

In **chapter 2**, we present a study on multivalent protein binding to chromatin. In this study, we make use of parameter estimation techniques to identify the binding mechanism and study the model cellular conditions.

In **chapter 3**, we present a particle-based analysis of the Michaelis-Menten kinetics in crowded conditions. We present a novel method to approximate the reaction kinetics of crowded reactions efficiently.

In **chapter 4**, we derive a comprehensive mean-field model for crowded, diffusion-controlled kinetics based on the Smoluchowski equation in non-equilibrium situations. We provide an analytical solution for the steady-state flux of diffusion-controlled bimolecular reactions displaced from equilibrium. We then use this model to study the effect of crowding on diffusion and reaction controlled enzymes.

In **chapter 5**, we use the mean-field model derived in chapter four in combination with the efficient approximate reaction kinetics to formulate a metabolic control analysis method for crowded reaction kinetics. We apply this crowded metabolic control analysis to analyze the steady-state responses of prototypical reaction networks.

Finally, in **chapter 6**, we summarize the conclusions of this thesis and provide perspectives for the future study of confined reaction networks and in vitro parameter corrections.





## 2 Modeling of multivalent protein binding on chromatin

This chapter is part of work published as: Bryan, L. C., Weilandt, D. R., Bachmann, A. L., Kilic, S., Lechner, C. C., Odermatt, P. D., Fantner, G. E., Georgeon, S., Hantschel, O., Hatzimanikatis, V., and Fierz, B. (2017). Single-molecule kinetic analysis of HP1-chromatin binding reveals a dynamic network of histone modification and DNA interactions. *Nucleic Acids Res*, 45(18):10504–10517.

For this work, the deterministic and stochastic modeling, the parameter identification, as well as the sensitivity analysis, were performed by Daniel Weilandt under the supervision of Beat Fierz and Vassily Hatzimanikatis.

### 2.1 Introduction

In this first chapter, we investigate the kinetics of a protein (HP1) that has the ability to bind to a 1D like structure (Chromatin). Chromatin is a complex of proteins and DNA that organizes the eukaryotic DNA. It forms a filament-like structure that compacts the DNA with a length of about 2 m to fit into the nucleus with a diameter of 5 – 10  $\mu\text{m}$  (Alberts, 2014). The core structures of the filament are the nucleosomes, these are assembled from Proteins and DNA. A nucleosome consists of a protein core around which 147 base pairs (bp) of DNA are wrapped. The protein core is made up of an octamer of two of each of the four core histones H2A H2B H3 and H4. The nucleosomes are connected by 30-70 bp of linker DNA forming a bead on a string like structure (Luger et al., 2012). This complex exists in different states, depending on the function of the underlying genomic sequence. In regions of active gene transcription, the beads form an open structure, mediated by acylation of the core histones called euchromatin. The open structure is highly dynamic and constantly remodeled to control gene expression.

## Chapter 2. Modeling of multivalent protein binding on chromatin

---

In regions of repressed transcription, the histones are not acetylated, and the presence of repression associated post-translational modifications (PTMs) on the core histones, linker histones H1 and structural effect proteins such as HP1 result in a compacted chromatin state. These PTMs are thought to serve as binding sites for proteins that assist in the compaction of the chromatin structure, e.g., triple methylation of the ninth lysine of the core histone H3 (H3K9me3) is such a PTM has been shown to promote binding of the HP1 (Kilic et al., 2015). Combinations of further PTMs in all core histones allow further discrimination of chromatin in multiple distinct functional states (Smith and Shilatifard, 2010; Kharchenko et al., 2011). A key question in chromatin research considers how PTM combinations are translated into biological function. Multivalent interactions between effector proteins carrying specific reader domains and histone PTM patterns seem at the core of chromatin regulation. Currently, the molecular determinants of multivalent PTM recognition are not well understood.

HP1 family proteins function as fundamental components of heterochromatin involved in gene regulation including suppression of latent viruses and transposable elements in the genome (Elgin and Grewal, 2003). Heterochromatin denotes compact and transcriptionally repressed chromatin domains characterized by H3 di- and tri-methylated at lysine 9 (H3K9me<sub>2/3</sub>), the absence of histone acetylation and the presence of linker histone H1 (Jenuwein and Allis, 2001). H3K9me<sub>2/3</sub> serve as binding sites for HP1, which accumulates at heterochromatin loci and induces gene silencing (Maison and Almouzni, 2004). In mammals, HP1 proteins include three isoforms: HP1 $\alpha$ , HP1 $\beta$  and HP1 $\gamma$  (Maison and Almouzni, 2004) with different sub-nuclear localization and function (Dialynas et al., 2007; Singh, 2010; Brown et al., 2010): Both HP1 $\alpha$ , and HP1 $\beta$  associate with heterochromatin, while HP1 $\gamma$  has also been shown to localize in euchromatin. HP1 proteins are similar in structural architecture: they contain a chromodomain (CD), which specifically interacts with H3K9me<sub>2/3</sub> with affinities around 1–10  $\mu$ M (Kouzarides, 2007), a flexible hinge region (HR) that interacts with nucleic acids as well as a dimerization domain (chromoshadow domain, CSD) (Thiru et al., 2004). Dimeric HP1 can bind to chromatin in a multivalent fashion by engaging two H3K9me<sub>3</sub> sites, thereby cross-bridging nucleosomes (Canzio et al., 2011; Hiragami-Hamada et al., 2016), and reducing access for the transcription machinery (Woodcock and Ghosh, 2010; Azzaz et al., 2014). In spite of their structural role, HP1 proteins are in rapid exchange in living cells (Müller et al., 2009; Festenstein et al., 2003; Cheutin et al., 2003), forming locally dynamic compartments that are nevertheless stable over time. Such local dynamic behavior is indeed important, enabling the cell to rapidly react when local access to chromatin is required (Ayoub et al., 2008). Intriguingly, this organization of spatial chromatin states has been found to involve phase-separation behavior, dependent on multivalent interactions (Larson et al., 2017;

Strom et al., 2017). Due to the complexity of multivalent effector–chromatin interactions, it is however not well understood how HP1 proteins are dynamically recruited and retained at their target sites and how they contribute to establishing the heterochromatin state. It is thus of importance to determine how the local arrangement (chromatin conformation) and nature of binding sites on the chromatin fibers (histone PTMs or other structural features) control dynamic HP1 association.

To investigate the dynamic interactions between effectors and modified chromatin we employed a single single-molecule total internal reflection fluorescence (smTIRF) imaging approach. In combination with mathematical modeling, it could be shown that the recruitment and retention kinetics of a key effector, HP1 $\alpha$ , to modified chromatin fibers is dependent on multiple factors, including the density of PTMs in the chromatin substrate. Moreover, we proposed a model for chromatin interactions, based on a kinetic capture mechanism. According to this model, effectors are dynamically trapped by sequential binding, dissociation and re-binding reactions in the high-avidity environment of a chromatin fiber, carrying PTMs. From such a model, it follows that the interaction dynamics of multivalent effectors with chromatin depend on structural features of the chromatin fiber, modulating the local concentration of binding sites.

## 2.2 Experimental data

We used single-molecule total internal reflection fluorescence (smTIRF) imaging to measure the binding kinetic of the different HP1 subtypes (Figure 2.1A). Therefore, Chromatin fibers were immobilized in PEG-passivated flow chambers and imaged in the far-red channel to determine the location of the chromatin fibers. Then labeled HP1 is injected into the flow chamber, and the binding events are detected by single-molecule colocalization. Therefore, a binding event is detected by exact matching of the positions of the fluorescent emitter with the localization of the chromatin (Kilic et al., 2015) (Figure 2.1B). From the recorded movies, fluorescence emission traces were extracted for each chromatin position. The kinetic traces showed transiently bound HP1 proteins as peaks in fluorescence emission (Figure 2.1C). Cumulative lifetime-histograms were constructed from the detected interaction events and analyzed. All HP1 subtypes exhibited bi-exponential dissociation kinetics for all HP1 subtypes (Figure 2.1D, Table 2.1), while the association kinetics were well described with single-exponential kinetics (Figure 2.1E and Table 2.1).

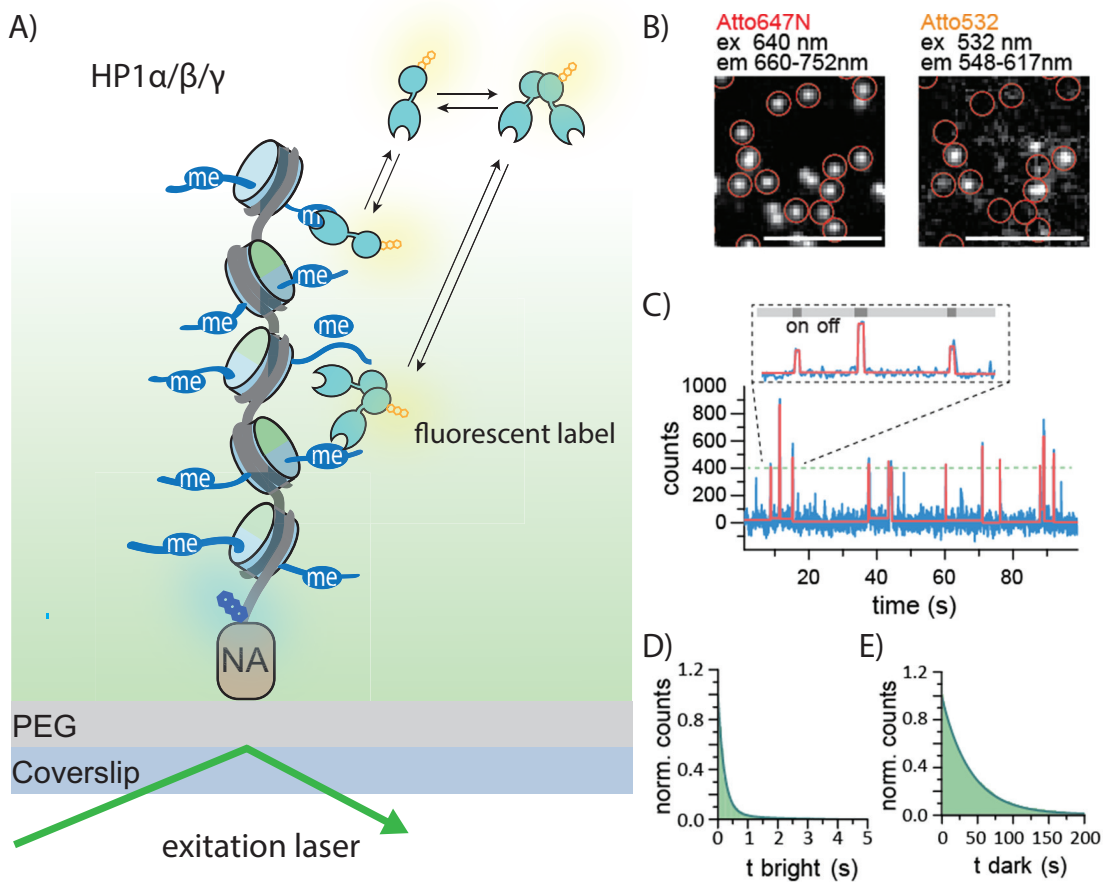


Figure 2.1 – Detection of effector–chromatin interactions on the single-molecule level. A) Schematic representation of the smTIRF imaging experimental setup showing HP1 interacting with a chromatin fiber B) Representative microscopy images showing the localization of the chromatin fibers (left panel) and individual HP1 $\alpha$  molecules bound to chromatin (right panel). The scale bar is 5  $\mu$ m. B) Characteristic time trace (blue) of HP1 $\alpha$  binding dynamics to a single chromatin fiber and fitted with a step function (red). Each intensity peak represents one binding event. C) Dissociation kinetics: cumulative histograms of HP1 $\alpha$  dwell times of 100 traces fitted with a double-exponential function. D) Association kinetics: cumulative histogram of times between each binding event of the same 100 traces, fitted with a mono-exponential function

Table 2.1 – Fit results from smTIRF measurements of HP1 $\alpha$ ,  $\beta$  and  $\gamma$  chromatin interactions. \*Values taken from Kilic et al. (2015)

Chromatin	Effector	$\tau_{off,1}$ (s)	$A_1$ (%)	$\tau_{off,2}$ (s)	$A_2$ (%)	$k_{on}$ ( $M^{-1}s^{-1}$ ) $\times 10^6$	$n$
H3K9me3*	HP1 $\alpha$	$0.25 \pm 0.03$	$87 \pm 7$	$2.26 \pm 1.22$	$13 \pm 7$	$3.64 \pm 1.56$	16
H3K9me3	HP1 $\beta$	$0.19 \pm 0.03$	$95 \pm 2$	$3.60 \pm 1.13$	$5 \pm 2$	$0.67 \pm 0.19$	12
H3K9me3	HP1 $\gamma$	$0.17 \pm 0.02$	$93 \pm 3$	$2.64 \pm 0.48$	$7 \pm 3$	$0.89 \pm 0.23$	6

## 2.3 Mathematical model

To dissect the detailed mechanisms of HP1-chromatin binding dynamics, the binding process is modeled in an unbiased way. The result is a kinetic model that accounts for all conceivable interactions between mono- ( $X$ ) or dimeric HP1 ( $Y$ ) and histone and DNA sites on the chromatin fibers and their respective transitions. The kinetic model considers all elementary steps of protein - chromatin interactions, up to third-order reactions. The protein monomers (denoted by  $X^{ij}$ ) it has the ability to form homodimers (denoted by  $Y^{ij}$ ), it can remain unbound (superscript 0), bind unspecifically to DNA (indicated by superscript 1) or specifically to the histone PTM, H3K9me3 (indicated by the superscript 2). The model assumes that protein monomers can either bind to a section of the DNA or to a PTM binding site. In a dimer, on the other hand, the individual protomers to bind independently to either a DNA binding site or to the histone PTM. Thus, dimers can bind in a monovalent mode as HP1:HP1:DNA ( $Y^{01}$ ), HP1:HP1:H3K9 ( $Y^{02}$ ) or in a bivalent mode as DNA:HP1:HP1:DNA ( $Y^{11}$ ), DNA:HP1:HP1:H3K9 ( $Y^{12}$ ), H3K9:HP1:HP1:H3K9 ( $Y^{22}$ ). In addition to the binding and unbinding of the proteins to DNA and H3K9 the model considers migration of chromatin-bound proteins between binding. Such migrations occur, for example, if DNA-bound proteins slide along the DNA and then bind to a modified histone tail. In order to avoid biasing the model due to its structure, all possible migration reactions up the third order are considered. Thus, dimers can migrate from monovalent bound states to bivalent bound states as well as from DNA bound states to PTM bound states and vice-versa. A rules-based modeling tool BioNetGen (Faeder et al., 2009) is then used to generate an extended reaction network from the simple reactions rules defined above, resulting in the reaction network shown in figure 2.2.

The overall parameter space is reduced by introducing thermodynamics constraints (Table 2.2). Additionally, we assume that the free energy difference of binding to a single site is the same for monomers and dimers:  $K_{0|1} \equiv K_{00|01}$  and  $K_{0|2} \equiv K_{00|02}$ . The complete mathematical model also accounts for incomplete fluorescent labeling of HP1. Thus, every monomer can exist in a labeled and unlabeled form. The ordinary differential equations (ODEs) of the reaction system were solved using the CVODE solver from the SUNDIALS toolbox for MATLAB (Serban and Hindmarsh, 2005; Hindmarsh et al., 2005).

## 2.4 Parameter identification

In the next step, we aim to find parameters that enable us to reproduce the experimentally observed behavior. We, therefore, used a variant of the genetic multi-objective optimization

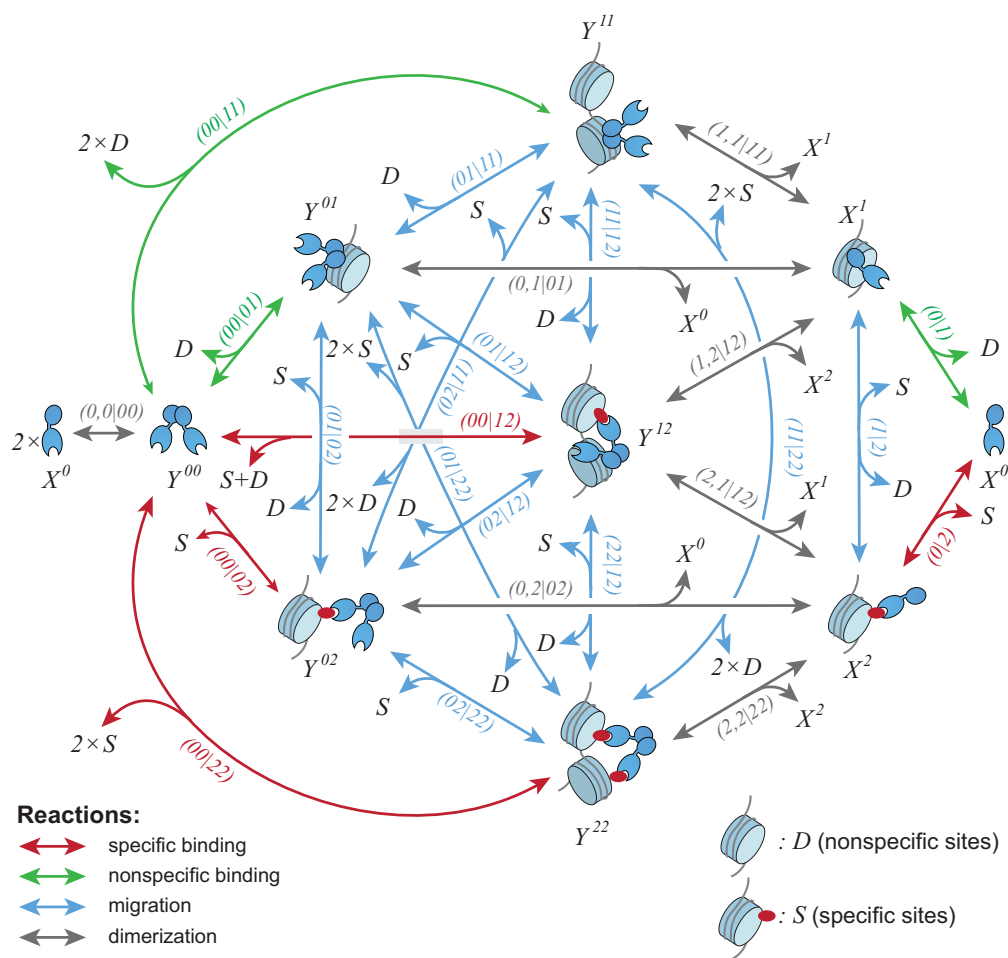


Figure 2.2 – Full reaction network model of HP1 chromatin interactions. All reactions between the indicated states are reversible and governed by equilibrium and rate constants.

algorithm (NSGA-II) (Deb et al., 2002) to generate a population of parameter sets for the kinetic model that match the experimental data. The NSGA-II provides a multi-objective selection algorithm to select parameter sets close to the Pareto front of the objectives. The selection of Pareto optimal parameter sets allows extracting possible trade-off when fitting to multiple data sets simultaneously. In addition to the Pareto optimal selection function, we used a Gaussian mutation function to sample the parameter space robustly within the initially set bounds. We then tuned the parameters of the Gaussian mutation function to capture the Pareto front of the two objective functions used. We chose this genetic algorithm multi-objective as it allows us to sample the parameter space along the Pareto front and, at the same time, generating a robust parameter population within the predetermined search space. The generated parameter populations further allow us to provide a measure of uncertainty for the individual parameter set giving us insight into which parameters are more constraint by

Table 2.2 – Thermodynamic constraints on the equilibrium parameters

$K_{0,1 01} = K_D \frac{K_{00 01}}{K_{0 1}}$	$K_{01 02} = \frac{K_{00 02}}{K_{00 01}}$	$K_{1,1 11} = K_D \frac{K_{00 01}}{K_{0 1}}$
$K_{0,2 02} = K_D \frac{K_{00 02}}{K_{0 2}}$	$K_{01 11} = \frac{K_{00 11}}{K_{00 01}}$	$K_{2,2 22} = K_D \frac{K_{00 02}}{K_{0 2}}$
$K_{1 2} = \frac{K_{0 2}}{K_{0 1}}$	$K_{02 22} = \frac{K_{00 22}}{K_{00 02}}$	$K_{22 12} = \frac{K_{00 12}}{K_{00 02} K_{00 22}}$
$K_{11 12} = \frac{K_{00 12}}{K_{00 01} K_{00 11}}$	$K_{11 22} = \frac{K_{00 02} K_{00 22}}{K_{00 01} K_{00 11}}$	$K_{01 22} = \frac{K_{00 02} K_{00 22}}{K_{00 01}}$
$K_{02 12} = \frac{K_{00 12}}{K_{00 02}}$	$K_{01 12} = \frac{K_{00 12}}{K_{00 01}}$	$K_{02 11} = \frac{K_{00 01} K_{00 11}}{K_{00 02}}$

the experimental data and which ones are less determined. It shall be noted here that we did not compare the performance of this parameter identification algorithm with other parameter identification methods that provide similar features as such an analysis was not in the scope of this work.

To compare the kinetic model with the single-molecule data, we perform association and dissociation simulations, where we first HP1 introduce at the nominal concentration and solve the set of ODEs until the chemical equilibrium is reached, using the equilibrium concentrations of bound HP1 as initial conditions a second simulation performed were the initial free HP1 concentration is zero. We then measure the characteristic times scales necessary for the HP1 to dissociate from the chromatin by fitting a double exponential of the form  $A_{1,det} \exp(t/\tau_{1,off}) + A_{2,det} \exp(t/\tau_{2,off})$  to the normalized decay curve. We compare the relative amplitudes of the deterministic model with the relative amplitudes of the the experimental data, as the amplitudes from the experimental data are obtained from a cumulative histogram data, we have to scale the amplitudes of the ODE model relative to their respective time scales  $A_{2,sim} = A_{2,det}/\tau_2 / (A_{1,det}/\tau_1 + A_{2,det}/\tau_2)$ . To train the model parameters, we used the results of the single-molecule TIRF experiments with HP1 $\alpha$  at 1 nM concentration and with HP1 $\beta$  at 5 nM concentration (Table 2.1). We assigned each experiment an objective function that compares the dissociation times  $\tau_1, \tau_2$ , the scaled relative exponential fraction  $A_2$  as well as the equilibrium amount of adsorbed protein at equilibrium  $N_0 = [HP1]V N_a$  with the experimental results. The objective for each experiment is then calculated as:

$$R = \sqrt{\left(\frac{|N_{0,exp} - N_{0,sim}|}{N_{0,exp}}\right)^2 + \left(\frac{|\tau_{1,exp} - \tau_{1,sim}|}{\tau_{1,exp}}\right)^2 + \left(\frac{|\tau_{2,exp} - \tau_{2,sim}|}{\tau_{2,exp}}\right)^2 + \left(\frac{|A_{2,exp} - A_{2,sim}|}{A_{2,exp}}\right)^2} \quad (2.1)$$

To simplify the parameter estimation, we used dimensionless quantities to describe our system. The only independent units of our system are concentration and time. Thus we scale our system using a characteristic concentration  $c_{ref} = [HP1]_{tot}$  and a characteristic time  $t_{ref} = r_{D,ref} [HP1]_{tot}$ . Here we chose the characteristic concentration to be  $[HP1]_{tot}$  the

## Chapter 2. Modeling of multivalent protein binding on chromatin

Table 2.3 – A list of all dimensionless model variables given a short description and expression in terms of the reference concentrations.

Symbols	Description	Expression
$X_0$	Unbound monomeric HP1 concentration	$\frac{[HP1]}{[HP1]_{tot}}$
$Y_{00}$	Unbound dimeric HP1 concentration	$\frac{[2HP1]}{[HP1]_{tot}}$
$D$	Concentration of free DNA binding sites	$\frac{[HP1]_{tot}}{[DNA]}$
$S$	Concentration of free PTM binding sites (H3K9)	$\frac{[HP1]_{tot}}{[H3K9]}$
$X_1$	Monomeric, DNA bound HP1 concentration	$\frac{[HP1:DNA]}{[HP1]_{tot}}$
$Y_{01}$	Dimeric, monovalent DNA bound HP1 concentration	$\frac{[2HP1:DNA]}{[HP1]_{tot}}$
$Y_{11}$	Dimeric, bivalent 2xDNA bound HP1 concentration	$\frac{[HP1:2DNA]}{[HP1]_{tot}}$
$Y_{12}$	Dimeric, DNA and PTM bound HP1 concentration	$\frac{[H3K9:2HP1:DNA]}{[HP1]_{tot}}$
$X_2$	Monomeric, PTM (H3K9) bound HP1 concentration	$\frac{[HP1:H3K9]}{[HP1]_{tot}}$
$Y_{02}$	Dimeric, monovalent, PTM (H3K9) bound HP1 concentration	$\frac{[H3K9:2HP1]}{[HP1]_{tot}}$
$Y_{22}$	Dimeric, bivalent PTM (2H3K9) bound HP1 concentration	$\frac{[2H3K9:2HP1]}{[HP1]_{tot}}$

Table 2.4 – A list of all dimensionless model variables given a short description and expression in terms of the reference concentrations.

Symbols	Description	Unit	median	lower quartile	upper quartile
$K_D$	Dimerization	$\mu\text{M}$	0.36	0.30	1.92
$K_{1,2 12}$	1D mixed Dimerization	$\mu\text{M}$	62.15	42.68	70.42
$K_{0,1}$	Monomer DNA bound	$\mu\text{M}$	6.19	4.54	8.12
$K_{00,01}$	Dimer monovalent DNA bound	$\mu\text{M}$	6.19	4.54	8.12
$K_{00,11}$	Dimer bivalent DNA bound	$\mu\text{M} \times \text{M}$	$2.20 \times 10^{-4}$	$1.79 \times 10^{-4}$	$5.81 \times 10^{-4}$
$K_{0,2}$	Monomer PTM bound	$\mu\text{M}$	8.35	1.74	11.76
$K_{00,02}$	Dimer monovalent PTM bound	$\mu\text{M}$	8.35	1.74	11.76
$K_{00,12}$	Dimer bivalent DNA-PTM bound	$\mu\text{M} \times \text{M}$	$9.10 \times 10^{-5}$	$2.75 \times 10^{-5}$	$3.03 \times 10^{-4}$
$K_{00,22}$	Dimer bivalent DNA-PTM bound	$\mu\text{M} \times \text{M}$	$9.30 \times 10^{-5}$	$8.11 \times 10^{-5}$	$3.72 \times 10^{-3}$

overall concentration of protein. The characteristic time is derived from a reference value for the dimerization rate  $r_{D,ref}$  assumed to be  $10^6 \text{M}^{-1} \text{s}^{-1}$ . The resulting dimensionless variables are listed in Table 2.3, and a description of the dimensionless parameter can be found in Table 2.4 and Table 2.5. We performed the parameter optimization using the data of HP1 $\alpha$  and HP1 $\beta$ , inferring the relative difference in their DNA and PTM binding constants (Hiragami-Hamada et al., 2011; Nishibuchi et al., 2014). From the results of the genetic algorithm, we obtained 168 parameter sets with different parameter combinations. For the investigations presented in this work, we used either the median of these populations as parameters for the model (Tables 2.4 and 2.5) or we simulated all parameter sets, e.g. to compare the sensitivities across the parameter population.



## 2.4. Parameter identification

Table 2.5 – A list of all dimensionless forward rates. The first half of the table denotes the reaction rates for the three-dimensional reactions and the second half of the table denotes the reaction rates for the migration rates.

Symbols	Description	Unit	median	lower q.	upper q.
$k_D$	Dimerization	$M^{-1} s^{-1}$	$1.12 \times 10^7$	$5.88 \times 10^6$	$2.16 \times 10^7$
$k_{0 1}$	Monomer DNA binding	$M^{-1} s^{-1}$	$5.75 \times 10^5$	$4.91 \times 10^5$	$7.93 \times 10^5$
$k_{0 2}$	Monomer PTM binding	$M^{-1} s^{-1}$	$9.56 \times 10^5$	$3.12 \times 10^5$	$1.32 \times 10^6$
$k_{0,1 01}$	Dimerization of free and DNA bound protein	$M^{-1} s^{-1}$	$1.32 \times 10^5$	$2.29 \times 10^4$	$2.58 \times 10^5$
$k_{0,2 02}$	Dimerization of free and PTM bound protein	$M^{-1} s^{-1}$	$7.93 \times 10^4$	$4.72 \times 10^4$	$1.23 \times 10^7$
$k_{00 01}$	Monovalent, DNA binding of a dimer	$M^{-1} s^{-1}$	$2.01 \times 10^7$	$1.23 \times 10^7$	$7.51 \times 10^7$
$k_{00 02}$	Monovalent, PTM binding of a dimer	$M^{-1} s^{-1}$	$1.33 \times 10^7$	$7.68 \times 10^6$	$1.72 \times 10^7$
$k_{00 11}$	Bivalent, DNA binding of a dimer	$M^{-2} s^{-1}$	$2.55 \times 10^{14}$	$1.38 \times 10^{14}$	$5.22 \times 10^{15}$
$k_{00 22}$	Bivalent, PTM binding of a dimer	$M^{-2} s^{-1}$	$2.07 \times 10^{13}$	$1.03 \times 10^{13}$	$4.04 \times 10^{14}$
$k_{00 12}$	Bivalent, PTM-DNA binding of a dimer	$M^{-2} s^{-1}$	$8.37 \times 10^{13}$	$3.34 \times 10^{13}$	$2.33 \times 10^{14}$
$k_{1,1 11}$	Dimerization of two DNA bound monomers	$M^{-1} s^{-1}$	$1.39 \times 10^{10}$	$5.68 \times 10^9$	$4.27 \times 10^{10}$
$k_{2,2 22}$	Dimerization of two PTM bound monomers	$M^{-1} s^{-1}$	$1.49 \times 10^{11}$	$7.13 \times 10^9$	$3.32 \times 10^{11}$
$k_{1,2 12}$	Dimerization of a PTM and a DNA bound monomer	$M^{-1} s^{-1}$	$6.74 \times 10^9$	$3.37 \times 10^9$	$1.97 \times 10^{10}$
$k_{01 11}$	Migration from monovalent DNA binding to bivalent DNA binding	$M^{-1} s^{-1}$	$8.75 \times 10^{10}$	$2.59 \times 10^{10}$	$1.22 \times 10^{11}$
$k_{02 22}$	Migration from monovalent PTM binding to bivalent PTM binding	$M^{-1} s^{-1}$	$2.41 \times 10^8$	$3.24 \times 10^{10}$	$3.57 \times 10^{11}$
$k_{01 12}$	Migration from monovalent DNA binding to bivalent, PTM-DNA binding	$M^{-1} s^{-1}$	$6.08 \times 10^9$	$4.28 \times 10^9$	$7.17 \times 10^{10}$
$k_{02 12}$	Migration from monovalent PTM binding to bivalent, PTM-DNA binding	$M^{-1} s^{-1}$	$6.74 \times 10^7$	$2.65 \times 10^7$	$1.75 \times 10^8$
$k_{11 12}$	Migration from bivalent, DNA binding to bivalent, PTM-DNA binding	$M^{-1} s^{-1}$	$5.72 \times 10^8$	$5.12 \times 10^8$	$9.49 \times 10^{10}$
$k_{22 12}$	Migration from bivalent PTM binding to bivalent, PTM-DNA binding	$M^{-1} s^{-1}$	$3.67 \times 10^7$	$6.48 \times 10^6$	$1.46 \times 10^{10}$
$k_{11 22}$	Migration from bivalent DNA binding to bivalent, PTM binding	$M^{-2} s^{-1}$	$3.17 \times 10^{18}$	$1.02 \times 10^{18}$	$3.70 \times 10^{19}$
$k_{01 02}$	Migration from monovalent DNA binding to monovalent, PTM binding	$M^{-1} s^{-1}$	$7.75 \times 10^8$	$3.61 \times 10^7$	$1.33 \times 10^{11}$
$k_{1 2}$	Migration of a monomer from DNA binding to PTM binding	$M^{-1} s^{-1}$	$4.08 \times 10^8$	$1.75 \times 10^7$	$2.60 \times 10^9$
$k_{01 22}$	Migration from monovalent, DNA binding to bivalent, PTM binding	$M^{-2} s^{-1}$	$1.02 \times 10^{19}$	$1.10 \times 10^{17}$	$2.67 \times 10^{19}$
$k_{02 11}$	Migration from monovalent, PTM binding to bivalent, DNA binding	$M^{-2} s^{-1}$	$3.37 \times 10^{19}$	$1.22 \times 10^{19}$	$4.43 \times 10^{19}$

### 2.5 Stochastic simulations of protein binding in vitro

We verified our deterministic parameter estimation using stochastic simulations, directly simulating the single molecule binding experiments. To translate the deterministic model into a stochastic simulation we transferred the rate equations into propensities as described by Gillespie (Gillespie, 1977). The stochastic model was then simulated using StochPy (Maarleveld et al., 2013). To evaluate the stochastic simulations, bright and dark times, i.e. the durations a labeled protein is bound to a chromatin array and the times the array remains free, were determined. To this end, we simulated a single chromatin array as 24 H3K9 and 120 DNA binding sites. Subsequently, we compared the simulations to the experiments using cumulative histograms of the bright and dark times. Since the experimental procedure cannot resolve events shorter than 0.05 s these events were removed by a low-pass filter in our simulations. Comparing the complete lifetime histograms in  $\log(t)$  space we clearly can see that the model captures events that are beyond the resolution of the experimental measurement (Figure 2.3 A vs. B). From the simulated cumulative lifetime histograms, observable rate (time) constants are then retrieved (Figure 2.4 B,C), dependent on the input parameters. To vary the overall binding affinity of H3K9me3 and DNA interactions we scaled the free energy of the a single DNA or H3K9me3 binding site. Thus, the binding constants of bivalent bound species are scaled by the a square of the scaling factor for the respective monovalent bound species. These simulations allowed to track the origins of the apparent bi-exponential kinetics observed for HP1 dissociation in the experimental data back to multivalent interactions: simulating HP1 interaction kinetics without multivalent binding did not reproduce the slow kinetic phase ( $\tau_{off,2}$ ) whereas inclusion of multivalency gave rise a population HP1 molecules engaged in long-lived interactions (Figure 2.3 D).

### 2.6 Sensitivity analysis

Our parameterized simulations revealed that the predominant binding pathways involved DNA bound states (Figure 2.4A). Further, we observed that individual observable binding events were composed of multiple rapid transitions between different H3K9me3 and intrinsically short-lived DNA bound states. We then applied our model to better understand how PTM- and DNA-dependent interactions modulate the chromatin recruitment kinetics of HP1 $\alpha$  and HP1 $\beta$ . We thus probed the response of the apparent association ( $k_{on}$ , Figure 2.4B) and dissociation rate constants ( $k_{off} = 1/\tau_{off,1}$ , Figure 2.4C) to changes in either the equilibrium constant for H3K9me3 interactions ( $K_{PTM}$ ) or in the equilibrium constant for DNA binding ( $K_{DNA}$ ). Indeed, when systematically altering  $K_{PTM}$  and  $K_{DNA}$  over two orders of magnitude

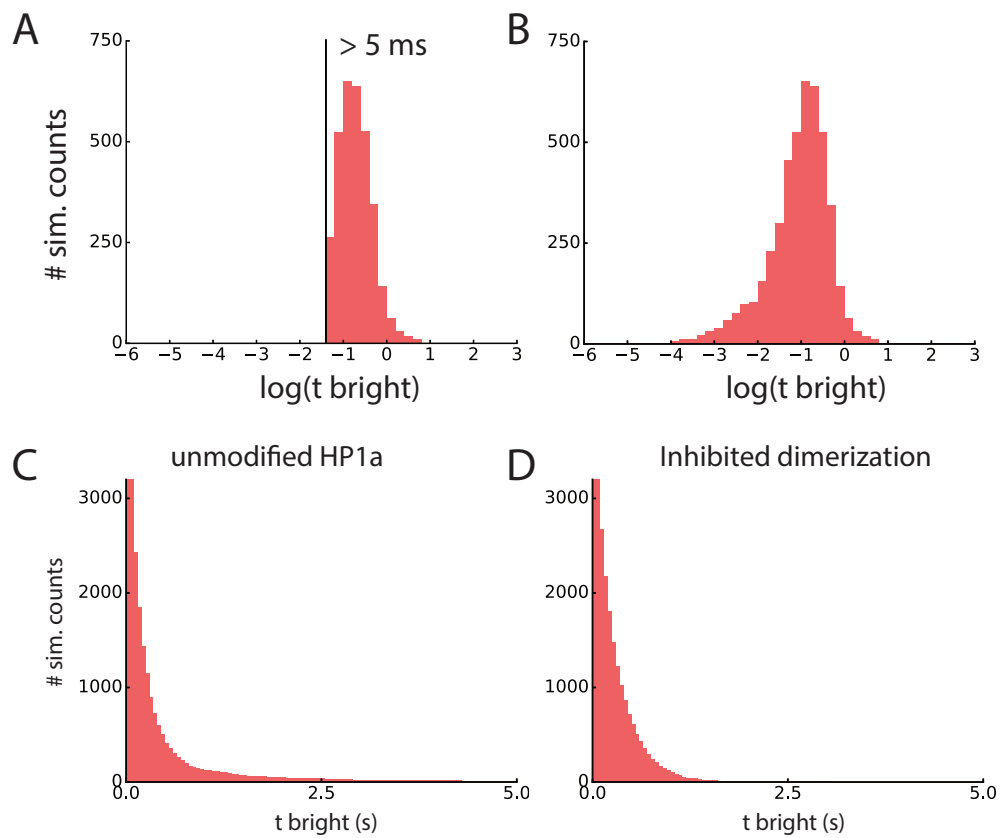


Figure 2.3 – A) Histogram of the events with in log space with event cutoff (left) and B) without event cutoff (right). C-D) Comparison of the stochastic simulations of E) HP1 $\alpha$  wt. with D) a simulation where the dimerization is inhibited i.e. the equilibrium constant of the dimer was increased by a factor of  $10^3$ .

## Chapter 2. Modeling of multivalent protein binding on chromatin

---

around the measured values for the HP1 isoforms ( $\approx 1\text{--}100\mu\text{M}$ ),  $k_{on}$  was found to be more sensitive to changes in  $K_{DNA}$ , whereas HP1 retention on chromatin ( $k_{off}$ ) depended more strongly on  $K_{PTM}$ . Moreover, changes in  $K_{DNA}$  could be partially compensated by respective changes in  $K_{PTM}$  and vice versa. In accordance with results from current and earlier experiments Kilic et al. (2015), this analysis shows that charge-based DNA interactions are instrumental in guiding HP1 proteins to their binding sites.

Finally, our model allowed us to identify the key parameters governing chromatin interactions. We, therefore, performed a global sensitivity analysis on the model. In a global sensitivity analysis, we aim to determine the input parameters that exhibit the largest sensitivity with respect to a set of outputs over i) large ranges of input parameter changes and ii) input parameters changing simultaneously. We, therefore, defined a set of output parameters (bound HP1 concentration, the two apparent dissociation time constants  $\tau_{off,1}$  and  $\tau_{off,2}$  and the percentage of the amplitude of the slow dissociation process  $A_2$ ). The analysis was performed for all the model parameters given in tables 2.4, and 2.5 with the total amount of HP1, varying all parameters randomly within the minimal and maximal values found across all parameters sets. For each parameter variation, we extracted the ten-fold change of the model in- and output for the reference model and used linear regression to extract the most probable trend for the respective parameter. This yields the most probable global effect on the model for a given set of parameters. The indices show whether correlation, anti-correlation, or no-correlation is expected between the respective model output and a parameter, see figure 2.5.

The sensitivity analysis revealed the set of microscopic rate constants that had the largest impact on a set of key observables: the amount of bound HP1, the two apparent residence times ( $\tau_{off,1}, \tau_{off,2}$ ) as well as the fraction molecules engaged in long-lived interactions (i.e. the relative amplitude of the slow process,  $A_2$ ). Apart from the total HP1 concentration and the microscopic rate constants governing binding to DNA and to H3K9me3, HP1 dimerization and a number of internal migration pathways appeared as a key determinant for chromatin retention (Figure 2.5). This allows us to make predictions about how the HP1 dynamics change in a cellular environment. Increasing the local HP1 concentration results in more chromatin bound protein. Cellular proteins that stabilize HP1 dimerization increase the chromatin bound population and prolong the residence times by inducing multivalent states. Contrariwise, an increase in migration reaction rates, potentially stimulated by local competition in the nucleus or active mechanisms such as chromatin remodeling, results in faster HP1 release times as they provide dissociation pathways. Finally, the combination of DNA and PTM interactions are

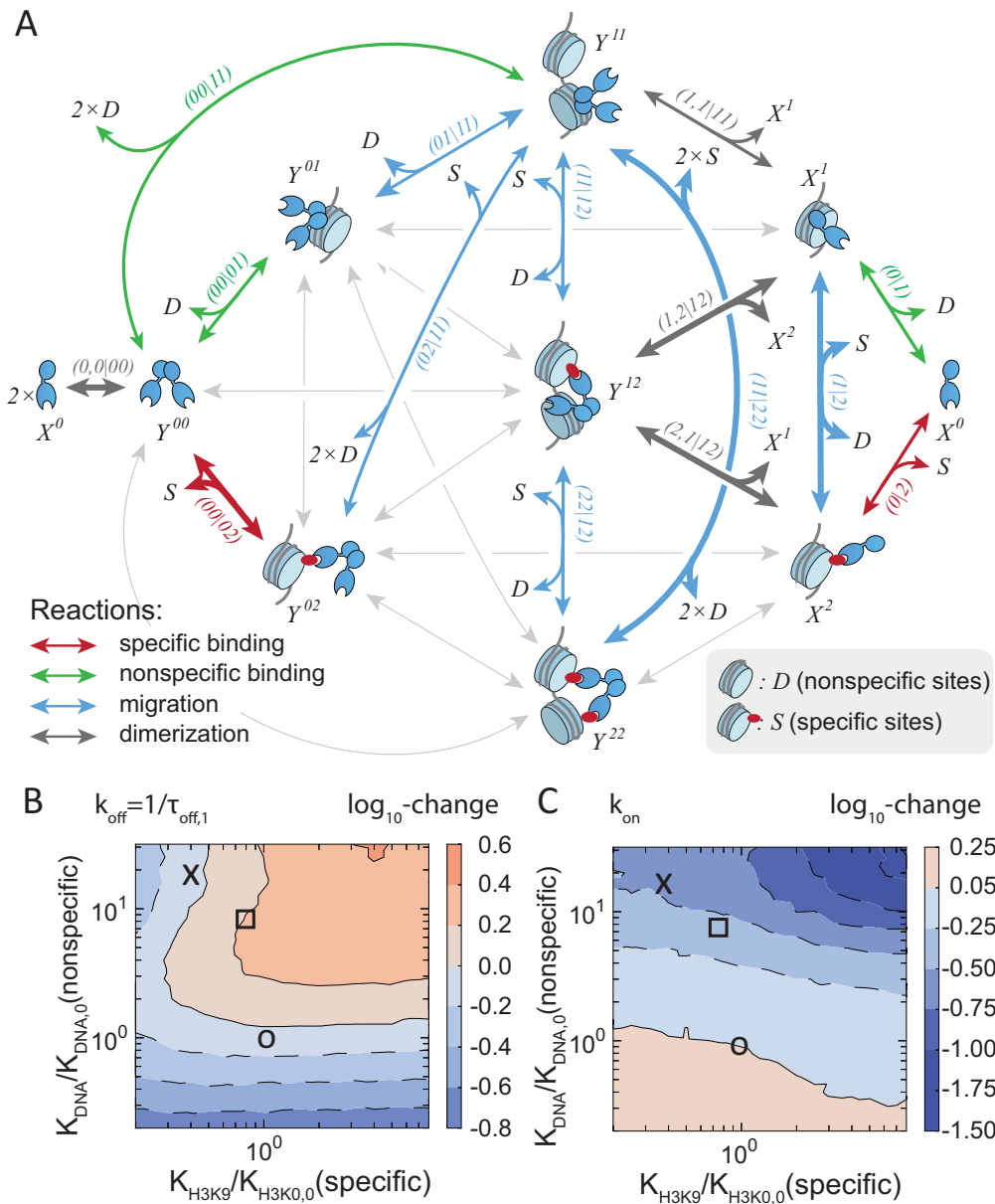


Figure 2.4 – A) Full kinetic model of HP1-chromatin interactions, showing the pathways associated with high flux (arrow thickness). Gray arrows denote reactions associated with low but non-zero flux. Arrowhead size indicates the direction of net flux. B) Dependence of simulated HP1 dissociation rate constants ( $k_{off} = 1/\tau_{off,1}$ ) on relative changes in  $K_{PTM}$  and  $K_{DNA}$ . Parameters for circle: HP1 $\alpha$ , cross: HP1 $\beta$ , square: HP1 $\gamma$ . The color code and contour lines indicate changes in the dissociation on a logarithmic scale. C) Dependence of simulated HP1 binding rate constants ( $k_{on}$ ) on relative changes in methyllysine (KPTM) and DNA (KDNA) interactions. Parameters for O: Parameters for circle: HP1 $\alpha$ , cross: HP1 $\beta$ , square: HP1 $\gamma$ . The color code and contour lines indicate changes in the binding rate on a logarithmic scale.

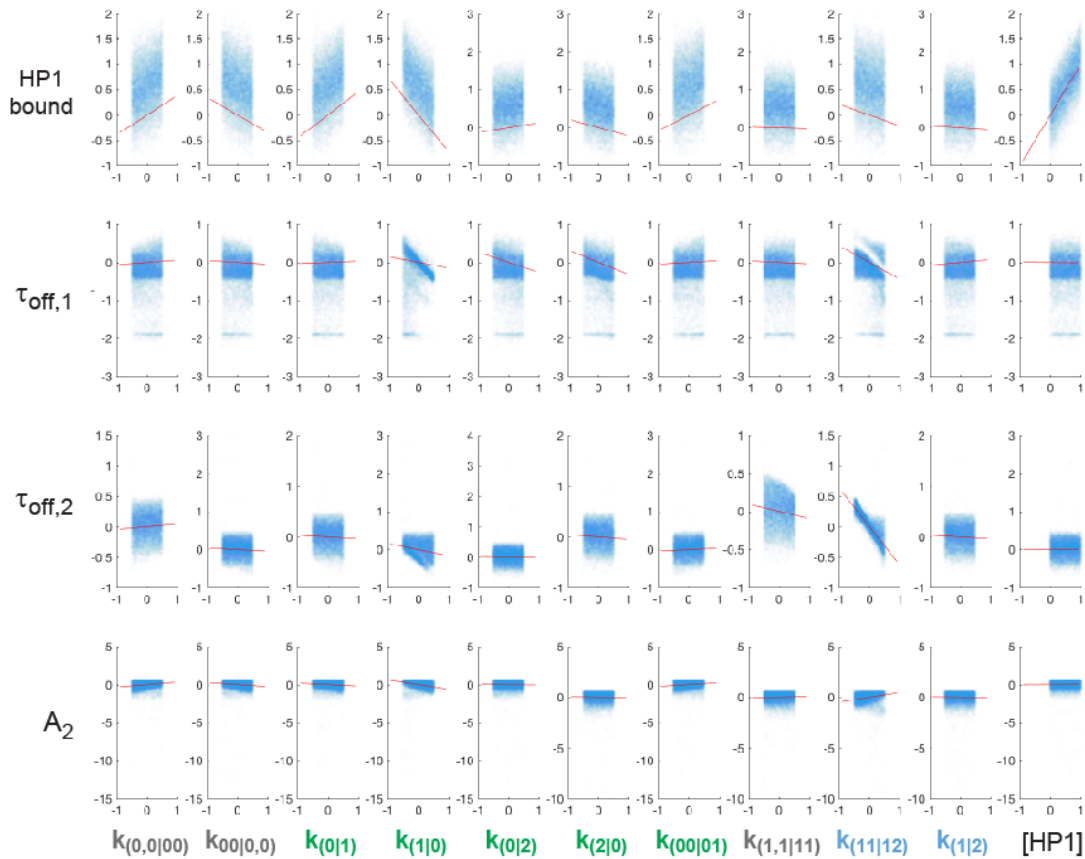


Figure 2.5 – Fold change of the model outputs in GSA. The tenfold change of the model outputs ( $HP1$  bound,  $\tau_{off,1}$ ,  $\tau_{off,2}$ ,  $A_2$ ) is plotted vs the tenfold change of the most important model parameters. Data is given as blue dots. The slope of the red lines indicates the mean fold-change of the output parameters with respect to a fold-change in the input parameter

responsible for chromatin targeting, as DNA binding has strong effects across all parameters, whereas histone PTM binding provides specificity for heterochromatic regions (Figure 2.5).

## 2.7 Discussion

Chromatin presents different chemical and structural features which are integrated by chromatin effectors and transcription factors to enact a biochemical response. Chromatin recognition by multivalent effectors not only depends on the presence of specific histone PTMs in a given chromatin state, but also on their spatial arrangement. Thus, the density of PTMs as well as spatial features, including positioning of nucleosomes, linker DNA lengths, higher order chromatin structure as well as asymmetrical modification patterns (Rhee et al., 2014; Voigt et al., 2012) are an important part of the recognition landscape and determine chromatin

function. In addition to histone PTM-specific readers, effectors often contain additional interaction domains, enabling binding to DNA or RNA, to the nucleosome surface, to transcription factors or to other chromatin associated proteins (Müller et al., 2016; Francis et al., 2004; Son et al., 2013; Zhen et al., 2016). For a quantitative understanding of chromatin recognition, knowledge of these different factors is required.

Here, we probed the relative influences of spatial and chemical features in chromatin on the interaction dynamics on a class of multivalent effectors, the human HP1 family proteins. We employed single-molecule TIRF measurements to directly monitor chromatin binding and dissociation kinetics and, coupled with modeling the complete kinetic system, extracted mechanistic information on these transient interactions. Combined single-molecule experiments comparing all three human HP1 subtypes, together with computational efforts further allowed us to generate a detailed picture of the dominant chromatin interaction pathways. In this dynamic capture model, the most common HP1 recruitment and retention pathways involve charge-dependent DNA interactions, which increase the capture radius for specific sites (i.e. H3K9me3 modified nucleosomes). This situation, where lower-affinity interactions guide an effector protein to its molecular target are reminiscent to the target search of transcription factors (Wang et al., 2009). From initial short-lived dynamic encounter complexes, HP1 molecules can transition into states involving more long-lived PTM-based interactions, either mono-, bivalent or mixed states where DNA and PTMs are simultaneously engaged. Moreover, DNA interactions enable rapid transitions between neighboring nucleosomes, facilitating rapid re-binding after dissociation from H3K9me3. Previous results (Kilic et al., 2015) indicated a critical importance of HP1 dimerization and the thus resulting multivalency. Here, we demonstrate that reducing the strength of charge-based interactions directly lowers the probability of H3K9me3 binding. Simultaneously the residence times of HP1 proteins is decreased as re-binding reactions are disfavoured. For this reason, the HP1 $\beta$  and HP1 $\gamma$  isoforms both exhibit slower binding and reduced chromatin retention in comparison to the HP1 $\alpha$  isoform, in spite of their higher affinity for H3K9me3.

Taken together, we have gained insight into the mechanisms of chromatin interaction by multivalent effectors. Importantly, we have determined a key function of helper-interactions via the DNA in target search and chromatin retention for effector proteins. We propose that this is a general paradigm for chromatin associated proteins. Effectors are transiently trapped by multiple moderate-affinity interactions, and sequential dissociation and re-binding reactions result in effector accumulation in the high-avidity environment of chromatin. Such a dynamic capture mechanism enables a fast response to changes in the local environment or cell state

## **Chapter 2. Modeling of multivalent protein binding on chromatin**

---

(Ayoub et al., 2008; Fischle et al., 2005). It further predicts that the interaction kinetics of effectors with chromatin depend on both the multivalency properties of effectors and the structural features of the chromatin fiber, modulating the local concentration of binding sites. Indeed, protein subdomains or regions conferring DNA or general nucleosome binding properties are commonly encountered among chromatin effectors, e.g. in SUV39H1 (Müller et al., 2016), PRC1 (Francis et al., 2004; Zhen et al., 2016), PRC2 (Son et al., 2013) or BRDT (Miller et al., 2016), in addition to specific PTM reader modules. These interactions are thus required for initial chromatin localization of effector complexes, whereas specific histone PTM recognition directs their accumulation in target chromatin domains



## 3 Particle-based modeling of crowding effects on enzyme kinetics

This chapter is part of work published as: Weilandt, D. R. and Hatzimanikatis, V. (2019). Particle-Based Simulation Reveals Macromolecular Crowding Effects on the Michaelis-Menten Mechanism. *Biophysical Journal*, 117(2):355–368.

All the reasearch in this paper was conducted by Daniel Weilandt under the supervision of Vassily Hatzimanikatis.

### 3.1 Introduction

For this next chapter, we switch gears and focus on the effects that high macromolecular concentrations have on effective enzyme kinetics. The intracellular environment of living cells is a crowded place, about 20–40% of the interior volume occupied by a variety of macromolecules, including proteins, RNA, DNA, and lipids (Ellis, 2001; Minton, 2001). The composition of the intracellular mixture depends considerably varies between organisms, the cell types, and their environment. Even within a single cell, the density and sizes of macromolecules vary between depending on the location and the compartment (Zhou and Qin, 2013; Aon and Cortassa, 2015; Hancock, 2004). So is the center of bacterial cells, the location of most DNA, a region with increased density compared to the remaining cytosol (Spitzer and Poolman, 2013). The presence of such massive amounts of macromolecules impacts the properties of molecules in the cytosol, as diffusion constants, the conformation of proteins their folding process and aggregation properties, catalytic rates of enzymes, and enzyme-substrate affinities (Poggi and Slade, 2015; Yadav, 2013; van den Berg et al., 1999). In consequence, these changed properties are governing the properties of the biochemical reaction networks that implement the various cellular functions necessary for translation, transcription, signaling,

### Chapter 3. Particle-based modeling of crowding effects on enzyme kinetics

---

and metabolism. Often components of these cellular systems are studied *in vitro* to determine their characteristic parameters since such studies allow to perturb isolated subsystems and often enable experiments, not permissible *in vivo*. Such experiments generate data under well-controlled conditions and to characterize the individual parts of the system. A prominent example of such a study is the characterization of enzyme kinetics as a submodule of metabolism, first performed by Michaelis and Menten (1913). Thereby the rate of substrate conversion of an enzyme extract is measured with varying substrate concentration to enable the characterization of the effective reaction rate law. Such *in vitro* characterizations are usually performed in dilute, homogenous conditions (Brooks et al., 2004), whereas reactions in the cytoplasm occur in the inhomogeneous and densely packed environment described above.

Today computational models are used to analyze and predict cell physiology. Although these studies are continuously improved through the integration of experimental data obtained *in vivo*, such as metabolomics and fluxomics, they are mostly limited in their frequent reliance on *in vitro* characteristics to parameterize their models directly (Emiola et al., 2015; Watterson et al., 2013), reduce uncertainty (Andreozzi et al., 2016a,b), or to evaluate predicted parameters (Khodayari et al., 2014). The extensive use of *in vitro* data in physiological models results in the actual enzyme *in vivo* characteristics not being captured such that the model predictions from these studies might deviate significantly from the ones measured *in vitro*.

The relevance of environmental impact on enzyme kinetics is therefore an important topic of study, especially in terms of crowding in the densely packed intracellular space. In early studies of crowded enzyme catalysis, it was believed that the main effect of diffusion-limited Michaelis-Menten kinetics was caused by altered, anomalous diffusion accompanied by increased effective concentrations. These studies were limited, however, in that volume exclusion effects caused by the reactive partners themselves were often neglected, which results in the change in activity due to interaction with macromolecules not being captured (Zimmerman and Trach, 1991; Schnell and Turner, 2004; Grima and Schnell, 2006b; Klann et al., 2011). A more recent work on the subject was presented by Mourao et al. (2014), in which fractal behavior, indicating that the diffusion and the apparent order of the elementary reactions is altered, was studied using a lattice-based model for an irreversible Michaelis-Menten mechanism. They showed that fractal kinetics only occur under very restrictive conditions, suggesting that it might be less common than previously assumed.

Further recent work has shown that the effective rate constant for bimolecular reactions changes under crowded conditions (Berezhkovskii and Szabo, 2016; Galanti et al., 2016).

Berezhkovskii and Szabo demonstrated that it is possible to express the effective rate for bimolecular reactions as a function of a crowding-induced interaction potential between two reaction partners, which results from an interaction with the surrounding particles when two reactants are in contact. Repulsive interactions between the reactants and particles would, therefore, result in an attractive effective potential between the reactants and vice versa. Relatedly, it has been shown that for rate-limited reactions, the influence of diffusion is minimal, indicating that the effective crowding-induced interaction potential might be more dominant for some enzymatic reactions (Benichou et al., 2010).

Because of its importance in modeling *in vivo* systems, the effects of crowding on biochemical reactions have been extensively studied by various computational and experimental methods, as seen in several reviews (Ellis, 2001; Minton, 2001; Shim et al., 2017). Most of the effort in these studies have been directed toward investigating the impact of diffusion in fractal media on the reaction kinetics (Benichou et al., 2010), with little focus on characterizing the effect of crowding on the mean effective enzyme kinetics. However, because it has now been shown that *in vitro*, some enzymes might not be limited by their translational diffusion but by their apparent association rate constants (Bar-Even et al., 2011; Vijaykumar et al., 2017; Ivancic et al., 2018; Cross et al., 2018; Westerhoff and Welch, 1992), the reevaluation of crowding in these reactions is important.

In this work, therefore, we introduced computational methods for studying spatial effects of any kind, applying our work to the effects of crowding on reaction-limited enzymes with the goal of bridging the discrepancy between the *in vitro* measurement of kinetic parameters and the actual *in vivo* conditions. The proposed method will also allow for studying the differences in the impact of spatial effects for single reactions and for integrated reaction networks. Although the scope of this work is the study of a reaction-limited system, we further evaluated the performance of the proposed method for a simple system under diffusion-limited conditions.

In contrast to the previous studies on the Michaelis-Menten kinetics, which used a diffusion-limited irreversible reaction scheme, we studied the effect of crowding on enzyme kinetics by employing a fully reversible reaction scheme and present herein an example with a representative catalytic activity and affinities that result in a reaction-limited enzyme. Additionally, our molecular particle model accounts for volume exclusion and the diffusion of all species, including reactants and crowding agents, and this was used to study the effect of different size distributions of crowding agents on reaction kinetics.

### Chapter 3. Particle-based modeling of crowding effects on enzyme kinetics

---

Previous studies on crowding conditions were often limited by their computational cost and lack of global insight into the sensitivity of the reaction kinetics or are missing a direct connection to the first physical principles. They often use spatial simulation techniques to simulate multiple realizations of reaction trajectories to determine the influence on the effective kinetics under very specific conditions, meaning that these studies only gain insight into the local sensitivity of the kinetics with respect to the crowding conditions. Furthermore, it is computationally very expensive to resolve the reaction trajectories from particle simulations for reaction-limited reactions because the timescale to resolve the diffusion of the particle is up to seven orders of magnitude faster than the reaction timescale. This requires billions of time steps to be solved for tens of thousands of particles, resulting in a month of simulation time for a single trajectory (Feig and Sugita, 2013). An effective approach to reduce the computational complexity of the Brownian is the crowder-free formulation of the Cichocki-Hinsen algorithm (Cichocki and Hinsen, 1990), which has been validated for homogenous and locally homogenous crowding conditions (Smith and Grima, 2017). Whether the validity of the homogenous or local homogenous crowding assumption holds for inert molecules with a diverse size distribution remains to be examined and shall be discussed elsewhere. Another way to overcome the computational challenges is mesoscopic formulations based on the reaction-diffusion master equation (Grima and Schnell, 2007; Hattne et al., 2005). These formulations require additional models to capture the microscopic effect of obstacles on the macroscopic rate constant, meaning that they can capture the effect of obstacles on the apparent transport coefficient but need additional models to capture how the microscopic collision dynamics are altered.

In this chapter, we resolve these challenges with a new, to our knowledge, formulation entitled generalized elementary kinetics (GEEK). The formulation allows us to characterize kinetic mechanisms that are influenced by various spatial effects, including volume exclusion, confinement (one-dimensional/two-dimensional diffusion), strong and weak interaction forces, localization, or any combination of similar phenomena. In this work, we use a coarse-grained particle model based on HSRB to parameterize this formulation, which can be used in a straightforward way to build ordinary differential equation (ODE) models that use power-law approximations to capture the characteristics of spatial effects and to directly quantify the impact of fractal diffusion. The formulation presented here is achieved by a regression model that is trained from data governed by simulating the microscopic diffusion and collisions from the first physical principle. For the workflow, any kind of simulation algorithm with single molecule detail can be used. Possible alternatives are, for example, the Cichocki-Hinsen algorithm (Cichocki and Hinsen, 1990), the reaction Brownian dynamic algorithm (Morelli

and ten Wolde, 2008), the Green's function reaction dynamics algorithm (van Zon and ten Wolde, 2005), smoldyn (Andrews et al., 2010), or Readdy (Schoneberg and Noe, 2013). In this work, we used an algorithm that combines hard-sphere Brownian dynamics (Strating, 1999) and Brownian reaction dynamics (Allen, 1980; Northrup et al., 1984; Wilson et al., 2018; Kim et al., 2014).

We applied our method to the investigation of macromolecular crowding on the function of phosphoglycerate mutase (PGM) in *Escherichia coli*. Our example clearly demonstrates that accounting solely for an increased local concentration and anomalous diffusion is not sufficient to properly describe crowding effects. We show that a mechanism-dependent effect emerges upon crowding that is facilitated by an increase in both product and substrate association activity and a decrease in the dissociation activity. For reversible Michaelis-Menten kinetics, these effects result in an increase in the binding affinity for the product and substrate as well as a decrease in the maximal reaction rate. Finally, we investigated the effects of crowding on a linear pathway, in which we show that crowding can significantly redistribute the relative flux responses with respect to enzyme overexpression, indicating that the impact of altered kinetics is also propagated on a network level.

## 3.2 Modeling enzyme kinetics

### 3.2.1 Approximation of non ideal enzyme kinetics

In this study the focus is to investigate the effects of crowding on a two step Michaelis-Menten mechanism. In this mechanism a substrate S binds to an enzyme E to form a complex ES via a reversible reaction, which can reversibly transform the substrate and reversibly dissociate the product P. The overall reaction scheme is given below:



where  $k_{1,f}$ ,  $k_{1,b}$ ,  $k_{2,f}$  and  $k_{2,b}$  denote the rate constants of the elementary reactions. The typical form of the reaction rate  $v$  as a function of substrate and product concentrations (see equation (3.2)) is derived from the assumption that all enzymes are conserved such that  $[ES] + [E] = [E_T]$ , where  $[E_T]$  denotes the total enzyme concentration and the enzyme-substrate complex concentration  $[ES]$  is in a quasi-steady state, i.e.,  $d[ES]/dt \approx 0$  (Heinrich

### Chapter 3. Particle-based modeling of crowding effects on enzyme kinetics

---

and Schuster, 1996):

$$v([S], [P]) = \frac{V_M^+ \frac{[S]}{K_{M,S}} - V_M^- \frac{[P]}{K_{M,P}}}{1 + \frac{[S]}{K_{M,S}} + \frac{[P]}{K_{M,P}}} \quad (3.2)$$

where the parameters  $V_M^+$ ,  $V_M^-$ ,  $K_{M,S}$  and  $K_{M,P}$  are related to the elementary rate constants  $k_{1,f}$ ,  $k_{1,b}$ ,  $k_{2,f}$ ,  $k_{2,b}$  and the total enzyme concentration  $[E_T]$  via the relations shown in the equations below.

$$V_M^+ = k_{2,f}[E_T] \quad (3.3a)$$

$$V_M^- = k_{1,b}[E_T] \quad (3.3b)$$

as well as

$$K_{M,S} = \frac{k_{1,b} + k_{2,f}}{k_{1,f}} \quad (3.4a)$$

$$K_{M,P} = \frac{k_{1,b} + k_{2,f}}{k_{2,b}} \quad (3.4b)$$

The parameters of the steady-state reaction rate  $V_M^+$ ,  $V_M^-$ ,  $K_{M,S}$  and  $K_{M,P}$  as well as the elementary rate constants  $k_{1,f}$ ,  $k_{1,b}$ ,  $k_{2,f}$  and  $k_{2,b}$  are related to the overall equilibrium constant of the two reactions:

$$K_{eq} = \frac{k_{1,f}}{k_{1,b}} \frac{k_{2,f}}{k_{2,b}} = \frac{V_M^+ K_{M,P}}{V_M^- K_{M,S}} \quad (3.5)$$

By introducing inert molecules a modification of the effective rate constants is observed due to a change in the diffusion and the collision dynamics. In the most general case, this can, compared to mass-action kinetics, result in a change of the effective order and effective rate constant. Berezhkovskii and Szabo showed that the effective steady state (Collins-Kimball) reaction rate constant  $k_{CK}$  for a diffusion-influenced, irreversible, bimolecular reaction under crowded conditions can be modeled in terms of an altered diffusion constant  $D_1$  and an external crowding-induced interaction potential  $\Delta U$  between the two reacting species. This potential is an implicit representation of the interaction of the individual reactant species with the molecules in their environment and whether these interactions keep the reactants in contact or if they are tearing them apart. The expression for the Collins-Kimball rate constant

was found to follow that described by Berezhkovskii and Szabo (2016):

$$k_{CK} = \frac{4\pi D_1 R k_0 e^{\Delta U \zeta}}{4\pi D_1 R + k_0 e^{\Delta U \zeta}} \quad (3.6)$$

where  $k_0$  is the reaction rate upon collision and  $\zeta$  the the inverse of the thermal energy  $(k_B T)^{-1}$  with  $k_B$  denoting the Boltzman constant and  $T$  the absolute temperature.

To approximate this deviation of the effective elementary rate constants - indicated by  $k_{j,eff}$ , where  $j \in [(1, f), (1, b), (2, f), (2, b)]$  - from the reaction constants in ideal (dilute) conditions  $k_{j,0}$  the effective reaction rates are described as a power law:

$$k_{j,eff}(\phi, \mathbf{X}) = k_{j,0} e_j^{\beta} \prod_{i=0}^N \left( \frac{[X_i]}{[X_i]_0} \right)^{\alpha_{ij}} \quad (3.7)$$

where  $\alpha_{ij}$  are the coefficients quantifying the effect of one of the  $N$  reactants on the effective rate of reaction  $j$  and  $\beta_j$  is the effctive reaction rate constant relative to the ideal reaction constant at the reference concentrations  $[X_i]_0$ .

#### 3.2.2 Generalized elementary Michaelis-Menten kinetics

Given the generalized elementary rate laws, the quasi-steady-state approximation for the Michaelis-Menten reaction rate with GEEK can be defined. Therefore, it can be assumed that the enzyme is conserved,  $[ES] + [E] = [E_T]$ , and the enzyme complex is in a quasi-steady state, i.e.,

$$\frac{d[ES]}{dt} = v_{1,f} - v_{1,b} - v_{2,f} + v_{2,b} \approx 0 \quad (3.8)$$

where each flux  $v_j$  is given by a generalized rate law as given in equation 3.7. For the case of  $\alpha_{i,j} \in \mathcal{R}$  and  $\alpha_{i,j} \neq 0$ , it is not possible to obtain an explicit expression for the reaction rate  $v_{net,qss}$ . To calculate the amount of enzyme-substrate complex in the quasi-steady state for a given  $[E_T]$ ,  $[S]$ , and  $[P]$ , the conservation relation  $[E] = [E_T] - [ES]$  is introduced, and the resulting nonlinear equation equation 3.8 is solved numerically for the steady-state enzyme concentration  $[ES]_{qss}$  using `nsolve` from the Python package `sympy`. The numerical solution is obtained using the reference concentration  $[ES]_0$  as an initial guess for the nonlinear solver. The reaction rate of the enzymatic reaction at steady state, for a set of constant  $[S]$  and  $[P]$ , is then given by the net reaction rate of product formation at steady state:

$$v_{net,qss} = [ES]_{qss} k_{2,f,eff}([ES]_{qss}, P, S) - ([E_T] - [ES]_{qss}) [P] k_{2,b,eff}([ES]_{qss}, P, S) \quad (3.9)$$

### Chapter 3. Particle-based modeling of crowding effects on enzyme kinetics

---

where  $[ES]_{qss}$  is the enzyme-complex concentration at the quasi-steady state. The average apparent Michaelis-Menten parameters are then extracted using a linear approximation of  $v([X])$  with  $v([X])/[X]$  for either  $[S] = 0$  or  $[P] = 0$ , i.e., the Eadie-Hofstee form of Michaelis-Menten kinetics (Eadie, 1942; Hofstee, 1959). The slope of these linear regressions yields the respective  $K_M$ , and the  $y$ -axis intercept yields the respective  $V_{max}$ :

$$|v([S])| = -K_{M,S} \frac{|v([S])|}{|S|} + V_{max}^+ \quad (3.10)$$

$$|v([P])| = -K_{M,P} \frac{|v([P])|}{|P|} + V_{max}^- \quad (3.11)$$

To express the thermodynamic driving forces, the elementary rate model was considered as  $M$  reversible reactions  $\rho \in [1, 2]$ , with the forward flux  $v_{\rho,f}$  and the backward flux  $v_{\rho,b}$ . Using the principle of detailed balance, the free energy of the reaction can be expressed as a function of the displacement from equilibrium  $\Gamma = v_b/v_f$  (Demirel, 2013):

$$\Delta_r G'_\rho = RT \ln \Gamma_\rho = RT \ln \left( \frac{v_{\rho,b}}{v_{\rho,f}} \right) \quad (3.12)$$

where  $R$  is the general gas constant and  $T$  is the absolute temperature. With the fluxes expressed in terms of the generalized elementary rate law the free energy reads

$$\Delta_r G'_\rho = RT \ln \left( \frac{k_{\rho,b,0} e^{\beta_{\rho,b}} \prod_{i=1}^M \left( \frac{[X_i]}{[X_i]_0} \right)^{n_{i,\rho,b} + \alpha_{i,\rho,b}} [X_i]_0^{n_{i,\rho,b}}}{k_{\rho,f,0} e^{\beta_{\rho,f}} \prod_{i=1}^M \left( \frac{[X_i]}{[X_i]_0} \right)^{n_{i,\rho,f} + \alpha_{i,\rho,f}} [X_i]_0^{n_{i,\rho,f}}} \right) \quad (3.13)$$

In general, the overall free energy consists of ideal and nonideal contributions. The ideal contribution consists of the standard free energy of the reaction and the concentration contributions, and the nonideal contribution contains terms emerging from molecular interactions, such as by steric repulsion, van der Waals forces, electrostatic interactions, or nonspecific attractions.

$$\Delta_r G'_\rho = \Delta_r G'_\rho{}^o + \sum_{i=1}^M n_{i,\rho} RT \ln([X_i]) + \Delta_r G'_{\rho,steric} + \Delta_r G'_{\rho,VDW} + \Delta_r G'_{\rho,el} + \dots \quad (3.14)$$

In this work, only the nonideal contributions due to steric repulsion were modeled by means of a hard-sphere potential, though in the most general case, the formulation presented in this work allows for the inclusion of any kind of nonideal contribution. The presented approach shows that a power-law approximation suffices to describe the effect of steric repulsion. The approximation of the effect of nonspecific attractions and other interactions in terms of kinetic parameters and free energies will probably require alternative functional forms in



these approximations in addition to this power-law formulation. A functional to account for the approximation of nonspecific attractions could be based on the derivations of Kim and Mittal (Kim and Mittal, 2013).

By comparing the free energy of the generalized elementary rate model to the free energy of the dilute mass-action equivalent, the ideal contribution can be identified as

$$\Delta_r G'_{\rho,ideal} = RT \ln \left( \frac{k_{\rho,b,0}}{k_{\rho,f,0}} \right) + \sum_{i=1}^M n_{i,\rho,b} RT \ln([X_i]) - \sum_{i=1}^M n_{i,\rho,f} RT \ln([X_i]) \quad (3.15)$$

$$= \Delta_r G'_{\rho} + \sum_{i=1}^M n_{i,\rho} RT \ln([X_i]) \quad (3.16)$$

The remaining contributions can be identified as the nonideal contribution:

$$\Delta_r G'_{\rho,non-ideal} = RT(\beta_{\rho,b} - \beta_{\rho,f}) + RT \ln \left( \frac{\prod_{i=1}^M \left( \frac{[X_i]}{[X_i]_0} \right)^{\alpha_{i,\rho,b}}}{\prod_{i=1}^M \left( \frac{[X_i]}{[X_i]_0} \right)^{\alpha_{i,\rho,f}}} \right) \quad (3.17)$$

$\Delta_r G'_{\rho,non-ideal}$  can be further partitioned into a reactant-independent and a reactant-dependent contribution:

$$\Delta_r G'_{\rho,non-ideal} = \Delta_r G'_{\rho,indep} + \Delta_r G'_{\rho,dep} \quad (3.18)$$

$$= RT(\beta_{\rho,b} - \beta_{\rho,f}) + RT \ln \left( \prod_{i=1}^M \left( \frac{[X_i]}{[X_i]_0} \right)^{\alpha_{i,\rho,b} - \alpha_{i,\rho,f}} \right) \quad (3.19)$$

The free energy of the generalized elementary Michaelis-Menten kinetics is given by the sum of all reversible-reaction free-energy contributions  $\Delta_r G'_{\rho}$ :

$$\Delta_r G' = \sum_{\rho}^R \Delta_r G'_{\rho} \quad (3.20)$$

With  $[X_i] = [[S], [E], [ES], [P]]$ , the free energy of the reaction can be simplified to the well-known ideal contribution containing only the chemically modified species  $[S]$  and  $[P]$  as well as a non-ideal contribution, wherein the non-ideal contribution is a phenomenological description of free-energy change based on the GEEK.

$$\Delta_r G' = \Delta_r G'^o + RT \ln \left( \frac{[P]}{[S]} \right) + \Delta_r G'_{non-ideal}([S], [E], [ES], [P]) \quad (3.21)$$

The formulation of the reversible Michaelis-Menten rate law in terms of GEEK allows for the phenomenological capture of nonlinear effects on the collision level.

### 3.2.3 A hard sphere model for macromolecular crowding

To incorporate the spatial effects into the enzymatic reaction system, hard-sphere Brownian reaction dynamics (HSBRD) were used. This method is using the elastic hard-sphere Brownian dynamics algorithm (Strating, 1999) to compute the transport and the collisions dynamics of the particles and implement reactions according to the Brownian dynamics algorithm (Allen, 1980; Northrup et al., 1984). Similar methods combining these two approaches have been presented Wilson et al. (2018) and Kim et al. (2014).

The method describes the movement of independent particles as a random walk of point particles diffusing in a viscous medium. Thereby, HSBRD neglects the hydrodynamic interactions between the particles. The equations of motion are given in terms of the overdamped Langevin equation. Using the Einstein-Smoluchowski relation, its velocity is given by Wang and Uhlenbeck (1945):

$$\frac{d\mathbf{x}}{dt} = -\frac{D}{k_B T} \mathbf{F}(\mathbf{x}) + \sqrt{2D} \frac{d\eta}{dt} \quad (3.22)$$

where  $\mathbf{F}(\mathbf{x})$  is a force acting on the particle,  $k_B$  is the Boltzmann constant,  $T$  is the absolute temperature of the surrounding fluid, and  $\eta(t)$  is the result of a three-dimensional Wiener process. An explicit Euler formulation was used to update the positions at every time step,  $\Delta t$ , as follows:

$$\mathbf{x}_{t+\Delta t} = \mathbf{x} + \Delta t \frac{D}{k_B T} \mathbf{F}(\mathbf{x}) + \sqrt{2D\Delta t} \boldsymbol{\eta}_t \quad (3.23)$$

where  $\boldsymbol{\eta}_t$  is a random vector drawn from a normal distribution.

Reaction-diffusion dynamics methods account for bimolecular and unimolecular reactions by a Monte Carlo simulation of the local reaction dynamics. For bimolecular reactions, the Monte Carlo simulation was performed when two reactants collided, i.e., their radii overlapped after the positions were updated. Then a uniform distributed random number  $r$  was compared to the reaction with a probability  $p$  to determine if the reaction occurred within this time step  $\Delta t$ . The probability  $p$  is given by the microscopic reaction rate  $k_{j,micro}$  (Morelli and ten Wolde, 2008):

$$p = 1 - e^{-\frac{k_{j,micro}\Delta t}{4\pi I(D,R,\Delta t)}} \quad (3.24)$$

where  $I(D,R,\Delta t)$  is a normalization factor for the effective collision volume in Brownian

reaction dynamics simulations to account for all possible diffusion path within  $\Delta t$ , as derived by Morelli and ten Wolde (Morelli and ten Wolde, 2008). Using the relation derived by Collins and Kimball, the observed steady-state reaction rate  $k_{j,0}$  for a bimolecular reaction,  $j \in [(1, f), (2, b)]$  with educts A and B, in homogenous, dilute conditions is related to its microscopic or transition rate constant  $k_{j,micro}$  and the diffusion-limited reaction rate constant  $\gamma_j = 4\pi(D_A + D_B)(r_A + r_B)$  (Collins and Kimball, 1949b). Assuming that the Collins-Kimball rate constant corresponds to the observed rate constant in the experimental *in vitro* system and the dilute particle simulation, the corresponding microscopic rate constant can be expressed as a function of the rate constant observed *in vitro*  $k_{j,0}$  and the diffusion-limited rate constant  $\gamma_j$ , calculated based on the molecular properties of the collision radii  $r_A, r_B$  and self-diffusion constants  $D_A, D_B$ :

$$k_{j,micro} = \frac{\gamma_j k_{j,0}}{\gamma_j - k_{j,0}} \quad (3.25)$$

In the case of a particle collision without a subsequent reaction, an elastic hard-sphere collision was assumed to take place. The new particle position was computed from the momentum conservation using the average velocity  $\mathbf{v}_i = \Delta \mathbf{r} / \Delta t$  of the move that led to the particle overlap (Strating, 1999).

First-order reactions,  $j \in [(1, b), (2, f)]$ , are modeled similarly to bimolecular reactions by comparing a uniformly distributed random variable to the probability that the reaction took place in the time interval  $\Delta t$ , with the reaction probability of  $p = 1 - \exp(-k_{j,micro} \Delta t)$ . The reaction products are placed in contact around the original position of the educt using a random orientation. If the products were to collide with any other particles, the move would be rejected, and the educt would remain at its original position. Otherwise, the educt would be removed, and the products would be placed instead.

Furthermore, constant particle boundary conditions were applied at every time step through the random insertion or removal of particles of a given species to match the specified particle count of the species. The HSBRD particle simulation was implemented in C++ using the OPENFPM framework (Incardona et al., 2019).

### 3.2.4 Measuring effective reaction rate constants

Because it is necessary to resolve the particle movement on the nanosecond timescale as opposed to the timescales of the reaction dynamics, which are found to be in the order of

seconds to hours, a separated timescale approach was proposed to efficiently bridge these differences. The effective elementary reaction rates at constant concentrations and crowding conditions in particle simulation were therefore measured. To measure the effective rate constants from a particle simulation, two separate schemes for monomolecular and bimolecular rate constants were used.

For monomolecular rate constants,  $j \in [(1, b), (2, f)]$ , the effective reaction rates were extracted by probing the space around the enzyme-substrate complexes. Therefore, for every valid educt molecule  $k$  of a monomolecular reaction  $j$ ,  $L$  dissociation reactions were attempted with a random orientation. For each molecule  $k$  and reaction  $j$ , the success of the  $l$ -th attempt  $\omega_{jkl}$  is determined. If the dissociation were to be successful, meaning that the dissociated particles would not collide,  $\omega_{jkl} = 1$ . If the dissociation were to yield a collision,  $\omega_{jkl} = 0$ . Averaging over the results of all dissociation attempts  $\omega_{jkl}$  of the probed molecule  $k$ , a local success probability of was obtained. To describe the equivalent homogenous system, the reaction success probability was computed as the mean of the local average success rate over all  $N$  probed particles. In the limit of continuous concentrations, the effective rate constant,  $k_{j,eff}$ , is given by the rate constant  $k_{j,0}$  scaled by the reaction success probability  $\omega_j$ :

$$k_{j,eff} = k_{j,0} \langle \omega_j \rangle \quad (3.26)$$

The effective bimolecular rate constants,  $j \in [(1, f), (2, b)]$ , can be extracted from the effective collision frequency  $z_{A,B}$  between the two educts  $A$  and  $B$  of reaction  $j$ . This collision frequency is estimated as the number of collisions between  $A$  and  $B$  in an integration time interval  $c_{A,B}(t, t + \Delta t)$  per time step  $\Delta t$ , as described in Appendix A.1.

$$k_{j,eff} = \frac{\langle z_{A,B} \rangle}{N_A N_B} \left( 1 - e^{-\frac{k_{j,micro} \Delta t}{4\pi I(D,R,\Delta t)}} \right) \quad (3.27)$$

#### 3.2.5 Modeling framework

In this work, we propose a new, to our knowledge, simulation framework using the above-described concept of GEEK. In our simulation framework, an equivalent particle model is first created from an elementary step mechanism (Figure 3.1, part 1). To create an equivalent particle model, only the elementary reactions of the enzyme mechanism are required. If only phenomenological constants, e.g., parameters for the quasi-steady-state approximation, are given for the enzymatic reaction, it is necessary to map these to the elementary reaction rate constants. Furthermore, all species involved in the elementary reaction properties need to

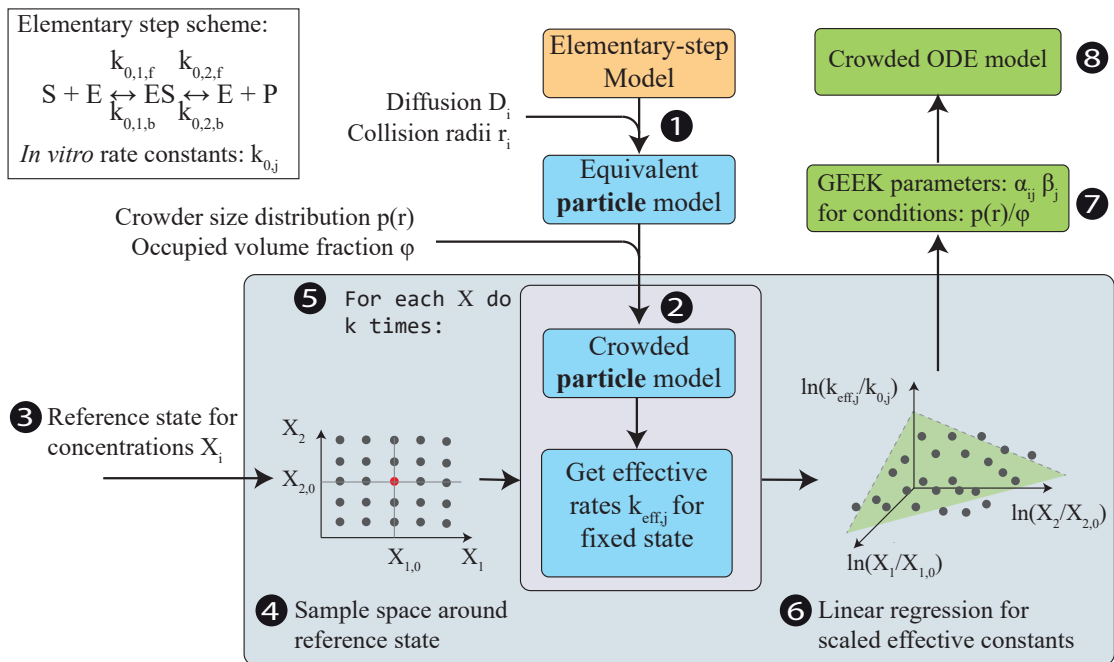


Figure 3.1 – Modeling framework for crowded generalized elementary kinetics (GEEK). The input for the modeling framework is an arbitrary elementary step model containing *in vitro* data for the enzyme kinetics. 1) This model is then translated into an equivalent *in vitro* particle model of the enzymatic reaction. 2) The space is filled with inert molecules that are drawn from a size distribution  $p(r)$  until the fraction  $\phi$  of the simulation space is occupied. 3) A reference concentration state is then chosen for the GEEK model, and 4) the space around the concentration space is sampled. 5) The  $k$  particle model realizations are then simulated for each concentration sample, i.e., repeat step 2 and simulate. 6) From the resulting particle traces, the effective rate constants are measured from the particle collision frequencies and the locally available volume. 7) These effective reaction rate constants are log transformed, and a linear regression is performed with respect to the scaled logarithmic concentrations. The output of the linear regression directly links to the GEEK parameters; see Eqs. 7 and 8. 8) Finally, the GEEK model can approximate the crowded kinetics using ODEs.

be assigned to describe their molecular movement, i.e., a diffusion coefficient, a collision radius, and a mass. Given the molecular data, the rate constants of the particle model are matched with the rate constants of the elementary step model with the assumption that the measured or calculated rate constants were measured in homogenous, dilute conditions. In the case of monomolecular reactions, the observed rate constants are then equivalent to the microscopic transition rates. For bimolecular reactions,  $j \in [(1, b), (2, f)]$ , the diffusion-limited rate constant  $\gamma_j$  is first computed based on the diffusion coefficients and collision radii and then matched to the effective reaction rate of the dilute, homogenous particle system with the rate constant in the elementary step model by adapting the corresponding microscopic rate constant  $k_{j,micro}$  using equation (3.25). A volume that is large enough to capture the local bulk properties of a locally well-mixed enzyme-substrate system is then chosen such that the number of particles of each species in the system is large enough to discretize the concentration space of interest.

In the second step, the system is perturbed on the microscopic level to investigate the influence of crowding (Fig. 2, part 2). Therefore, inert particles are introduced into the system that therefore alter effective particle interactions between the reactive species (Berezhkovskii and Szabo, 2016). To model a realistic crowding environment, a size distribution function  $p(r)$  is estimated from the mass distribution  $p(M_w)$  and an empirical mass size relation  $r = 0.0515M_w^{0.392}$  [nm], with  $M_w$  in [Da], as reported for proteins in *E. coli* by Kalwarczyk et al. (2012). The simulation volume is then populated with inert molecules by randomly drawing collision radii from the size distribution until the specified inert volume fraction  $\phi$  is reached. The diffusion constant of the individual species is then calculated using the Stokes-Einstein relation, assuming that the hydrodynamic radius is equal to the collision radius Einstein (1905):

$$D = \frac{k_B T}{6\pi\eta r_{hyd}} \quad (3.28)$$

where  $r_{hyd}$  is the hydrodynamic radius and  $\eta$  is the dynamic viscosity of the solvent, here assumed to be water.

Next, the model is sampled around a chosen reference state (Figure 3.1, parts 3 and 4). In this work, we chose to generate our sample with a full-factorial design. For each concentration sample, a particle simulation is performed where the effective rate constants  $k_{eff,j}$  are measured for every elementary reaction as described in the previous section (Figure 3.1, part 5).

Subsequently, multivariate linear regression is used to estimate the mean GEEK parameters  $\alpha_{ij}$  and  $\beta_j$  for the specified crowding conditions (Figure 3.1, part 6). Finally, the GEEK, as

### 3.3. Effects of crowding on the reversible Michaelis Menten kinetics

---

described above, is used to analyze the response behavior of an equivalent crowded ODE-enzyme model (Figure 3.1, part 7).

#### 3.2.6 Weighted linear regressions

To estimate the GEEK parameters using multivariate regression, a multivariate regression was performed. Because the variance of the reaction rate would be expected to be dependent on the regression variables, a weighted linear regression was performed to avoid fitting data with large heteroscedasticity. The conditional variance of the residuals was therefore extracted, and a weighted linear regression was performed in which each observation was weighted by the inverse of the conditional variance of the residual (Details described in Appendix A.3). To perform these calculations, the Python package *statsmodels* was used (Seabold and Perktold, 2010).

#### 3.2.7 Computational details

The Brownian reaction dynamics simulations were performed with a time step  $\Delta t$  of 0.25 ns. The dynamics viscosity of the liquid between the particles was assumed to be water with 0.7 Pas at  $T = 310.15$  K. The system is considered to be isothermal ( $T = \text{constant}$ ). At each time step, all possible first-order reactions are attempted  $L = 100$  times. For the regression input space, all combinations of substrate and product concentrations that were  $n$ -fold increased and decreased with respect to the reference concentration of  $[S]_0 = [P]_0 = 49 \mu\text{M}$  were used, with  $n \in [1, 2, 3, 4, 5]$ , in combination with all free-enzyme and enzyme-complex concentrations that yielded saturations of  $\sigma = [ES]/[ET] = [0.1, 0.2, 0.3, 0.4, 0.5, 0.6, 0.7, 0.8, 0.9]$  given a total amount of enzyme  $[E_{tot}] = [ES] + [E] = 64 \mu\text{M}$ . Each sampled concentration state is simulated  $1 \mu\text{s}$ , where the first  $0.1 \mu\text{s}$  are discarded. Furthermore, 10 independent realizations of the crowding population were used for every concentration sample to capture the variability that comes from differently sized crowding agents drawn from the size distribution.

### 3.3 Effects of crowding on the reversible Michaelis Menten kinetics

To address the pitfalls currently associated with computational studies of enzymatic reactions in the intracellular space, this work presents GEEK, a novel, to our knowledge, approach to capture spatial effects, such as crowding, in ODE models. The framework is available in the form of two Python packages: a package to implement GEEK expressions into ODE (<https://github.com/EPFL-LCSB/geek>) and a package to perform openfpm-based HSRD

simulations (<https://github.com/EPFL-LCSB/openbread>). The GEEK formulation directly quantifies the deviation from dilute mass-action behavior in a systematic and efficient procedure, and we have focused our studies on the impact of crowding due to the influence of densely packed biomolecules on enzyme reaction rates *in vivo*.

### 3.3.1 Validation of GEEK

We validate the GEEK framework by comparing the an HSBRD-based GEEK model with the exact solutions obtained by HSBRD. We therefore used the initial rate experiment of a simple association-dissociation system. We simulated this system in dilute conditions and with single-sized inert molecules,  $r = 2.1$  nm, for volume fractions between  $\phi = 0.0$  and  $\phi = 0.4$ . We show that for this reaction system, the GEEK models are able to capture the dynamics and the impact of crowding on the dynamics as predicted by the respective full simulation of the system (see figures A.4 to A.7). To perform these comparisons, we used a simple association-dissociation  $A + B \rightleftharpoons C$  model with two different parameter sets.

We validate the GEEK framework by comparing i) an HSBRD-based GEEK model with the exact solutions obtained by HSBRD and ii) a GEEK model based on the crowder-free Cichocki-Hinsen algorithm with the respective solution of the full simulation (see details described in Appendix A.3). We therefore used the initial rate experiment of a simple association-dissociation system. We simulated this system in dilute conditions and with single-sized inert molecules,  $r = 2.1$  nm, for volume fractions between  $\phi = 0.0$  and  $\phi = 0.4$ . We show that for this reaction system, the GEEK models are able to capture the dynamics and the impact of crowding on the dynamics as predicted by the respective full simulation of the system. We further discuss the results of i and ii with respect to their modeling assumptions in appendix A.3.

We then applied the described modeling framework to investigate the effects of macromolecular crowding on the enzymatic activity of PGM in *E. coli*. PGM is part of the lower glycolysis pathway and functions by reversibly transforming 3-phospho-D-glycerate (g3p) into 2-phospho-D-glycerate (g2p). We use PGM for our investigation because it exhibits a prototypical reversible Michaelis-Menten kinetics and its *in vitro* kinetics are well-known (Fraser et al., 1999).



### 3.3. Effects of crowding on the reversible Michaelis Menten kinetics

Table 3.1 – *In vitro* Michaelis-Menten parameters and calculated elementary rate constants for PGM in *E. coli*, as found by Fraser et al. (1999)

Michaelis-Menten parameters		Elementary rate constants	
$K_{M,g3p}$	210 $\mu\text{M}$	$k_{1,f}$	$1.52 \times 10^5 \text{ s}^{-1} \text{ M}^{-1}$
$K_{M,g2p}$	97 $\mu\text{M}$	$k_{1,b}$	$22 \times 10^5 \text{ s}^{-1}$
$k_{cat} \text{ g3p to g2p}$	22 $\text{s}^{-1}$	$k_{2,f}$	$11 \times 10^5 \text{ s}^{-1}$
$k_{cat} \text{ g2p to g3p}$	11 $\text{s}^{-1}$	$k_{2,b}$	$3.29 \times 10^5 \text{ s}^{-1} \text{ M}^{-1}$

#### 3.3.2 Impact of crowding on the elementary reaction level

We then applied the described modeling framework to investigate the effects of macromolecular crowding on the enzymatic activity of PGM in *E. coli*. PGM is part of the lower glycolysis pathway and functions by reversibly transforming 3-phospho-D-glycerate (g3p) into 2-phospho-D-glycerate (g2p). We use PGM for our investigation because it exhibits a prototypical reversible Michaelis-Menten kinetics and its *in vitro* kinetics are well-known (Fraser et al., 1999).

For our reference elementary step mass-action model, which will serve as a basis for constructing the GEEK model, we calculated the elementary rate constants by the relations given in equations 3.3a, 3.3b, 3.4a and 3.4b from the *in vitro* Michaelis-Menten parameters measured by Fraser et al. (1999) (Table 3.1). Based on this *in vitro* elementary step model, we built an equivalent *in vitro* particle model that required additional information on the molecular parameters, including mass, diffusion, and collision radius, of all the species involved in a reaction, meaning the substrates, products, free enzymes, and enzyme complexes. To estimate the collision radius of the enzyme and the enzyme-substrate complex, we followed the suggestions of Gameiro et al. (2016) and used the empirical relation between mass and size to estimate the inert molecule size from the enzyme mass (Kalwarczyk et al., 2012; Gameiro et al., 2016). In the same way, we applied the Stokes-Einstein relation to calculate the diffusion constants from the collision radius. We additionally assumed that the enzyme-substrate complex entirely enclosed the substrate with its binding pocket, thus rendering the collision radius of the complex and enzyme equal. To estimate the collision radius of g3p and g2p, we also followed the suggestions of Gameiro et al. and used the method developed by Zhao et al. to estimate their van der Waals volume and to calculate the equivalent sphere radius (Gameiro et al., 2016; Zhao et al., 2003). The diffusion constants of g2p and g3p were obtained from the literature (56). All molecular properties are summarized in Table 3.2.

Given the effective elementary rate constants and the molecular properties of the species, we calculated the effective microscopic rate constants using the relation given in equation 3.25 (Ta-

### Chapter 3. Particle-based modeling of crowding effects on enzyme kinetics

Table 3.2 – Molecular Properties of the Reacting Particles, data obtained from: a) Perry (1973), calculated according to the approximations suggested by b) Gameiro et al. (2016) as well as obtained from c) Gameiro et al. (2016)

Species	Diffusion ( $\mu^2 \text{s}^{-1}$ )	Collision Radius (nm)	Mass (kDa)
g3p	940 a	1.11 b	0.186 b
g2p	940 a	1.11 b	0.186 b
PGM	84.8 b	3.87 b	61 c
PGM complex	84.8 b	3.87 b	61.186

Table 3.3 – Microscopic reaction rates per reacting particle (p), or per collision (c), and diffusion-limited rate constants of the bimolecular reactions.

$$\begin{aligned}
 k_{1,f} & 1.57 \times 10^5 \text{s}^{-1} \text{M}^{-1} \\
 k_{1,b} & 10 \text{s}^{-1} \\
 k_{2,f} & 22 \text{s}^{-1} \\
 k_{2,b} & 3.40 \times 10^5 \text{s}^{-1} \text{M}^{-1}
 \end{aligned}$$

ble 3.3). Comparing the microscopic rate constants in table 3.3 with the diffusion-limited rate constants, it can be seen that the diffusion-limited constants  $\gamma_{1,f} = \gamma_{2,b} = 3.88 \times 10^{10} \text{M}^{-1} \text{s}^{-1}$  are about five orders of magnitude higher than the microscopic reaction constants. This indicates that the microscopic binding process is much slower than the diffusion process and that the kinetics are reaction limited and not diffusion limited. Thus, the mean time until the first collision between two reactants, i.e., the mean first passage time, is orders of magnitudes shorter than the mean time to the first reaction. For a reaction to be successful, tens of thousands of collisions are occurring; hence, the impact of any increase in high-frequency first passage events due to fractal diffusion is limited (Benichou et al., 2010).

To build a GEEK model that allows us to characterize the enzyme kinetics in a crowded environment, we sampled the concentration space. This was done using a full-factorial design, allowing us to study the effect of several variables on the response output, as well as interactions between those variables, that sampled both the product and substrate concentrations as well as different enzyme saturation levels, indicating the percentage of bound enzyme with respect to the total enzyme concentration. The computational details of the simulation procedure are summarized in the respective method subsection above.

In total, we generated 21 generalized elementary kinetic models for five different inert volume fractions  $\phi_k$  and four different size distributions  $p_k(r)$ , plus one without any crowding. This allowed for a detailed comparison of the effects of the volume fraction and size distribution of the crowding agents on enzyme kinetics. For the size distributions, we used 1) the E. coli distribution derived from Kalwarczyk et al. (2012), 2) a population containing only particles

### 3.3. Effects of crowding on the reversible Michaelis Menten kinetics

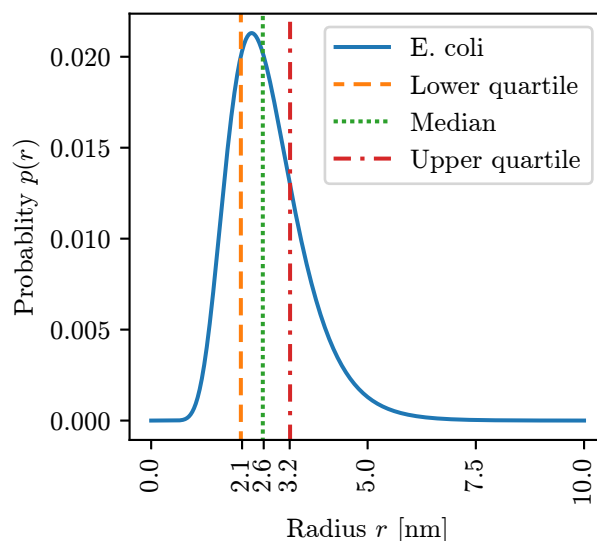


Figure 3.2 – Size distribution function of the inert particles, numerically calculated from the mass distribution and empirical mass size relation as reported for proteins in *E. coli* by Kalwarczyk et al. (2012).

of the median size of the *E. coli* distribution, 3) a population the size of the upper quartile of the *E. coli* size distribution, and 4) a population the size of the lower quartile (Figure 3.2; (Kalwarczyk et al., 2012)). These crowding populations were each investigated for inert volume fractions of  $\phi \in [0.0, 0.1, 0.2, 0.3, 0.4, 0.5]$ .

For each crowding condition, we estimated the mean GEEK parameters  $\alpha_{ij}$  and  $\beta_j$  using multivariate weighted linear regression, which indicate conditions that likely influenced the enzyme kinetics. To further quantify the uncertainty of the mean GEEK parameters, the 95% confidence intervals of the regression results are given in Table 4. For parameter estimates with a p-value  $\leq 0.05$ , it was assumed that no significant correlation existed, and these parameters were not accounted for in the GEEK model. A closer analysis shows that the offset  $\beta_j$  could always be determined with statistical significance; only some of the coupling parameters  $\alpha_{ij}$  were not able to be determined with the required significance level. Note that this mean GEEK parameter model assumes that the crowding composition of an average cell is given by the average effect of a crowding configuration on the rate constant, which should accurately reflect the mean behavior of cell populations. Further, it should be taken into account that the calculations leading to the effective rate constants are based on the assumption of the microscopic model, considering that effective association rate constants are proportional to the collision frequency of their educts and that effective dissociation reaction constants are proportional to the surface accessible to the products. The validity of the GEEK approximation

### Chapter 3. Particle-based modeling of crowding effects on enzyme kinetics

Table 3.4 – Parameters of the generalized elementary kinetics, i.e.  $\alpha_{ij}$  and  $\beta_j$ , for all elementary reactions at different inert volume fractions, where \* denotes GEEK parameters with a significance of  $p \leq 0.05$ .

Parameters	0%	10%	20%	30%	40%	50%
$\beta_{1,f}$	$7.31 \times 10^{-2}$	$2.61 \times 10^{-1}$	$4.57 \times 10^{-1}$	$6.87 \times 10^{-1}$	$9.57 \times 10^{-1}$	1.25
$\alpha_{S,1,f}$	$4.74 \times 10^{-3}$	*	$3.22 \times 10^{-3}$	$7.22 \times 10^{-3}$	$6.95 \times 10^{-3}$	$3.23 \times 10^{-3}$
$\alpha_{E,1,f}$	$1.07 \times 10^{-2}$	$1.89 \times 10^{-2}$	$9.67 \times 10^{-3}$	$8.07 \times 10^{-3}$	$1.23 \times 10^{-2}$	*
$\alpha_{ES,1,f}$	*	$1.34 \times 10^{-2}$	*	*	*	*
$\alpha_{P,1,f}$	*	$2.51 \times 10^{-3}$	$-3.47 \times 10^{-3}$	*	*	$2.42 \times 10^{-3}$
$\beta_{1,b}$	$-1.48 \times 10^{-2}$	$-1.17 \times 10^{-1}$	$-2.80 \times 10^{-1}$	$-5.46 \times 10^{-1}$	-1.03	-2.265
$\alpha_{S,1,b}$	$-2.94 \times 10^{-3}$	$-3.56 \times 10^{-3}$	$-4.53 \times 10^{-3}$	$-6.09 \times 10^{-3}$	$-8.33 \times 10^{-3}$	$-9.58 \times 10^{-3}$
$\alpha_{E,1,b}$	$-1.90 \times 10^{-4}$	$1.71 \times 10^{-3}$	$6.47 \times 10^{-4}$	$3.32 \times 10^{-3}$	*	$3.16 \times 10^{-3}$
$\alpha_{ES,1,b}$	*	$3.46 \times 10^{-3}$	*	$2.03 \times 10^{-3}$	$-1.22 \times 10^{-3}$	*
$\alpha_{P,1,b}$	$-2.94 \times 10^{-3}$	$-3.58 \times 10^{-3}$	$-4.52 \times 10^{-3}$	$-6.09 \times 10^{-3}$	$-8.33 \times 10^{-3}$	$-9.58 \times 10^{-3}$
$\beta_{2,f}$	$-1.48 \times 10^{-2}$	$-1.17 \times 10^{-1}$	$-2.80 \times 10^{-1}$	$-5.46 \times 10^{-1}$	-1.03	-2.26
$\alpha_{S,2,f}$	$-2.94 \times 10^{-3}$	$-3.56 \times 10^{-3}$	$-4.53 \times 10^{-3}$	$-6.09 \times 10^{-3}$	$-8.34 \times 10^{-3}$	$-9.58 \times 10^{-3}$
$\alpha_{E,2,f}$	$-1.90 \times 10^{-4}$	$1.71 \times 10^{-3}$	$6.53 \times 10^{-4}$	$3.31 \times 10^{-3}$	*	$3.13 \times 10^{-3}$
$\alpha_{ES,2,f}$	*	$3.46 \times 10^{-3}$	*	$2.01 \times 10^{-3}$	$1.20 \times 10^{-3}$	*
$\alpha_{P,2,f}$	$-2.94 \times 10^{-3}$	$-3.58 \times 10^{-3}$	$-4.52 \times 10^{-3}$	$-6.10 \times 10^{-3}$	$-8.34 \times 10^{-3}$	$-9.57 \times 10^{-3}$
$\beta_{2,b}$	$6.88 \times 10^{-2}$	$2.54 \times 10^{-1}$	$4.58 \times 10^{-1}$	$6.85 \times 10^{-1}$	$9.52 \times 10^{-1}$	1.25
$\alpha_{S,2,b}$	*	*	$2.29 \times 10^{-3}$	*	$3.09 \times 10^{-3}$	*
$\alpha_{E,2,b}$	*	*	$1.05 \times 10^{-2}$	*	*	*
$\alpha_{ES,2,b}$	*	*	*	$-7.78 \times 10^{-3}$	*	*
$\alpha_{P,2,b}$	$6.59 \times 10^{-3}$	$2.76 \times 10^{-3}$	$4.70 \times 10^{-3}$	$6.85 \times 10^{-3}$	$8.45 \times 10^{-3}$	$3.74 \times 10^{-3}$

is therefore always dependent on the validity of the underlying microscopic model used to compute the effective rate constants. As mentioned in the introduction, the workflow within the GEEK framework will remain valid even if a more detailed microscopic model is used for the estimation of the rate constant.

Comparing the parameters  $\alpha_{ij}$  and  $\beta_j$  of each elementary reaction  $j$  (Table 3.4), it can generally be observed that the direct effect  $\beta_j$  is about one to two orders of magnitude larger than each corresponding coupling coefficient,  $\alpha_{ij}$ . Therefore, the direct effect is on the order of  $\pm 10^{-2}$  to  $\pm 100$ , whereas the coupling coefficients are on the order of  $\pm 10^{-4}$  to  $\pm 10^{-2}$ . Assuming a twofold increase in a concentration, the change in the coupling is smaller than 1%, whereas the direct effect varies between one and 1000%. This suggests that the effect of the reduced dimensionality only plays a small role compared to the effective interaction potential and the diffusion inhibition.

#### 3.3.3 Effect on the Michaelis Menten parameters

We used the results of the linear regression to parameterize GEEK models to compare the ODE simulations of the classical Michaelis-Menten experiment with the mass-action model. The

### 3.3. Effects of crowding on the reversible Michaelis Menten kinetics

basis of this experiment involved an initial substrate concentration  $[S]_{init}$  that was added to a volume with a fixed enzyme concentration  $[E]_{init} = [E]_{tot}$ . When the substrate was added, the enzyme started to convert the substrate into a product. If the enzyme was operating reversibly, part of the product would also be converted back to a substrate, and the reaction would become indistinguishable as it approached equilibrium. In this equilibrium state, the overall free energy of the reaction was close to zero. Therefore, the ratio between the product and substrate concentrations could be used to estimate the apparent equilibrium constant  $K_{eq}$ .

To characterize the dynamics of this system, the time to half-equilibrium  $t_{eq}/2$  was measured, which indicates the time needed for the ratio between the product and substrate concentrations to equal  $K_{eq}/2$  (Figure 3.3 a). In general, an increase in the  $t_{eq}/2$  was seen with an increasing substrate concentration (Figure 3.3 a). The time to half-equilibrium for the interconversion between g3p to g2p was reduced for small substrate concentrations and inert molecule fractions, up to  $\phi = 30\text{--}40\%$ . In the case of  $[S]_{init} = [S]_{ref}/4$ , the time to half-equilibrium was reduced to a minimal value for an inert volume fraction of  $\phi = 40\%$  (Figure 3.3 a). For  $[S]_{init} = [S]_{ref}$  and  $[S]_{init} = 2[S]_{ref}$ , this decrease in half-life time persists, though the overall half-life times are larger than for  $[S]_{init} = [S]_{ref}/4$ , and the minimal point occurs at lower inert volume fractions. Finally, in the  $[S]_{init} = 4[S]_{ref}$  case, this decrease in  $t_{eq}/2$  is no longer visible. It follows from this that the average initial rate increases with substrate concentration and decreases with an increasing volume occupancy. This suggests that the same substrate concentrations yield higher enzyme saturations, meaning that the ratio of enzyme-substrate complex/total amount of enzyme increases and that the dissociation of the enzyme-substrate complex is inhibited.

For a closer analysis of these findings, the Michaelis-Menten parameters were estimated using Eadie-Hofstee diagrams, solving for the steady-state flux of the substrate and product concentrations between 4.9 and 490  $\mu\text{M}$  (Equation 3.8). The Eadie-Hofstee diagrams reveal that for both high- and low-occupancy volume fractions, a slight nonlinearity with respect to the linear Eadie-Hofstee form of the reversible Michaelis-Menten is introduced with the GEEK. This indicates that the effective maximal flux  $V_{max}^{+/-}$  and effective Michaelis-Menten constant  $K_{M,X,eff}$  are actually functions of the reactant concentrations  $[S]$  and  $[P]$ . For the case of  $\phi = 0\%$ , this nonlinearity is only pronounced at small reactant concentrations, whereas for higher volume occupancy conditions, the nonlinearity is visible over the entire measurement range. Nevertheless, we used linear regression to estimate the effective average parameters to compare the steady-state GEEK model to the traditional Michaelis-Menten kinetics.

Interestingly, the steady-state analysis revealed that all the effective Michaelis-Menten pa-

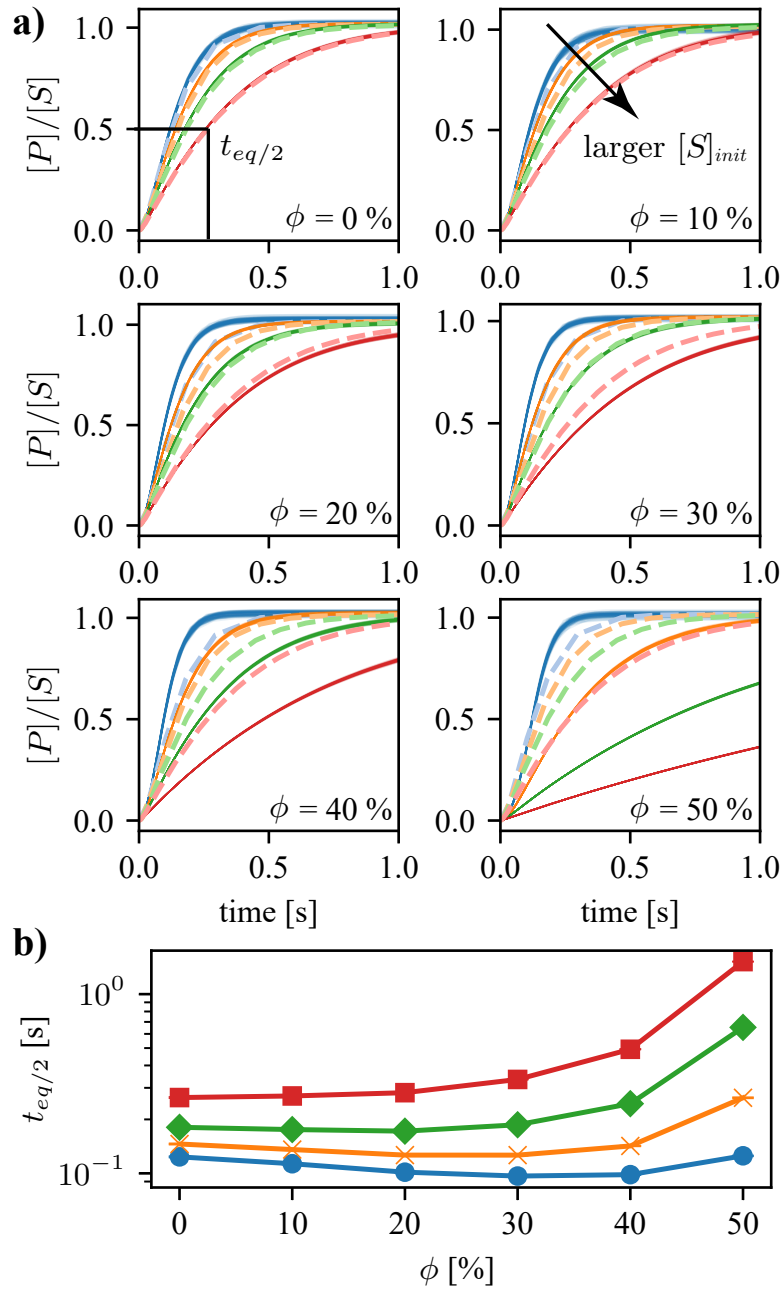


Figure 3.3 – (a)  $[P]/[S]$  dynamics determined for mass-action and GEEK models for different initial substrate concentrations  $[S]_{init}$  and different occupied volume fractions ( $\phi$ ) for the E. coli molecular weight distributions. The light dashed lines represent the dilute mass-action model, whereas the thin solid lines represent a population of 100 resampled GEEK models. (b) Time to half-equilibrium  $t_{eq/2}$  as a function of the occupied volume fraction for different initial substrate concentrations  $[S]_{init}$  is shown. The colors of the lines denote the different initial concentrations: blue corresponds to  $[S]_{init} = [S]_{ref}/4$ , yellow to  $[S]_{init} = [S]_{ref}$ , green to  $[S]_{init} = 2[S]_{ref}$ , and red to  $[S]_{init} = 4[S]_{ref}$ .

### 3.3. Effects of crowding on the reversible Michaelis Menten kinetics

parameters  $V_{max}^{+/-}$ ,  $K_{M,X,eff}$  decreased as a function of the inert occupied volume  $\phi$ , shown in figure 3.4, a and b respectively. These results complement our primary analysis because the maximal flux of the enzyme directly relates to the ability of the enzyme-substrate complex to dissociate, and the Michaelis-Menten constant is a measure of the affinity of the reactant binding to the enzyme. The lower the Michaelis-Menten constant, the higher the binding affinity to the enzyme. Consequently, a decreasing Michaelis-Menten constant indicates more enzyme bound at the same reactant concentration, or in other words, an increased enzyme saturation. For the effective flux through the enzyme, this results in two counteracting effects: a potential increase in flux due to an increase in saturation or a decrease in flux due to the reduced dissociation. From the analysis of  $t_{eq}/2$  and the effective Michaelis-Menten parameters, it is evident that the flux-increasing effect is dominating if enough free enzyme is available to increase the saturation. If the enzyme capacity does not allow more substrate to associate, the flux-decreasing effect dominates.

#### 3.3.4 Influence of crowder size on the Michaelis Menten kinetics

We further investigated the influence of the size of the inert molecules on the enzyme kinetics by comparing crowding with different inert molecule sizes obtained using the results for the *E. coli* size distribution. When comparing the  $t_{eq}/2$  as a function of the volume occupancy obtained from crowding using the *E. coli* distribution to the population consisting of a single inert molecule size, a general flux-decreasing effect was observed for crowding in the single-sized population, shown in figure 3.5 a. Furthermore, smaller inert molecule sizes showed a stronger flux-decreasing effect that was alleviated as the size of the inert molecules increased. When we compared the enzyme saturation at equilibrium for the different inert molecule sizes, the single-sized crowding showed an increased saturation, and smaller crowding sizes had a stronger effect, illustrated in figure 3.5 b. This shows that the overall substrate affinity is increased more if the inert molecules are smaller than the enzyme-substrate collision radius.

Finally, we determined the effective standard free energy of the reaction from the effective equilibrium constant  $\Delta_r G'^{\circ} = RT \ln(K_{eq})$  where the effective equilibrium constant was determined from the reactant concentrations at equilibrium  $K_{eq} = [P]_{eq}/[S]_{eq}$ , seen in figure 3.5 c. This showed that the overall apparent standard free energy of reaction does not vary significantly with crowding size or volume fraction. Because the nonideal contributions, which contain the terms emerging from molecular interactions, from steric interaction for the substrates and products are exactly equal, we would expect the overall nonideal contribution to the free energy of the enzymatic reaction to be zero. The deviation in the effective standard energy

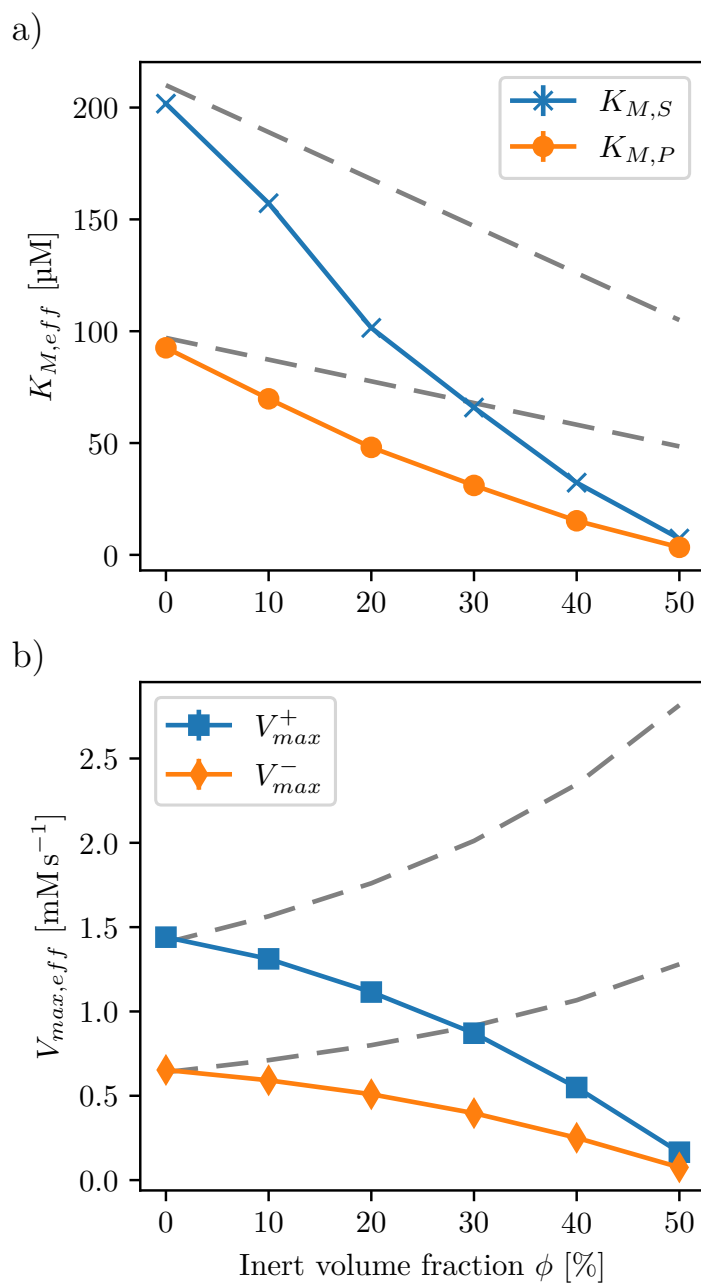


Figure 3.4 – Effective Michaelis-Menten parameters (a)  $K_{M,S}$  and  $K_{M,P}$  and (b)  $V_{max}^+$  and  $V_{max}^-$  as a function of volume fraction. The gray dashed lines represent the effective parameters when all concentrations are scaled to an effective volume  $V_{eff} = V(1 - \phi)$  that excludes the volume occupied by inert molecules. The errors in the values calculated from uniformly resampling the GEEK parameters are smaller than 2% of the mean.



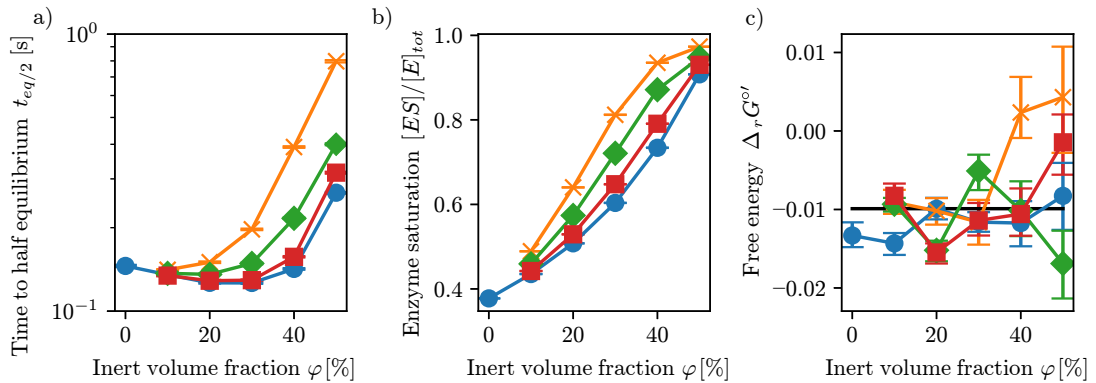


Figure 3.5 – Effects of the particle size distribution. (a) Time to half-equilibrium  $t_{eq}/2$ , (b) enzyme saturation  $[ES]/[E]_{tot}$  for  $[S]_{ref} = 49 \mu\text{M}$ , and (c) apparent standard free energy of the reaction measured as  $RT \log([P]_{eq}/[S]_{eq})$  under different crowding conditions are shown. The circles represents the apparent equilibrium measured from the *E. coli* size distribution; crosses, diamonds, and squares are obtained using a single size of inert molecules corresponding to the lower quartile, the median quartile, and the upper quartile of the *E. coli* size distribution, respectively. The error bars denote the upper and lower quartile of the resulting population that was obtained by resampling the GEEK model parameters within their confidence bounds. The horizontal black line denotes the equilibrium constant calculated from the in vitro kinetic parameters.

using GEEK can be attributed to the approximation over the state space at points far from equilibrium.

### 3.4 Discussion

In this chapter we present a method for characterizing spatial effects of any nature on biochemical reactions based on the mapping of average effects to ODEs. We, therefore, supplement recent work on the transport properties of macromolecule in heterogeneous environments (Grima et al., 2010; Smith et al., 2017) and improvements on Brownian reaction dynamics in crowded media (Smith and Grima, 2017), as well as efforts to integrate models for altered diffusion and rate constants into macroscopic transport equations (Grima and Schnell, 2007; Grima, 2010), with a framework that allows for efficiently characterizing the observable rate constant from Brownian reaction dynamics simulations. In addition, we consider the reaction-diffusion dynamics in a diverse, heterogeneous environment represented by a size distribution. Besides studying the effects of intracellular crowding as we have done, this framework can influence the study of membrane-confined biochemical reactions, enzyme channeling, and DNA- or actin-bound reaction systems, which are all current topics in biochemistry that lack

dedicated study tools.

Using a representative example, we confirm the hypothesis of recent research in the field that for reaction-limited enzyme kinetics, the diffusion effects in fractal spaces are negligible and are most likely not dominating in reaction networks. Instead, we confirm earlier research by Grima (2010) that observed a strong direct effect of crowding on the effective rates, for which a decrease in dissociation rates and an increase in association rates was observed when increasing occupied volume fraction. Both effects can be sufficiently explained by an effective increase of the crowding-induced potential with the volume fraction, confirming that this is a better predictor of intracellular enzyme kinetics than the diffusion. Furthermore, we show that the effective Michaelis-Menten parameters strongly depended on the volume occupancy and the size distribution of inert molecules, indicating that the kinetics is likely to vary dramatically in different cellular compartments. We finally show that crowding at a simplified network level can lead to a redistribution of the effective control on the flux response, suggesting that crowding can have a stabilizing effect with respect to fluctuation in enzyme levels, potentially indicating why enzymatic systems *in vivo* systems show higher robustness compared to *in vitro*.

## 4 Theoretical model of crowded kinetics

### 4.1 Introduction

In the previous chapter, we demonstrate that crowding alters the substrate affinity and the maximal enzyme rate of the Michaelis-Menten kinetics by approximating their kinetics using particle simulations based on the first physical principle. The presented method provides an essential speed up compared to the traditional particle simulation techniques, although it still requires substantial computational effort to construct the approximate models. These approximate models are also only able to characterize the effective reaction rate constants around a reference concentration state. In this chapter, we aim to create an improved model for the calculation of maximal velocity  $V_{max}$  and the Michaelis-Menten constants  $K_{M,i}$  that is suitable to calculate crowding corrections for a variety of enzyme mechanisms in large scale models. In the previous chapter, we further focused our efforts on simulating a single enzyme based on *in vitro* data instead of providing mechanistic insights into the observed phenomena.

Instead of a stochastic, agent-based model, we provide a mean-field model that can account for macromolecular crowding in terms of altered thermodynamic parameters, such as activities, equilibrium distribution functions, and diffusion coefficients. Mean-field models have been widely used to obtain effective chemical reaction constants for diffusion-limited, and diffusion influenced reaction kinetics. Thereby, studies focused mainly on the effects of diffusion on irreversible reaction kinetics, calculating the steady-state (Smoluchowski, 1927; Debye, 1942; Collins and Kimball, 1949a) or time-dependent reaction rate constants (Szabo, 1989). Later studies extended these models to study the effects of diffusion on reversible reactions (Agmon and Szabo, 1990; Szabo, 1991). These early models all have in common

## Chapter 4. Theoretical model of crowded kinetics

---

that they are considering the average association kinetics of a single reactant pair neglecting the changes in the pair distribution that originate from the bulk conversion rates. Gopich and Szabo (2002) have first taken into account these bulk conversion rates by linearizing the effective kinetics close to equilibrium. Their model produced good results for the relaxation times to equilibrium at the expense of not reproducing the correct irreversible limit. Their formalism was used by Szabo and Zhou (2012) to study the effects of diffusion on the two-step reversible Michaelis-Menten mechanism. The most recent contributions are the extension of the formalism of Szabo and Zhou (2012) for reaction networks by Gopich and Szabo (2018) and the introduction of crowding effects for the irreversible reactions employing an effective potential by Berezhkovskii and Szabo (2016).

All these studies demonstrated that under quasi-homogeneous conditions, the effects of diffusion on the effective reaction kinetics could be taken into account using a mean-field model based on the Smoluchowski equation (Smoluchowski, 1927). However, all studies on reversible reaction kinetics consider closed systems. This couples the non-equilibrium effects always to a decay dynamic so that they vanish at long times as the system approaches equilibrium. In a living organism, enzymatic reactions are driven out of equilibrium as they will be in a constant supply of nutrients that are catabolized to store chemical energy in the form of ATP, NADH, and NADPH as well as to produce the building blocks of macromolecules that make up the cells of the organism. As mentioned in the previous chapter, these reactants travel through a liquid environment where about 20–40% is occupied by a variety of macromolecules including proteins, RNA, DNA, and lipids (Ellis and Minton, 2003; Hall and Minton, 2003; Zhou et al., 2008; Rivas and Minton, 2018) to find their respective binding targets, catalysts or substrates. With some exceptions, such as active vesicle transport (Hirokawa and Takemura, 2005), their primary transport mechanism is diffusion.

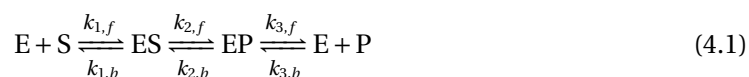
Zooming in on a single enzymatic reaction, we are left with a time-dependent, non-equilibrium reaction-diffusion system that is affected by multibody forces due to the interaction of the reactants with the macromolecules in its environment. We address the effects of the interaction with macromolecules on i) the diffusion, ii) the fluid-structure, and iii) the activities using a hard-sphere model. The properties of dense hard-sphere mixtures have been extensively studied during the second half of the 20th century. Especially for the fluid-structure and the species activity in hard-sphere mixtures there exist many reasonably good approximations, starting from the most simple ones derived from the Percus-Yevick equation (Lebowitz, 1964; Lebowitz and Rowlinson, 1964; Leonard et al., 1971) to Scaled Particle Theory (Helfand et al., 1960; Lebowitz et al., 1965) to more recent approximations (Grundke and Henderson, 1972;

Tang and Lu, 1995; Yuste et al., 1998). To model the effects of macromolecular crowding on the effective dissociation rate constant, we derive a dissociation rate based on the results of the previous chapter and the detailed balance. We likewise use the hard-sphere simulation results to find an approximation for the change of the effective diffusion constant in a hard-sphere mixture.

In this chapter, we present a non-equilibrium model of the Michaelis-Menten mechanism based on the Smoluchowski formalism derived by Gopich and Szabo (2018). We additionally present and validate analytical models for the effective diffusion constant, the effective dissociation rates, and the equilibrium radial distribution function in a dense hard-sphere fluid modeling macromolecular crowding conditions. For a simple association mechanism, we show analytically that the steady-state reaction rate constants of bi-molecular diffusion-controlled reactions strongly depend on the displacement from equilibrium. Reactions displaced towards association tend towards the irreversible Collins-Kimball rate constant. In contrast, reactions that are displaced towards dissociation experience an increase in the reaction rate as reassociation becomes more likely as diffusion becomes a limiting factor. We then use a finite element formulation of the full model of the Michaelis-Menten mechanism to determine how the effective Michaelis-Menten parameters of diffusion and reaction limited enzymes change. Finally, we show that the results of the bi-molecular diffusion-controlled reactions can be used to derive approximate expressions for the effective Michaelis-Menten parameters under crowded conditions, which are in good agreement with the finite element results.

## 4.2 Mathematical model

For the analysis presented in this chapter, we consider a prototypical reversible Michaelis-Menten mechanism consisting of three reversible reactions: i) association and dissociation of the substrate, ii) catalytic transformation, and dissociation, and iii) association of the product.



Both the association and dissociation reactions are strongly dependent on the transport of enzyme and substrate towards and away from each other. This transport is based on the effective diffusion constant as well as the accessible space for diffusion (Benichou et al., 2010; Trovato and Tozzini, 2014).

### 4.2.1 Pairwise reaction-diffusion model

The reaction rate of diffusion influenced reactions can be modeled by describing the time evolution of the pair distribution of the reactants at contact (Gopich and Szabo, 2018). This approach also allows accounting for many-body interactions by means of a potential of mean force that characterizes the deviation from the pair distribution function of an ideal solution at equilibrium (Gopich and Szabo, 2002; Kirkwood, 1935). The recently proposed theory for diffusion influenced reaction networks models bimolecular molecular reaction rates as a function of the pair-distribution  $\rho_{mn}$ . Previous work used analytical approximations to derive the time-dependent rate constants for closed systems near equilibrium (Gopich and Szabo, 2002, 2018). For this work, the theoretical description was adapted to model systems that maintain a steady-state far away from equilibrium. From the theoretical description of Gopich and Szabo (2018) the time-dependent bi-molecular reaction rates  $w_{mn,l}$  for the reaction  $[X_n][X_m] \rightarrow [X_l]$  are described by

$$w_{mn,l} = k_{mn \rightarrow l}^0 \int d\mathbf{r} \rho_{mn}(\mathbf{r}, t) \sigma_{mn,l}(\mathbf{r}) - k_{l \rightarrow mn} [X_l] \quad (4.2)$$

where  $k_{mn \rightarrow l}^0$  is the association rate constant in contact,  $k_{l \rightarrow mn}$  is the effective dissociation rate constant,  $\sigma_{mn,l}(\mathbf{r})$  is the probability that the reaction occurs for a pair with distance  $\mathbf{r}$ .

Gopich and Szabo (2018) modeled the time evolution of the pair-distributions  $\rho_{mn}$  by accounting for i) diffusion, ii) pair interconversion due to dissociation and association at the boundary as well as iii) pair interconversion due to reaction in the bulk. The corresponding equation describing the time evolution of the tensor  $P$  with elements  $\rho_{mn}$  is then:

$$\partial_t P = \nabla^2 (DP + PD) + KP + PK^T - R^{irr}(\mathbf{r}) \circ P - V(\mathbf{r}) \quad (4.3)$$

where  $\partial_t$  denotes the partial derivative with respect to time,  $D$  is a diagonal matrix with the effective self-diffusion coefficients and the elements  $\kappa_{ij}$  of  $K$ , describe the interconversion rates between pairs,  $R^{irr}$  are the irreversible association fluxes, and  $V$  are the effectively irreversible dissociation fluxes of reactions  $mn \rightarrow l$ , and  $\circ$  denotes element-wise matrix product, as introduced by Gopich and Szabo (2018). The bulk interconversion rates  $\kappa_{ij}$  account for the interconversion of the pair  $m, n$  to pairs  $m, i$  or  $j, n$  due to bulk reactions and are directly

derived from the effective reaction rate of the species  $m$  and  $n$  (Gopich and Szabo, 2018):

$$\kappa_{ij} = \partial_{[X_j]} \partial_t [X_i] \quad (4.4)$$

To describe an open system were up- and downstream processes responsible for the correlated creation and depletion of species, a source term  $S(\mathbf{r})$  is added to the equation (4.3). This source describes the difference from the bulk rate for the creation of a pair at a distance  $r$ . The source term is becoming non zero if the upstream or downstream processes create or deplete species in a correlated manner. This can be the case if the enzymes that produce the substrates upstream to the modeled enzyme are colocalized.

In addition to the source term the transport description of the model is refined accounting for crowding effects using the relative equilibrium radial distribution  $g_{mn}(\mathbf{r}) = \rho_{mn}(\mathbf{r})/[X_m][X_n]$ . The relative equilibrium radial distribution of each pair of species describes how the thermodynamic forces affect the pair distribution at equilibrium, i.e. in the absence any net reaction fluxes (Barker and Henderson, 1976). For dilute systems the relative equilibrium radial distribution is close to unity. Smoluchowski (1927) showed that the transport operator  $\mathcal{L}_{mn} = \nabla \cdot D_{mn} g_{mn}(\mathbf{r}) \nabla [g_{mn}(\mathbf{r})]^{-1}$  models the altered transport equilibrium correctly, were  $D_{mn}$  denotes the relative diffusion constant between species  $m$  and  $n$ . Introducing the source term and the refined transport of the partial differential equation describing the time evolution of the pair distribution  $P$  reads:

$$\partial_t P = \mathcal{L}P + KP + PK^T - R^{irr}(\mathbf{r}) \circ P - V(\mathbf{r}) + S_{mn}(\mathbf{r}) \quad (4.5)$$

The time evolution of the species bulk concentration is then given by

$$\frac{dX}{dt} = N_1 \mathbf{u}(X) + N_2 \mathbf{w}(P, X) + \mathbf{f} \quad (4.6)$$

where  $\mathbf{u}$  are the unimolecular reaction rates transforming species  $m \rightarrow n$  and  $\mathbf{w}$  are the modified reaction rates as described in equation (4.2) and  $\mathbf{f}$  denotes the source fluxes of material into the system.

We further consider that all molecules are spherical reactions only occur when two reacting species  $m$  and  $n$  are in contact. Therefore  $\sigma(\mathbf{r})$  reduces to the surface of the contact sphere

resulting in the simplification of equation (4.2):

$$w_{mn,l} = k_{mn \rightarrow l}^0 \rho_{mn}(R_{mn}, t) - k_{l \rightarrow mn} [X_l] \quad (4.7)$$

Due to the symmetry equation (4.5) can be easily expressed in radial coordinates. Further the terms  $R^{irr}(\mathbf{r}) \circ P$  and  $V(\mathbf{r})$  can be expressed as flux boundary at the contact sphere, similar to the original work of Gopich and Szabo (2002). We can thus express the dynamic equations for the pair distribution functions as

$$\rho_{mn} = r^{-2} \partial_r r^2 j_{mn} + \sum_k \kappa_{mk} \rho_{kn} + \sum_k \rho_{mk} \kappa_{nk} + s_{mn}(r) \quad (4.8)$$

$$j_{mn} = D_{mn} g_{mn}(r) \partial_r [g_{mn}(r)]^{-1} \rho_{mn} \quad (4.9)$$

subject to the boundary

$$4\pi R_{mn}^2 j_{mn}(R_{mn}) = \sum_l k_{mn \rightarrow l}^0 \rho_{mn}(R_{mn}) - k_{l \rightarrow mn} [X_l] \quad (4.10)$$

The resulting set of partial and ordinary differential equations can be solved exactly at equilibrium or for the steady-state with constant bulk concentrations. As we show later, an approximate solution can be found for closed systems with kinetics linearized close to equilibrium Gopich and Szabo (2002, 2018).

### 4.2.2 Finite element model

To solve the set of partial differential equations given in (4.8) subject to the boundary (4.10) together with the set of ordinary differential equations (4.6) for any system of elementary reactions a discretized model based on the finite element method (FEM) is derived. The finite element model is used to solve for the time derivative of  $\rho_{mn}$  at time  $t$  given by the partial differential equations. The time derivatives of the species concentrations  $\partial_t [X_m]$  and the time derivatives of the pair distributions are then integrated over time based on their initial values  $X^0$  and  $P^0$  solving for their time evolution.

To compute the time derivative of  $\rho_{mn}$  the spatial dependent quantities  $\partial_t \rho_{mn}$ ,  $\rho_{mn}$  and  $j_{mn}$  are approximated around the  $i$ th node using the basis functions  $\phi_i$  within the inter-



val  $[R_{mn}, L]$ .

$$\begin{aligned}
 \partial_t \rho_{mn} &\approx \partial_t \rho_{mn}^h = \sum_i \phi_i \partial_t \mathcal{P}_{mn,i} \\
 \rho_{mn} &\approx \rho_{mn}^h = \sum_i \phi_i \mathcal{P}_{mn,i} \\
 j_{mn} &\approx j_{mn}^h = \sum_i \phi_i \mathcal{J}_{mn,i}
 \end{aligned} \tag{4.11}$$

In this work, a set of second-order Lagrange basis functions is used (Larson and Bengzon, 2013). Then Galerkin's method is applied to derive an approximation for the partial differential equations. This method approximates the solution to the differential equation by constraining the weighted residuals for the approximated functions  $\partial_t \rho_{mn}^h$ ,  $\rho_{mn}^h$  and  $j_{mn}^h$  to 0 (Mikhlin, 1964). Applications of Galerkin's method to the partial differential equations in (4.8) result in two integral equations for every pair distribution:

$$0 = \sum_i \int_R^L \left\{ \phi_i \partial_t \mathcal{P}_{mn,i} - r^{-2} \partial_r r^2 [\phi_i \mathcal{J}_{mn,i}] - \sum_k \kappa_{mk} \phi_i \mathcal{P}_{kn,i} - \sum_k \phi_i \mathcal{P}_{mk,i} \kappa_{nk} - S_{mn} \right\} \phi_j dr \tag{4.12}$$

$$0 = \sum_i \int_R^L \{ J - D_{mn} g_{mn}(r) \partial_r [g_{mn}(r)]^{-1} [\phi_i \mathcal{P}_{mn,i}] \} \phi_j dr \tag{4.13}$$

To formulate the problem in terms of a matrix multiplication equations (4.12) and (4.13) may be rewritten as:

$$\begin{aligned}
 0 = \sum_i \int_R^L & \left[ \phi_i \phi_j \partial_t \mathcal{P}_{m,n,i} - 2r^{-1} \phi_i \phi_j \mathcal{J}_{m,n,i} - \partial_r \phi_i \phi_j \mathcal{J}_{m,n,i} \right. \\
 & \left. - \sum_k \kappa_{m,k} \phi_i \phi_j \mathcal{P}_{k,n,i} - \sum_k \phi_i \phi_j \mathcal{P}_{m,k,i} \kappa_{n,k} - S_{m,n} \phi_j \right]
 \end{aligned} \tag{4.14}$$

$$0 = \sum_i \int_R^L [\mathcal{J}_{m,n,i} \phi_i \phi_j - f_1 \partial_r f_2 \mathcal{P}_{m,n,i} \phi_i \phi_j - D_{mn} \mathcal{P}_{m,n,i} \partial_r \phi_i \phi_j] dr \tag{4.15}$$

with  $f_1 = D_{mn} g_{mn}(r)$  and  $f_2 = [g_{mn}(r)]^{-1}$ . Summarizing the discretizations of the integration variables into the vectors  $\partial_t \vec{\mathcal{P}}_{m,n}$ ,  $\vec{\mathcal{P}}_{m,n}$  and  $\vec{\mathcal{J}}_{m,n}$  we can express the integral equations in

## Chapter 4. Theoretical model of crowded kinetics

terms of the matrix equations  $A^{mn}$ ,  $B_1^{mn}$ ,  $B_2^{mn}$  and the vector  $\vec{C}^{mn}$ :

$$\vec{0} = A^{mn} \cdot \partial_t \vec{\mathcal{P}}_{m,n} - B_1^{mn} \cdot \vec{\mathcal{J}}_{m,n} - \sum_k \kappa_{m,k} A^{mn} \cdot \vec{\mathcal{P}}_{k,n} - \sum_k A^{mn} \cdot \vec{\mathcal{P}}_{m,k} \kappa_{n,k} - \vec{C}^{mn} \quad (4.16)$$

$$\vec{0} = A^{mn} \cdot \vec{\mathcal{J}}_{m,n} - B_2^{mn} \cdot \vec{\mathcal{P}}_{m,n} \quad (4.17)$$

where elements of  $A$ ,  $B_1$  and  $B_2$  and  $\vec{C}$  are calculated by integration over the basis functions:

$$A_{ij}^{mn} = \sum_i \int_R^L \phi_i \phi_j dr \quad (4.18)$$

$$B_{1,ij}^{mn} = \sum_i \int_R^L 2r^{-1} \phi_i \phi_j + \partial_r \phi_i \phi_j dr \quad (4.19)$$

$$B_{2,ij}^{mn} = \sum_i \int_R^L f_1 \partial_r f_2 \phi_i \phi_j - D_{mn} \partial_r \phi_i \phi_j dr \quad (4.20)$$

$$\vec{C}_j^{mn} = \sum_i \int_R^L S_{mn} \phi_j dr \quad (4.21)$$

The time differential of the discretized radial distribution functions at time  $t$  are thus computed as follows:

$$\vec{\mathcal{J}}_{m,n}(t) := (A^{mn})^{-1} B_2^{mn} \cdot \vec{\mathcal{P}}_{m,n}(t) \quad (4.22)$$

$$\mathcal{J}_{m,n,0}(t) := \frac{\sum_l k_{mn \rightarrow l}^0 \mathcal{P}_{m,n,0} - k_{l \rightarrow mn} [X_l]}{4\pi R_{mn}^2} \quad (4.23)$$

$$\partial_t \vec{\mathcal{P}}_{m,n}(t) := (A^{mn})^{-1} B_1^{mn} \cdot \vec{\mathcal{J}}_{m,n}(t) + \sum_k \kappa_{m,k} \vec{\mathcal{P}}_{k,n} - \sum_k \vec{\mathcal{P}}_{m,k} \kappa_{n,k} - \vec{C}^{mn} \quad (4.24)$$

where  $(A^{mn})^{-1}$  denotes the inverse matrix of  $A^{mn}$ . Simultaneous time integration of  $\partial_t \vec{\mathcal{P}}_{m,n}(t)$  and  $\partial_t X$  yields a numerical solution for the time course of species and pair distributions.

We solve the finite element problem on the integration domain  $[R_{mn}, L]$  with  $L = 100R_{mn}$  using a discretization of  $N_E = 100$  elements on a linearly increasing grid, i.e., the nodes are equidistant in the  $1/r$  space. To test whether the proposed FEM model converges to the solution of the differential equation, we test the model against the steady-state analytical solution of the pair distribution function of an irreversible bi-molecular reaction Collins and Kimball (1949a). Our results indicate that the FEM model converges to the analytical solution in the limit of  $[L, N_E] \rightarrow [\infty, \infty]$  (Figure 4.1 A and B)

For the time integration, a variable order backward differentiation formula (BDF) scheme is used as implemented by the CVODE solver implementation of SUNDIALS (Serban and

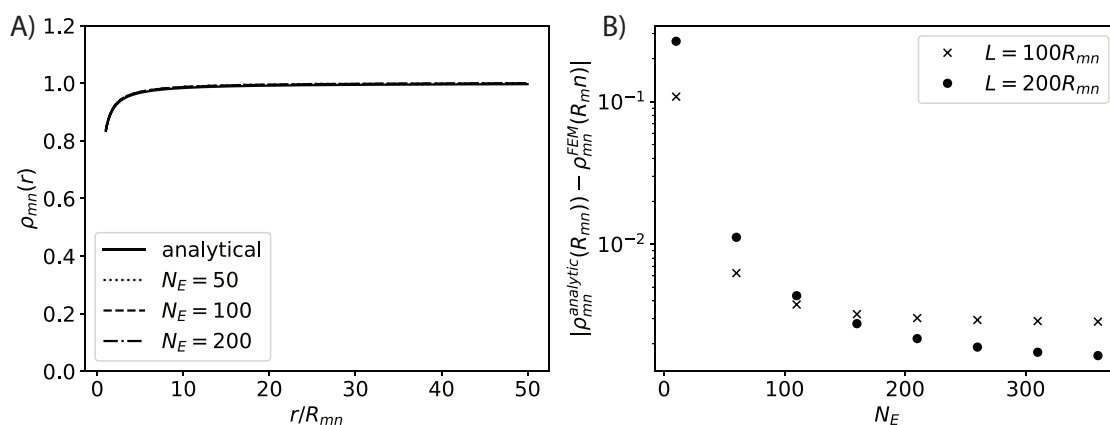


Figure 4.1 – A) Comparison of the analytical solution for the pair-distribution function  $\rho_{mn}$  for an irreversible reaction  $m + n \rightarrow l$  with constant concentrations and at steady state at different discretizations  $N_E$ . B) Error at of the pair distribution  $\rho_{mn}$  function at the collision interface as a function of  $N_E$  and  $L$ .

Hindmarsh, 2005; Hindmarsh et al., 2005).

### 4.3 Effects of crowding on the model parameters

The presence of macromolecules in the reaction domain can actively alter the effective diffusion constant by obstruction of the mean free path, the equilibrium pair distribution, and the effective dissociation rate by reducing the available volume (Minton, 1981; Zhou et al., 2008). The reduction of the available volume near dissociation complexes additionally reduces the effective dissociation rate constants (Grima, 2010; Weilandt and Hatzimanikatis, 2019). The presence of macromolecules is taken into account by analytical models that describe the changes of these three parameters as a function of the volume occupancy and macromolecular size distribution.

#### 4.3.1 Equilibrium radial distribution function

As discussed in the introduction, many different approximations have been developed to calculate the equilibrium pair distribution in hard-sphere mixtures. In this chapter, the solution derived from the Percus-Yevick closure of the Ornstein-Zernike compressibility relation is used to compute the equilibrium pair distribution functions for a  $m$  component mixture of hard-spheres with the radius  $R_l$  and the number density  $\rho_l$ . Like for all analytical approximations of the equilibrium pair distribution functions the expression for  $g_{mn}(r)$  is derived by introducing the Laplace transform of  $r g_{mn}(r)$  as an explicit closed form of  $g_{mn}(r)$  can not be

## Chapter 4. Theoretical model of crowded kinetics

---

obtained (Lebowitz, 1964; Blum and Hoeye, 1977):

$$G_{mn}(s) = \int_0^{\infty} dt e^{-sr} r g_{mn}(r) \quad (4.25)$$

The generalized expressions for the laplace tansfrom of a  $m$  component mixture are defined by the following set of equations (Lebowitz, 1964; Blum and Hoeye, 1977):

$$G_{mn}(s) = \frac{e^{sR_{mn}}}{sD\Delta} \left\{ s \left[ R_{mn} + R_m R_n \frac{\pi}{\Delta} \xi_2 \right] + 1 + \frac{\pi}{2\Delta} \xi_3 + \frac{2\pi s}{\Delta} \sum_l \rho_l \theta_1(2R_l)(R_l - R_i)(R_l - R_j) \right\} \quad (4.26)$$

with the denominator

$$D = 1 - \frac{2\pi}{\Delta} \left\{ \sum_l \rho_l \theta_1(2R_l) \left[ 2R_l \left( 1 + \frac{\pi}{2\Delta} \xi_2 R_l \right) + \frac{\pi}{\Delta} \sum_k \rho_k \theta_1(2R_k)(R_k - R_l)^2 \right] \right\} - \frac{2\pi}{\Delta} \sum_l \rho_l \theta_2(2R_l) \left( 1 + \frac{\pi}{2\Delta} \xi_3 \right) \quad (4.27)$$

The functions  $\theta_1$  and  $\theta_2$  are modified gamma functions of the form

$$\theta_1(\sigma_k) = (1 - s\sigma_k - e^{-s\sigma_k})/s^2 \quad (4.28)$$

$$\theta_2(\sigma_k) = (1 - s\sigma_k + s^2\sigma_k^2/2 - e^{-s\sigma_k})/s^3 \quad (4.29)$$

and  $\xi_2$ ,  $\xi_3$  and  $\Delta$  are given as the following expressions:

$$\xi_2 = \sum \rho_k (2R_k)^2 \quad (4.30)$$

$$\xi_3 = \sum \rho_k (2R_k)^3 \quad (4.31)$$

$$\Delta = 1 - \pi \xi_3 / 6 \quad (4.32)$$

Numerical inversion of the Laplace transform  $G_{mn}(s)$  allows then to calculate  $g_{mn}(r)$ . The algorithm developed by de Hoog et al. (1982) is deployed to compute the inverse Laplace transform using the implementation in the python package *mpmath* (Johansson et al., 2013). To compute the radial distribution function, we assume that the components of the system, i.e., enzymes [E], enzyme complex [ES], [EP], substrate [S], and product [P] concentrations are sufficiently small so that their effect on the overall occupied volume is negligible. This assumption holds for most individual components of a cell (Ellis and Minton, 2003). To model the macromolecular mixture in the intracellular environment, we use the same size distribution model as used in chapter 3 based on the work of Kalwarczyk et al. (2012). As the inversion of the Laplace transform is computationally expensive, the size molecular size

### 4.3. Effects of crowding on the model parameters

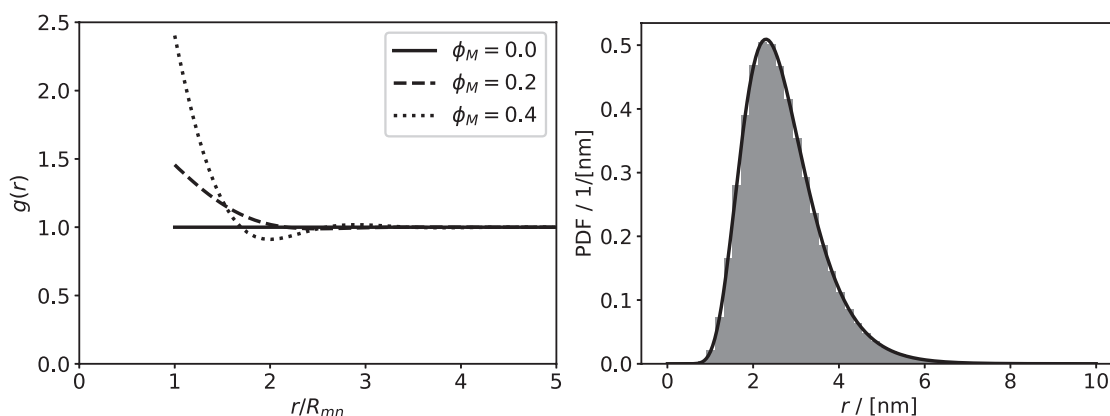


Figure 4.2 – A) Equilibrium radial distribution functions for a pair pair  $m, n$  with  $R_m = 1$  nm and  $R_n = 3$  nm in a mixture of hard-spheres with  $\phi = 0.0$  (line),  $\phi = 0.2$  (dashed) and  $\phi = 0.4$  (dotted) fraction of macromolecules following the discrete size distribution given in B) Discrete (bars) and continuous (line) size distribution of macromolecules Kalwarczyk et al. (2012).

distribution function is discretized to approximate this continuous size distribution function (see figure 4.2 part B). Examples for the numerical calculation of radial distribution functions for a pair  $m, n$  with  $R_m = 1$  nm and  $R_n = 3$  nm are shown in figure 4.2 part A for macromolecular volume fractions of 0% 20% and 40%.

#### 4.3.2 Effective dissociation constant

The previous chapter showed that the effective dissociation rate constant depends on macromolecular crowding conditions, see section 3.3.2. To model the effect of macromolecules on the dissociation rates a dissociation probability  $p_d$ , with  $d \in [(E, S \rightarrow ES), (EP \rightarrow E, P)]$  is introduced to describe how a macromolecular solution affects the possibility of an associated complex to dissociate. The effective dissociation rate constant is then given as the dissociation react constant in dilute conditions multiplied with a dissociation probability that accounts for the effects of macromolecular crowding  $k_d = p_d k_{d,0}$ . The probability model considers that if dissociation of a species  $l$  into a pair  $m, n$  leads to a reduction in the excess free energy the reaction probability remains equal to one and an increase in the excess free energy will reduce the probability by the Boltzmann factor between the increased energies of the dissociated and associated state  $\exp(-\beta \Delta \Delta F_{mn \rightarrow l})$ , where  $\Delta \Delta F_{mn \rightarrow l}$  is the difference of the excess free energy of the product pair in contact  $\Delta F_{mn}$  with respect to the educt  $\Delta F_l$ . The excess free energy of a pair in contact  $\Delta F_{mn}$  is calculated based on the thermodynamic cycle to introduce a pair in contact and separate this pair under ideal and crowded conditions, see figure 4.3. As in an ideal solution there exists no barrier to separate a pair, i.e.,  $\Delta E_s^0 = 0$ , the excess free energy of

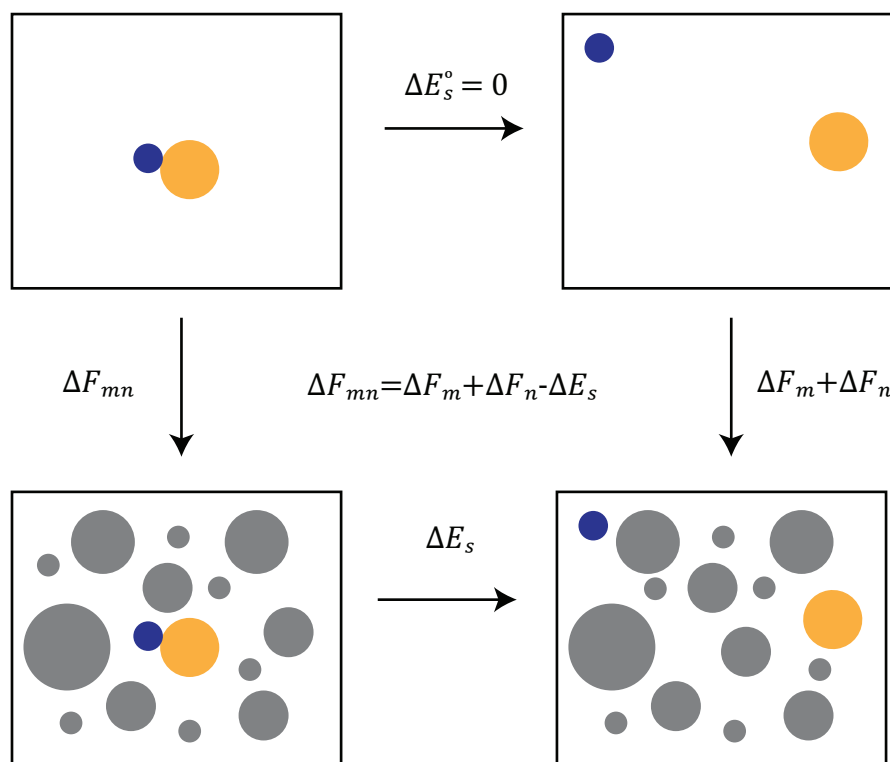


Figure 4.3 – Calculation of the excess free energy, based on the thermodynamic equivalence of i) introducing a pair into an ideal solution, separating it and introducing crowded molecules, and ii) introducing the pair in contact into a solution with the same crowding properties and then separate it.

introducing a pair into a crowded solution can then be calculated by the excess free energy of the individual species  $\Delta F_m$  and  $\Delta F_n$  and the energy that is necessary to separate that pair in crowded conditions  $\Delta E_s$ .

The difference of the excess energy  $\Delta\Delta F_{m,n \rightarrow l}$  can then be calculated as

$$\Delta\Delta F_{mn \rightarrow l} = \Delta F_{mn} - \Delta F_l = \Delta F_m + \Delta F_n - \Delta F_l - \Delta E_s \quad (4.33)$$

The excess free energies for the individual compounds is calculated, like the equilibrium radial distribution function, based on expressions derived from the Percus-Yevick approximation for

### 4.3. Effects of crowding on the model parameters

a hard-sphere mixture (Lebowitz and Rowlinson, 1964):

$$\begin{aligned} \beta \Delta F_m = \beta \mu_m^{ex} = & -\ln(1 - \zeta_3) + \frac{\pi}{6} \beta p^c (2R_m)^3 \\ & + \frac{(2R_m)^2}{(1 - \zeta_3)^3} \left[ 3\zeta_1 - 6\zeta_3\zeta_1 + \frac{9}{2}\zeta_2^2 - \frac{9}{2}\zeta_3\zeta_2^2 + 3\zeta_3^2\zeta_1 \right] \\ & + \frac{2R_m}{(1 - \zeta_3)^3} [3\zeta_2 - 6\zeta_3\zeta_2 + 3\zeta_3^2\zeta_2] \end{aligned} \quad (4.34)$$

where  $\zeta_i = \sum_l \rho_l (R_l)^i \pi/6$  and the compressibility consistent pressure (Lebowitz and Rowlinson, 1964):

$$\beta p^c = \left\{ \sum_l \rho_l (1 + \zeta_3 + \zeta_3^2) - 6\pi \sum_{l,k} \rho_l \rho_k (R_l - R_k)^2 [2R_{lk} + 4R_l R_k \zeta_2] \right\} (1 - \zeta_3)^{-3} \quad (4.35)$$

The energy necessary to separate a pair  $m, n$  can be obtained by considering that the equilibrium pair distribution can be interpreted as the exponential of the potential of mean force between species  $m$  and  $n$ ,  $g_{mn}(r) = \exp(-\beta U_{mn}(r))$  (Kirkwood, 1935). The energy necessary to separate the species is then

$$\Delta E_s = \lim_{L \rightarrow \infty} \int_{R_{mn}}^L dr \partial_r U_{mn}(r) = \lim_{L \rightarrow \infty} U_{mn}(L) - U_{mn}(R_{mn}) \quad (4.36)$$

In a fluid, the pair distribution function tends to 1 for large  $r$  the potential of mean force tends to 0 for large  $r$  (Kirkwood, 1935). Expressing the separation energy in terms of the radial distribution of  $m$  and  $n$  in contact  $g_{mn}(R_{mn})$  then yields:

$$\Delta E_s = -U_{mn}(R_{mn}) = -\beta^{-1} \ln(g_{mn}(R_{mn})) \quad (4.37)$$

The value of the equilibrium radial distribution function in contact can be obtained from the inverse Fourier transform or using Percus-Yevick the expressions derived by Lebowitz (1964):

$$g_{mn}(R_{mn}) = \frac{R_m g_{nn}(R_n) + R_n g_{mm}(R_m)}{R_m + R_n} \quad (4.38)$$

$$g_{mm}(R_m) = \frac{(1 - \zeta_3) + \zeta_2 R_m}{(1 - \zeta)^2} \quad (4.39)$$

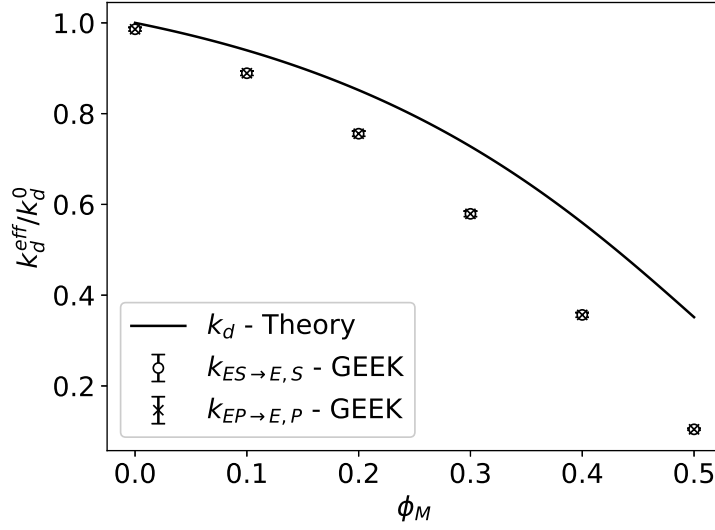


Figure 4.4 – Change of the relative dissociation constant calculated using the hard-sphere model of PGM as presented in the previous chapter (circles and crosses) compared to the theoretical model derived in this chapter (solid line). The changes for the theoretical model are calculated based on the size distribution of macromolecules by Kalwarczyk et al. (2012) and for species  $l$  with  $R_n = 3$  mn dissociating into pairs  $m, n$  with sizes  $R_m = 1$  mn and  $R_n = 3$  mn.

Using the above-derived results, the effective dissociation rate constants are:

$$k_{mn \rightarrow l} = \begin{cases} k_{mn \rightarrow l}^0 & \text{if } \Delta\Delta F_{mn \rightarrow l} \leq 0 \\ k_{mn \rightarrow l}^0 \exp(-\beta\Delta\Delta F_{mn \rightarrow l}) & \text{if } \Delta\Delta F_{mn \rightarrow l} > 0 \end{cases} \quad (4.40)$$

with  $\Delta\Delta F_{m:n \rightarrow l} = \Delta F_m + \Delta F_n - \Delta F_l + \beta^{-1} \ln(g_{mn}(R_{mn}))$ . As  $\Delta F_m$  are the excess free energies equation 4.40 can also be expressed in terms of the activity coefficients  $\gamma_m$ . Were the activity coefficients relate to the excess free energies  $\gamma_m = \exp(\beta\Delta F_m)$ :

$$k_{mn \rightarrow l} = \begin{cases} k_{mn \rightarrow l}^0 & \text{if } g_{mn}(R_{mn})\gamma_{mn \rightarrow l} \geq 1 \\ k_{mn \rightarrow l}^0 g_{mn}(R_{mn})\gamma_{mn \rightarrow l} & \text{if } g_{mn}(R_{mn})\gamma_{mn \rightarrow l} < 1 \end{cases} \quad (4.41)$$

with the overall change in reaction activity  $\gamma_{mn \rightarrow l} = \gamma_l(\gamma_m\gamma_n)^{-1}$ .

Comparing the effective dissociation rate to the changed dissociation rates as calculated from the hard-sphere Brownian reaction dynamics model presented in the previous chapter (Figure 4.4) indicates that the energy-based models presented in this chapter predict a weaker effect on the dissociation rate constant than the hard-sphere model. The difference in the



models originates from their different assumptions. The hard-sphere model assumes that any dissociation process that encounters a hindrance cannot occur. This model implies that the macromolecules' positions cannot change during the dissociation step. In the theoretical model, we introduce the dissociation probability as the Boltzmann factor between the associated and the dissociated state, i.e., the product pair in contact. In contrast to the hard-sphere model, this model considers that an increase in free energy reduces the probability of transition towards this state, accounting for the possibility that the macromolecules position can change during the dissociation step.

#### 4.3.3 Effective diffusion constant

The final model parameter that is impacted by the presence of macromolecules is the effective diffusion constant of the reacting species. Diffusion in the intracellular environment is anomalous due to interactions of the diffusing species with the macromolecules (Hofling and Franosch, 2013; Hasnain et al., 2014). In this work, these interactions are reduced to the hard-sphere repulsion that leads to volume exclusion and exchange of momentum upon collision. The path of a tracer molecule in a solution of water is naturally driven by the thermal fluctuations of the water molecules surrounding it. In the hard-sphere mixture, this path changes with each collision with another molecule leading to a reduction in the effective self-diffusion constant. The critical parameter for the reaction-diffusion model described above is the relative diffusion between the reacting species. In a quasi-homogeneous solution, this relative diffusion constant is given by the sum of the self-diffusion coefficients. In the literature, approaches to calculate the self-diffusion coefficients for hard-sphere suspensions consisting out of single-sized spheres (Leegwater and Szamel, 1992). For mixtures of hard-spheres, models are limited to two-component mixtures (Imhof and Dhont, 1995; Peppin, 2019) and consider high volume fractions of the individual components. As discussed above, the diffusion-reaction model presented in this chapter is based on the assumption that the individual components of the system only occupy a small fraction of the volume. In the absence of a theory for Brownian diffusion in hard-sphere mixtures, we approximate the effects of macromolecular crowding on the effective diffusion using hard-sphere simulations, see figure 4.5. We calculate the effective diffusion constant using the mean squared displacement as a function of time and the relation  $\langle \mathbf{x}_m - \mathbf{x}_m^0 \rangle = 6D_m t$ , where  $\mathbf{x}$  are the positions of the tracer particles Einstein (1905). Up to macromolecular volume fractions of about 0.4%, the effective

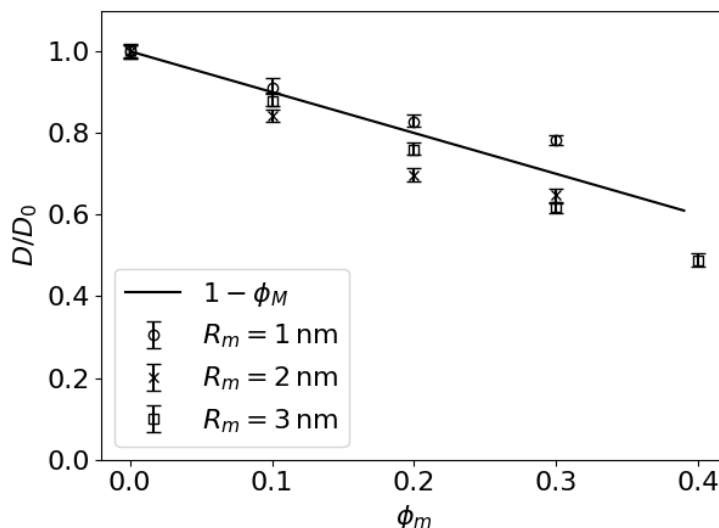


Figure 4.5 – Effective diffusion coefficient as a function of the macromolecular volume fraction for species with  $R_1 = 1$  nm (circles),  $R_1 = 2$  nm (crosses) and  $R_1 = 3$  nm (squares) in a hard-sphere mixture following the size distribution given in Kalwarczyk et al. (2012).

diffusion constants are reasonably approximated by the linear relation:

$$D_m \approx D_m^0(1 - \phi_M) \quad (4.42)$$

here  $D_m^0$  denotes the diffusion constant of species  $m$  in a dilute aqueous solution.

#### 4.4 Apparent reaction rates at equilibrium

When macromolecules are introduced into a closed system at equilibrium, the system is displaced into a non-equilibrium state. The interactions between macromolecules and reactants cause this displacement by changing the chemical potential of the reactants. After sufficient time the closed system will settle in a new equilibrium state. This equilibrium state is defined by the altered rate constants that arise from altered pair distributions in the presence of macromolecules. As the above-described model for diffusion influenced reaction networks considering macromolecular crowding can be solved at equilibrium, we derive the basic equilibrium relations for the three-step Michaelis-Menten mechanism.

In a first step, we calculate the equilibrium relations for the bimolecular reactions  $E, S \rightleftharpoons ES$  and  $EP \rightleftharpoons E, P$ . From equation (4.2) and the definition of  $g_{mn}(r)$ , it follows that at equilibrium

#### 4.4. Apparent reaction rates at equilibrium

the relative pair distribution  $\rho_{mn}(r)/[X_m][X_n]$  of species  $m$  and  $n$  is  $g_{mn}(r)$ . Introducing these result into equation 4.2 and considering that at equilibrium, all net reaction rates are zero, we find the equilibrium relation for bimolecular reactions:

$$K_{mn \rightarrow l, eq}^{app} = \frac{[X_l]_{eq}}{[X_m]_{eq}[X_n]_{eq}} = \frac{k_{mn \rightarrow l}^0 \int d\mathbf{r} g_{mn}(\mathbf{r}) \sigma_{mnl}(\mathbf{r})}{k_{l \rightarrow mn}} \quad (4.43)$$

Considering the spherically symmetric partially absorbing boundary at contact, and the model of the effective dissociation constant, see above equations (4.10) and (4.41), we show that the equilibrium constant is shifted by the activity coefficients of the products and educts. This result recovers the well-known relation obtained from thermodynamic considerations (Zhou et al., 2008):

$$\begin{aligned} K_{mn \rightarrow l, eq}^{app} &= \frac{k_{mn \rightarrow l}^0 g_{mn}(R_{mn})}{k_{l \rightarrow mn}^0 g_{mn}(R_{mn}) \gamma_{l \rightarrow mn}} \\ &= K_{mn \rightarrow l, eq}^0 \frac{\gamma_l}{\gamma_m \gamma_n} \\ &= K_{mn \rightarrow l, eq}^0 e^{\beta(\Delta F_l - \Delta F_m - \Delta F_n)} \end{aligned} \quad (4.44)$$

As unimolecular reactions are neither affected by the diffusion nor by the pair distribution function, they are not subject to any effects in the above-presented model. In the three-step Michaelis-Menten mechanism, only the biotransformation in the catalytic pocket is a unimolecular reaction and thus not subject to any macromolecular effects. Therefore the effective equilibrium constant for the unimolecular reactions is equal to their ideal.

$$K_{m \rightarrow n, eq}^{app} = K_{m \rightarrow n, eq}^0 \quad (4.45)$$

Nevertheless, it has been suggested that crowding can stabilize enzyme configurations and result in a change of the effective reaction rate constants of this transformation (Kinjo and Takada, 2002; Xu et al., 2017). We note that with the presented model such effects can be taken into account if the impact of macromolecules on the effective forward and backward rates is known.

Considering the elementary reaction scheme for the Michaelis-Menten mechanism in 4.1 the

overall apparent equilibrium constant is

$$\begin{aligned} K_{eq}^{app} &= K_{E,S \rightarrow ES,eq}^{app} K_{ES \rightarrow EP,eq}^{app} K_{EP \rightarrow E,P,eq}^{app} \\ &= K_{E,S \rightarrow ES,eq}^0 K_{ES \rightarrow EP,eq}^0 K_{EP \rightarrow E,P,eq}^0 \frac{\gamma_{ES}}{\gamma_E \gamma_S} \frac{\gamma_E \gamma_P}{\gamma_{EP}} \end{aligned} \quad (4.46)$$

with  $K_{E,S \rightarrow ES,eq}^0 K_{ES \rightarrow EP,eq}^0 K_{EP \rightarrow E,P,eq}^0 = K_{eq}^0$ .

If the enzyme-substrate and enzyme-product complex are of the same size their activity coefficients  $\gamma_{ES}$  and  $\gamma_{EP}$  are equal, and the expression for the apparent equilibrium constant further simplifies to

$$K_{eq}^{app} = K_{eq}^0 \frac{\gamma_P}{\gamma_S}. \quad (4.47)$$

From these relations, it is clear that the apparent equilibrium is only effected by macromolecular crowding if i) the effective size of the substrate and product is different, ii) the enzyme-substrate complex changes in size when transforming the substrate to the product, or iii) the apparent  $K_{ES \rightarrow EP}^{app}$  is effected due to a changed enzyme conformation. For Uni-Uni enzyme reactions, the effective size of the substrate is unlikely to change as the mass of the molecule is conserved. Still, for other enzyme stoichiometries, the equilibrium constant may be significantly affected by crowding, as suggested by Angeles-Martinez and Theodoropoulos (2015).

## 4.5 Non-equilibrium effects on steady-state reaction rates

In a living organism, external driving forces such as a constant supply of substrates maintain steady-state displaced from equilibrium. This situation requires a constant net transport of enzyme and substrate molecules towards and a constant transport of enzymes and product molecules away from each other. Under constant growth conditions, the metabolic enzymes in the cell operate at a quasi-steady state (Monod, 1949; Campbell, 1957; Heineken et al., 1967; Salvy and Hatzimanikatis, 2020). To investigate these steady-state properties in the presence of macromolecular crowding, we first investigate the properties of the elementary reaction and then simulate the steady-state behavior of the Michaelis-Menten mechanism. We further derive an analytical approximation for the effective Michaelis-Menten parameters based on the properties of the elementary reactions.

### 4.5.1 Elementary reactions

As mentioned above, Biochemical reactions inside the cells often operate at a non-equilibrium steady state. A simple model to account for such a situation can be modeled as an association reaction  $E, S \rightleftharpoons ES$  that is subject to constant bulk concentrations. The constant bulk concentrations model that there exists an upstream and downstream process that continuously maintains the value of the concentration. For this simple model, it is possible to find an analytical expression for steady-state reaction flux. As the bulk concentration are assumed to be constant the bulk conversion rates  $\kappa_{ij}$  reduce to zero reducing all equations for the pair distribution function, except for  $m = E, n = S$  and  $m = S, n = E$ , to  $\partial_t \rho_{mn} = L_{mn}(D_{mn}\rho_{mn})$ . The steady-state solution for the operator  $L_{mn}$  is  $g_{mn}(r)$ . Due to symmetry  $\rho_{mn} = \rho_{nm}$  the system is completely described by the following set of equations:

$$\rho_{mn} = r^{-2} \partial_r r^2 D_{E,S} g_{E,S}(r) \partial_r [g_{E,S}(r)]^{-1} \rho_{E,S} \quad (4.48)$$

subject to the boundary

$$4\pi R_{E,S}^2 j_{E,S}(R_{E,S}) = k_{E,S \rightarrow ES}^0 \rho_{E,S}(R_{E,S}) - k_{ES \rightarrow E,S}[ES] \quad (4.49)$$

We follow the derivation of Szabo (1989) by formally solving the inhomogeneous equation as  $[C_1 - C_2 f(r)]g(r)$  with  $f(r)$  being the solution of the homogeneous equation, i.e  $g(r) = 1$  and subsequently comparing the constants for diffusion-limited boundary  $\rho_{E,S}(R_{E,S}) = 0$  with the constants for above described boundary. Introducing the diffusion limited interface flux as  $k_{E,S \rightarrow ES}^{sm}[E][S]$  we find the flux at the boundary to be:

$$v_{E,S \rightarrow ES} = \frac{k_{E,S \rightarrow ES}^0 g(R_{E,S}) \left( k_{E,S \rightarrow ES}^{sm} + k_{ES \rightarrow E,S} \frac{[ES]}{[E][S]} \right)}{k_{E,S \rightarrow ES}^0 g(R_{E,S}) + k_{E,S \rightarrow ES}^{sm}} [E][S] - k_{ES \rightarrow E,S}[ES] \quad (4.50)$$

where  $k_{E,S \rightarrow ES}^0$  is the reaction rate at constant,  $k_{E,S \rightarrow ES}^{sm}$  is the Smoluchowski (diffusion limiting) rate constant and  $k_{ES \rightarrow E,S}$  is the effective dissociation rate constant.

### 4.5.2 Enzymatic reactions

Next, we characterize the effects of macromolecular crowding on different enzymes following the Michaelis-Menten mechanism described in equation 4.1. We parameterize the rate constants of the enzyme in a diluted environment based on six kinetic parameters in addition to the size of the species and their dilute diffusion constants. We then use *in silico* enzyme assays

## Chapter 4. Theoretical model of crowded kinetics

---

to determine the maximal enzyme velocity  $V_{max}$  and the Michaelis-Menten constants  $K_M$ .

These kinetic parameters are the overall standard free energy of the reaction  $\Delta_{S \rightarrow P} G^0$ , the substrate and product dissociation constants  $K_{D,E,S \rightarrow ES}$  and  $K_{D,E,P \rightarrow EP}$ , the ratio of rate constant in contact to diffusion limitation rate to for the substrate association and the product association  $d_{E,S \rightarrow ES}$  and  $d_{E,P \rightarrow EP}$  and finally the rate of the biocatalytic transformation  $k_{ES \rightarrow EP}$ . In a first step, the diffusion-limited rate constants are determined from the size and the diffusion constant of the reactants (Smoluchowski, 1927). Thereby the diffusion constants  $D_m$  are calculated from the radius  $R_m$  based on the Stokes-Einstein relation given in 3.28.

$$\gamma_{mn \rightarrow l} = 4\pi D_{mn} R_{mn} \quad (4.51)$$

From this the association rate constants at contact for the substrate product association are calculated via the ratios  $d_{E,S \rightarrow ES}$  and  $d_{E,P \rightarrow EP}$  as

$$k_{E,S \rightarrow ES}^0 = d_{E,S \rightarrow ES} \gamma_{E,S \rightarrow ES} \quad (4.52)$$

$$k_{E,P \rightarrow EP}^0 = d_{E,P \rightarrow EP} \gamma_{E,P \rightarrow EP}. \quad (4.53)$$

Subsequently, the ideal dissociation rate constants are calculated from the ideal association rate constants at contact and the dissociation constants  $K_{D,E,S \rightarrow ES}$  and  $K_{D,E,P \rightarrow EP}$  as

$$k_{ES \rightarrow E,S}^0 = k_{E,S \rightarrow ES}^0 K_{D,E,S \rightarrow ES} \quad (4.54)$$

$$k_{EP \rightarrow E,P}^0 = k_{E,P \rightarrow EP}^0 K_{D,E,P \rightarrow EP} \quad (4.55)$$

Finally, the reverse biocatalytic rate  $k_{EP \rightarrow ES}$  is calculated based on the overall Gibbs free energy  $\Delta_{S \rightarrow P} G^0$  and the dissociations rate constants  $K_{D,E,S \rightarrow ES}$  and  $K_{D,E,P \rightarrow EP}$ .

$$k_{EP \rightarrow ES} = e^{-RT\Delta_{S \rightarrow P} G^0} K_{D,E,S \rightarrow ES} K_{D,E,P \rightarrow EP} \quad (4.56)$$

The rate and diffusion constants are then modified according to the crowding models presented above in thorough sections 4.3.1 to 4.3.3, introduced into the model discussed in section 4.2.1 and solved using the finite element scheme presented in section 4.2.2 with constant boundary conditions for  $[S]$  and  $[P]$  at different substrate concentrations with  $[P] = 0$ . The maximal velocity  $V_{max}^{app}$  and  $K_{M,S}$  are then extracted from the enzyme flux as a function of the substrate concentrations, see figure 4.6. As a first study, we choose an enzyme model with  $R_E = R_{ES} = R_{EP} = 3 \text{ nm}$  and  $R_S = R_P = 1 \text{ nm}$ . The respective diffusion constants are

#### 4.5. Non-equilibrium effects on steady-state reaction rates

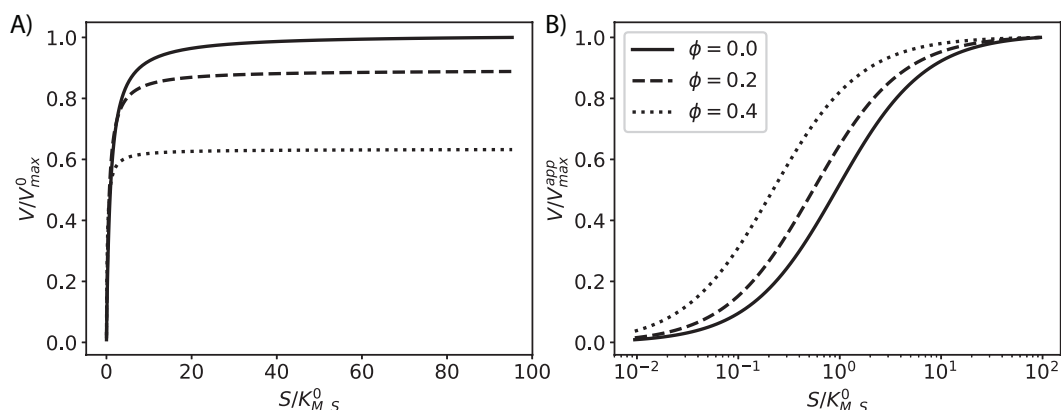


Figure 4.6 – A) Enzyme assay at different volume occupancies,  $\phi_M = 0.0$ , (solid)  $\phi_M = 0.2$  (dashed),  $\phi_M = 0.4$  (dotted), for a reaction controlled enzyme  $d_{E,S \rightarrow ES} = d_{E,P \rightarrow EP} = 10^{-2}$ . B) Enzyme assay in log-lin-scale normalized by the apparent maximal velocity  $V_{max}^{app}$  to illustrate the change of  $K_{M,S}$  in crowded conditions.

calculated based on the dynamic viscosity of water at 25°C, i.e.,  $\eta = 0.7 \text{ Pas}$ . The standard Gibbs free energy of the enzyme reactions is  $\Delta_{S \rightarrow P} G^0 = -1 RT$ , its substrate and product dissociation constants are  $K_{D,E,S \rightarrow ES} = K_{D,E,P \rightarrow EP} = 10 \mu\text{M}$ , its diffusion limitation ratios  $d_{E,S \rightarrow ES} = d_{E,P \rightarrow EP} = 10^{-2}$ , and the rate of the biocatalytic transformation  $k_{ES \rightarrow EP} = 10^3 \text{ s}^{-1}$ .

Inspection of the results of the enzyme assay reveals similar results, as found in chapter 3. We observe a reduction of the  $V_{max}^{app}$  and the  $K_{M,S}$  with increasing macromolecular volume fraction  $\phi_M$ . These results are not surprising as the effective enzyme parameters  $V_{max}^0$  and  $K_{M,S}^0$  are similar to those of the example, phosphoglycerate mutase, used in chapter 3. In the next step, we investigate the sensitivity of the enzymatic reaction regarding its degree of diffusion control by varying the ratios between the reaction rates in contact and the diffusion-limited rates  $d_{E,S \rightarrow ES}$  and  $d_{E,P \rightarrow EP}$ . The smaller these ratios, the less influence has the diffusional transport on the effective association rate, larger ratios suggest that the effective association rate is strongly impacted by the diffusion of two pairs towards each other. To investigate the impact of the diffusion-control on the enzyme parameters we vary the ratios of  $d = d_{E,S \rightarrow ES} = d_{E,P \rightarrow EP}$  with  $d = [10^{-6}, 10^{-2}, 10^0]$  across different macromolecular volume fractions  $\phi = [0.0, 0.1, 0.2, 0.3, 0.4]$  calculating their effective  $V_{max}$  and their effective  $K_{M,S}$  using enzyme assays as shown in figure 4.6. The analysis shows that the model suggests if enzymes are driven towards diffusion limitation, the effect on the maximal velocity is reduced compared to enzymes that are limited by their reaction rate at contact. Comparing the relative change in maximal velocity  $V_{max}/V_{max}^0$  to the relative change of the dissociation constant  $k_{EP \rightarrow E,P}/k_{EP \rightarrow E}^0$ , it is evident that the change of this dissociation rate constant is the driving

factor for the change in maximal velocity when the complementary association is limited by the relative reaction rate constant (Figure 4.7 part A). Interestingly, this effect is not observable for the changes in the relative substrate affinity in the form of the relative change of the Michaelis-Menten parameter  $K_{M,S}/K_{M,S}^0$ . The Michaelis-Menten parameter changes proportional to the effective equilibrium constant of the association reactions and is not affected by the diffusion-controlled ratios (Figure 4.7 part B). To understand why  $V_{max}$  seems to be less affected by macromolecular crowding, we investigate the change of radial distribution function of the associating pairs in contact  $\rho_{E,S}(R_{E,S})/\rho_{E,S}^0(R_{E,S})$  and  $\rho_{E,P}(R_{E,P})/\rho_{E,P}^0(R_{E,P})$  at the highest substrate concentration (Figure 4.7 part C and D). It can be clearly seen that the radial distribution of the product association decreases  $\rho_{E,P}(R_{E,P})/\rho_{E,P}^0(R_{E,P})$  with increasing macromolecular volume fraction. Revisiting equation 4.50, we understand that the effective association rate constant in contact  $k_{E,P \rightarrow EP}^{0,app} = k_{E,P \rightarrow EP}^0 g_{ES}(R_{E,S})$  increases with the radial distribution function in contact, which increases with the volume fraction (see section 4.3.1). In contrast, the diffusion-limited rate constant  $k_{E,P \rightarrow EP}^{sm}$  decreases. This results in an overall reduction of the effective association rate constant if the limited diffusion rate constant  $k_{E,P \rightarrow EP}^{sm}$  is in a similar order of magnitude as the association rate constant in contact  $k_{E,P \rightarrow EP}^{0,app}$ . The reduction of the effective product association increases the net flux, counteracting the limitation by the crowding dependent decrease of the dissociation rate constant.

From the solution of the elementary reaction model, we expect a linear increase in the pair distribution  $\rho_{E,P}$  at the interface with respect to the concentration  $[EP]/[E]/[P]$ . This linear increase is not limited by any interactions taken into account in the model. When assessing this quantity in the enzyme model, we likewise observe an increase of the  $\rho_{E,P}$  as a function of the substrate concentration. If we translate this observation into a conceptual model, this will result in the accumulation of products in the vicinity of an enzyme that can occur without any thermodynamic cost on the dissociation reaction. In reality, this boundary layer of products around the enzymes will increase the activity of the products in that region around enzyme (Figure 4.8), integrating this to the dissociation model discussed in section 4.3.2 results in a decreasing dissociation probability with increasing accumulation of products close to the enzyme. To capture this effect, we introduce a simple model that, in addition to the activity in bulk, accounts for the activity due to the volume occupancy of product molecules at the dissociation radius  $\phi_P(R_{mn})$ .

$$k_{mn \rightarrow l} = k_{mn \rightarrow l}^0 g_{mn}(R_{mn}) \gamma_{mn \rightarrow l} (1 - \phi_P(R_{mn})) \quad (4.57)$$

Note that we choose an underestimating model by the only accounting for the additional



#### 4.5. Non-equilibrium effects on steady-state reaction rates

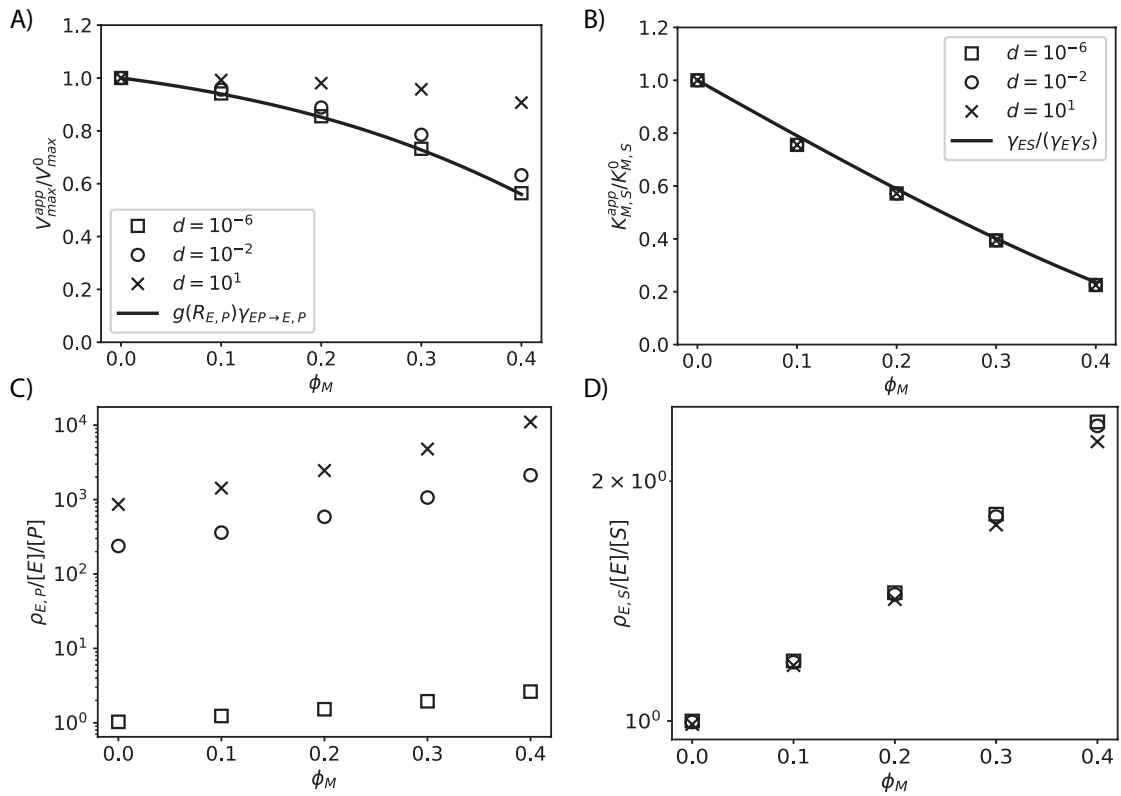


Figure 4.7 – A) Relative change in maximal enzyme rate  $V_{max}/V_{max}^0$  compared to the relative change in dissociation rate constant (solid line) as well as B) relative change of the Michaelis-Menten parameter  $K_{M,S}/K_{M,S}^0$  compared to the change of the equilibrium constant of the association reaction (solid line), C) relative pair distribution function between products and enzymes at highest substrate concentration  $\rho_{E,P}/[E][P]$  and D) relative pair distribution function between substrates and enzymes at highest substrate concentration  $\rho_{E,S}/[E][S]$  as a function of macromolecular volume fraction for enzymes with different diffusion-controlled ratios  $d = 10^{-6}$  (crosses),  $10^{-2}$  (circles),  $10^0$  (squares).

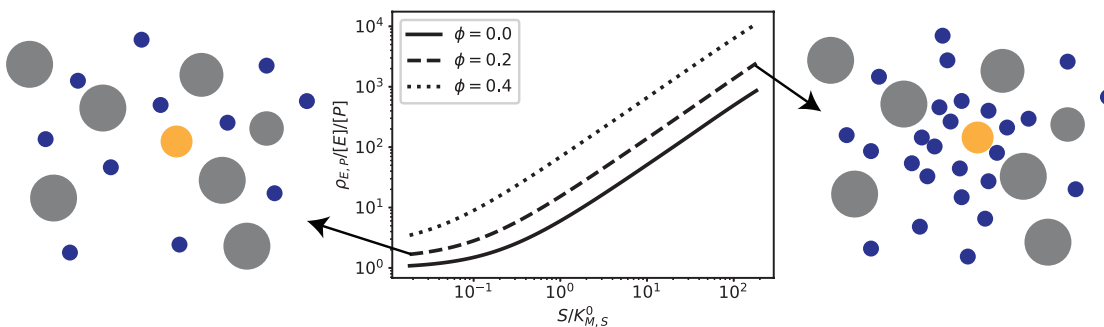


Figure 4.8 – Normalized pair distribution function at the contact radius  $\rho_{E,P}(R_{E,P})/[E][P]$  at steady state as a function the substrate concentration with illustrations of the increasing local concentration of product (blue) around the enzyme (yellow) surrounded by macromolecules (grey).

occupied volume at the contact radius, as we only account for the first term of the excess free-energy given in equation 4.34.

Correcting our diffusion-reaction model for the occupied volume at the contact interface, we repeat measuring the apparent maximal enzyme velocity  $V_{max}^{app}$  and the apparent Michaelis-Menten constant  $K_{M,S}^{app}$ , as a function of the volume fraction occupied by macromolecules  $\phi_M$ . The simulation results reveal that when the product accumulation at the contact interface is taken into account, the apparent maximal enzyme rate  $V_{max}^{app}$  of the diffusion-controlled case with  $d = 10^0$  is less affected by macromolecular crowding (Figure 4.9). In contrast, this correction has no significant effect on the maximal enzyme rate of the reaction controlled cases  $d = 10^{-2}$  and  $d = 10^{-6}$  as well as the apparent Michaelis-Menten constant for all cases. Thus, indicating that for the diffusion-controlled case  $d = 10^0$ , the reduction of the dissociation constant, due to the direct effect of crowding and the accumulation of products at the enzyme-product interface, is not limiting the maximal enzyme rate.

## 4.6 Discussion

The effect of diffusion and crowding on the effective reaction kinetics is a highly disputed topic (Grima and Schnell, 2006a,b). Most studies focused their efforts on the time-dependent reaction rate constants and discovered different forms of anomalies (Mourao et al., 2014; Szabo, 1989; Gopich and Szabo, 2002, 2018). Other studies also include crowding effects in closed systems (Smith and Grima, 2017; Cianci et al., 2017). In this chapter, we extend the model developed by Gopich and Szabo (2018) to expose, for the first time, the effective steady-state kinetics in an open system displaced from equilibrium. We also develop a nu-

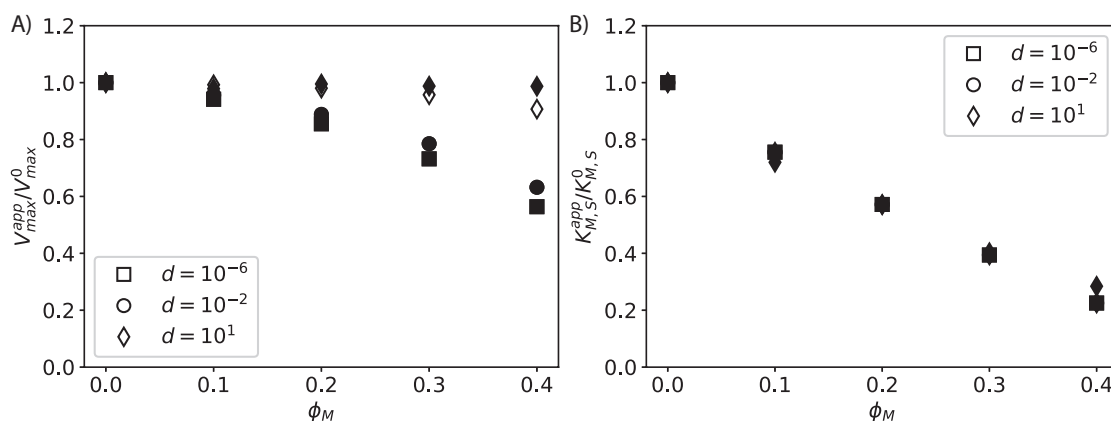


Figure 4.9 – Comparing the A) maximal enzyme rate  $V_{max}/V_{max}^0$  and B) relative change of the Michaelis-Menten parameter  $K_{M,S}/K_{M,S}^0$  as a function of macromolecular volume fraction for enzymes with different diffusion-controlled ratios  $d = 10^{-6}$  (diamonds),  $10^{-2}$  (circles),  $10^0$  (squares) between the original model (empty symbols) and the model corrected for product accumulation in proximity to the enzyme (filled symbols).

merical formulation to solve the non-linear equation that has so far only been solved for kinetics linearized around the thermodynamic equilibrium. Using models for thermodynamic quantities as the excess free energy and the equilibrium pair-distribution as well as models for the effective diffusion, we extend the models further to account for the average kinetics in a crowded environment.

Although the analysis presented in this chapter focuses solely on the steady-state reaction kinetics, the mathematical and numerical formulation of the problem also allows investigating dynamic transition paths from one steady-state to another. Gopich and Szabo (2018) presented an analysis of such transition paths for relaxation to equilibrium. In their analysis, they show that the effective rate constants change as a function of time as the pair distribution function of reactants in proximity is time-dependent for diffusion-controlled situations. Their analysis hints that these effects may also occur in non-equilibrium systems that move from one steady-state to another. Such a change in the steady-state can be caused by changes in the environment of the system, e.g., when the concentration of nutrients around the cell changes. We thus suggest that future work should also investigate the time course behavior between non-equilibrium states.



## 5 Crowded metabolic control

### 5.1 Introduction

In the previous chapters 3 and 4, we focus on the investigation of the behavior of individual enzymes in a crowded environment. In this chapter, we aim to extend the analysis to small prototypical metabolic networks and to provide a framework that enables studying the responses of metabolic reaction networks to genetic and environmental changes.

Metabolic networks are descriptions of the cellular metabolism in the form of a reaction network that connects the individual metabolites via biochemical transformations catalyzed by enzymatic reactions. Based on such a network description, the mass balances of the metabolites in the network can be deduced. The solution space of these mass-balances can, in the absence of knowledge on the reaction rate law, be studied by constraint-based modeling under the assumption the reactions network is in a quasi-steady-state (Vallino and Stephanopoulos, 1993; Varma and Palsson, 1993a,b; Orth et al., 2010). Constraint-based modeling methods have evolved to include a variety of different aspects such as thermodynamics (Henry et al., 2005, 2007), proteome limitations (Sánchez et al., 2017), as well as transcription and translation (Salvy and Hatzimanikatis, 2020), where the two latter methods require knowledge of the maximal kinetic rate in the form of the catalytic rate constant. Nevertheless, all these methods allow only to characterize the solution space of the reaction rates given the modeled constraints. To additionally constraint the possible solution space, these methods consider an objective function that is to be optimized, e.g., the maximal production of biomass. Under the assumption of optimality, the solution space for the reaction rates and other variables is then further reduced. This, however, does not allow to account for non-optimal responses, as the resulting solution space for a perturbation in the environment will still be the solution

space subject to the optimality assumption. Further, the solution spaces before and after the perturbation can overlap, leading to inconclusive results. Describing the flux and concentration responses of a biochemical network requires the information on the reaction rate laws of the enzymatic reaction or at least their sensitivities for changes in the concentrations and biochemical parameters.

In this chapter, we make use of metabolic control analysis (MCA), a framework initially developed to study the sensitivity of metabolic networks for environmental changes (Kacser and Burns, 1973). MCA provides the means to study the steady-state and dynamic responses of concentrations and fluxes within metabolic networks, provoked by changes in the enzyme activities, extracellular concentrations, or other system parameters Kacser and Burns (1973); Heinrich and Rapoport (1974); Reder (1988); Hatzimanikatis and Bailey (1996, 1997). The framework has since been used to address various questions in fundamental biology, biotechnology, biophysics, and medicine Kholodenko and Westerhoff (1993); Schuster (1999); Cascante et al. (2002); Wang et al. (2004); Wang and Hatzimanikatis (2006b,a); Tokic et al. (2020).

We use the MCA framework in combination with the approximate crowded kinetics (GEEK) introduced in chapter 3 to calculate the local and global sensitivities of the enzymatic reaction rates for changes in the enzyme activities in small prototypical reaction networks. Our analysis reveals that substrate sizes, as well as the limitation by diffusion, are key factors that change these sensitivities significantly when considering crowded conditions. This work suggests that applying this framework to larger metabolic networks may yield new insights into cellular responses to extreme changes in the environment.

## 5.2 Modeling perturbations in metabolic networks

### 5.2.1 Metabolic kinetic models

In this chapter, we consider a metabolic reaction network consisting out of  $M$  enzymatic reactions that involve  $N$  metabolites. The dynamics of this system is given by the mass-balance for each of the metabolites:

$$\frac{d\mathbf{x}}{dt} = S\mathbf{v}(\mathbf{x}, \mathbf{p}) \quad (5.1)$$

where  $\mathbf{v} \in \mathcal{R}^M$  is a function that describes the reaction rate of each enzymatic reaction as a function of the metabolite concentrations  $\mathbf{x} \in \mathcal{R}^N$  and a set of parameters  $\mathbf{p} \in \mathcal{R}^U$ . The rate of

## 5.2. Modeling perturbations in metabolic networks

accumulation of every metabolite is then given by the scalar product of the stoichiometric matrix  $S \in \mathcal{R}^{M \times N}$  with the reaction rate vector  $\mathbf{v}$ . Such metabolic network models can include conservation constraints. Such constraints emerge when the total amount of a group of compounds is constant over the characteristic response time of the model. To consider these conservation constraints, an additional set of parameters  $\mathbf{p}_c \in \mathcal{R}^{U_c}$  is introduced, representing the total concentration of the conserved moieties. Given the total concentration of a conserved moiety, one metabolite concentration can be expressed as a function of the other metabolite concentrations. Subsequently, the set of metabolites is split into a subset of dependent metabolites  $\mathbf{x}^d \in \mathcal{R}^{U_c}$  and a subset of independent metabolites  $\mathbf{x}^i \in \mathcal{R}^{N-U_c}$ . All dependent metabolites are then a function of the independent metabolites and the total concentration parameters  $\mathbf{x}^d(\mathbf{x}^i, \mathbf{p}_c)$ . The conservation constraints introduce linearly dependent rows in the stoichiometric matrix  $S$ , resulting in a rank deficient matrix. These linearly dependent rows can be extracted to form a new stoichiometric matrix  $S_R$  (Reder, 1988; Heinrich and Schuster, 1996; Wang et al., 2004). Reformulation of the kinetic rate laws considering the above-mentioned linear constraints gives then a reduced set of balance equations for the model:

$$\frac{d\mathbf{x}^i}{dt} = S\mathbf{v}(\mathbf{x}^i, \mathbf{x}^d(\mathbf{x}^i, \mathbf{p}_c), \mathbf{p}) \quad (5.2)$$

### 5.2.2 (Log)linear formulation of Metabolic Control Analysis

To analyze flux and concentration responses with respect to parameter perturbations Kacser and Burns introduced the flux and concentration control coefficients  $C_p^v$  and  $C_p^x$ , respectively. These control coefficients are defined as the fractional change of metabolite concentration and fluxes over the fractional change of the system parameters (Kacser and Burns, 1973). With the help of the (log)linear formalism (Hatzimanikatis and Bailey, 1996, 1997; Reder, 1988) the system (Equation 5.2) can be linearized and scaled around steady state, allowing to derive expressions for the control coefficients (Wang et al., 2004):

$$C_p^x = -(S_R V (\Xi_i + Q_i^d \Xi_d))^{-1} (S_R V \Pi) \quad (5.3)$$

$$C_p^v = (\Xi_i + Q_i^d \Xi_d) C_p^x + \Pi \quad (5.4)$$

where  $V$  a square diagonal matrix of the fluxes,  $\Xi_i$  denotes the fractional changes of the net fluxes with respect to the fractional changes of the independent concentrations,  $\Xi_d$  denotes the fractional changes of the net fluxes with respect to the fractional changes of the dependent

concentrations,  $Q_i^d$  are the weights of the linear conservation constraints of the dependent metabolites and  $\Pi$  are the fractional changes of fluxes with respect to the fractional change in a parameter  $p$ .

## 5.3 Introducing crowding into metabolic reaction networks

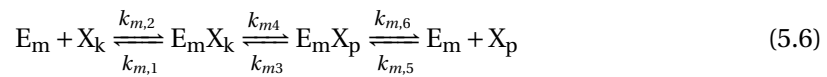
### 5.3.1 Generalized elementary enzyme model

In the next step, we aim to integrate a model of the response to a change of the environment into the metabolic control framework. Therefore we use the generalized elementary kinetics (GEEK) as presented in chapter 3. GEEK allows capturing the effective kinetics in a crowded environment. This kinetic rate is a modified mass action law where the effective reaction rate constant is expressed as a power-law of the scaled concentrations in the system. The expression of the rate constants is given as

$$k_j = k_j^0 e^{\beta_j} \prod_i \left( \frac{[X_i]}{[X_i^0]} \right)^{\alpha_{i,j}} \quad (5.5)$$

where  $\exp(\beta_j)$  characterizes the relative change of reaction rate constants at the reference concentration, and the  $\alpha_{i,j}$  are the exponents of the scaled concentrations. In contrast to the generalized mass action (Smith, 1992), GEEK is expressed in terms of the elementary reactions and as a function of all concentrations in the system rather than only the reactant concentrations. GEEK is a phenomenological description that can be directly characterized by rate constants measurement at constant concentrations using weighted log-linear regression.

To derive a formalism that allows considering spatial effects in the metabolic control analysis, we consider that each enzyme  $E_m$  catalyzing a reaction transforming the metabolite  $X_k$  into the metabolite  $X_p$  follows a three-step Michaelis-Menten mechanism



To account for deviations of the mass-action mechanism in crowded conditions, we introduce the generalized elementary kinetics (GEEK) to describe the kinetics each elementary step  $(m, i)$  with  $m \in M$  and  $i \in [1, 6]$ . Thus the reaction rate constant of each elementary step is

$$k_{m,i} = k_{m,i}^0 e^{\beta_{m,i}} \prod_{k \in \mathcal{X}} \left( \frac{[X_k]}{[X_k^0]} \right)^{\alpha_{m,i,k}} \prod_{e \in \mathcal{E}} \left( \frac{[E_j]}{[E_j^0]} \right)^{\alpha_{m,i,j}} \prod_{c \in \mathcal{C}} \left( \frac{[EX_c]}{[EX_c^0]} \right)^{\alpha_{m,i,c}} \quad (5.7)$$



### 5.3. Introducing crowding into metabolic reaction networks

Table 5.1 – Mass-action terms for the three step Michaelis-Menten mechanism

$\theta_{m,1}$	$\theta_{m,2}$	$\theta_{m,3}$	$\theta_{m,4}$	$\theta_{m,5}$	$\theta_{m,6}$
$[X_k][E_m]$	$[E_m X_k]$	$[E_m X_p]$	$[E_m X_k]$	$[E_m X_p]$	$[X_p][E_m]$

where  $\mathcal{X}$  is the set of metabolites in the metabolic network,  $\mathcal{E}$  is the set of free enzymes in the network  $\mathcal{C}$  denotes the set of existing enzyme complexes in the network. For a metabolic network consisting only of three-step Michaelis-Menten mechanisms  $\mathcal{X}$  has the size  $N$ ,  $\mathcal{E}$  has the size  $M$ , and  $\mathcal{C}$  is of size  $2M$ . The GEEK rate constants the reaction rate of the elementary reactions can be then written in the form of

$$v_{m,i} = k_{m,i}\theta_{m,i} \quad (5.8)$$

where  $\theta_{i,j}$  denote the mass-action term of respective elementary reaction. The mass action terms for the elementary reaction of the three-step mechanism given above are denoted in table 5.1.

The translation and degradation of proteins occur on a much slower timescale than the turn over of metabolic reactions as extensively reviewed in the supplemental material of (Salvy and Hatzimanikatis, 2020). We, therefore, assume that the overall amount of the enzyme  $E_m$  is conserved. Thus the total amount of enzyme  $[E_{m,T}]$  constraints the number of free enzymes and enzyme complexes linearly:

$$[E_{m,T}] = [E_m] + [E_m X_k] + [E_m X_p] \quad (5.9)$$

Each of these enzyme conservation relations reduces the effective degrees of freedom for each enzyme by one. Thus, one of the enzyme species has to be part of the set of dependent species. For every enzyme conservation relation, the free enzyme is chosen to be the dependent species. Thus the enzyme complexes are within the set of independent species.

$$[E_m] = [E_{m,T}] - [E_m X_k] - [E_m X_p] \quad (5.10)$$

At this point, we introduce another useful quantity, the enzyme saturation  $\sigma_m$ . The saturation  $\sigma_m$  denotes the fraction of bound enzyme. Given the conservation relation above the enzyme saturation can be expressed as

$$\sigma_m = \frac{[E_m X_k] + [E_m X_p]}{[E_{m,T}]} = 1 - \frac{[E_m]}{[E_{m,T}]} \quad (5.11)$$

### 5.3.2 An approximate model for crowded elementary reactions

In chapter 3, we investigate how the elementary kinetics of the Michaelis-Menten mechanism is altered under crowded, non-equilibrium conditions. We could show that the power-law formalism of GEEK can be used to approximate the steady-state reaction rates. Further, we show that the exponents are significantly deviating from zero when diffusion becomes a limiting factor in association reactions. In the following chapter 4, we find that isolated diffusion-controlled association reactions like the association of the substrate to an enzyme, when driven out of equilibrium towards the dissociated state, show an increased apparent reaction rate constant. From solving the pair-wise Smoluchowski equation, it can be shown that this increase is proportional to the ratio of products and educts of the association reaction. The results suggest that diffusion inhibits the separation of the products leading to an increased pair distribution at the contact, which appears as an increased association rate constant. This accumulation can then lead to an inhibition of the dissociation rate in case the available volume at the contact radius of the dissociated molecules approaches zero (Chapter 4).

In the above denoted enzyme model, equation 5.6, we find two association reactions, i.e.  $(m, 1)$  and  $(m, 6)$  with their respective dissociation reactions  $(m, 2)$  and  $(m, 5)$  and one single reversible unimolecular reaction modeling the biochemical transformation  $(m, 3)$  and  $(m, 4)$ . Choosing a set of reference concentrations allows us to approximate the effective kinetic rate constants using GEEK. Due to its power-law nature, the GEEK parameters can be directly calculated as:

$$\alpha_{i,j} = \left. \frac{\partial \ln(k_j/k_j^0)}{\partial \ln([C_j]/[C_j]_0)} \right|_{[C_j]_0} \quad (5.12)$$

$$\beta_j = \ln \left( \frac{k_j}{k_j^0} \right) \Bigg|_{[C_j]_0} \quad (5.13)$$

for every irreversible elementary rate constant  $k_j$  and component of the system  $C_j$ .

If the enzyme operates in the forward directionality, i.e., producing a netflux of products  $X_p$ , the reaction pair  $(m, 1), (m, 2)$  is driven towards the association of the substrate  $X_k$  and the reaction pair  $(m, 5), (m, 6)$  is driven towards the dissociation of the products  $X_p$ .

Using the theoretical model, presented in chapter 4, we calculate the change in effective reaction rate constants around a set of reference concentrations, we then estimate  $\alpha_{i,j}$  and  $\beta_j$  for the elementary reactions  $i = [(m, 1), (m, 2), (m, 5), (m, 6)]$  of the enzymes in the network. For the elementary reactions of the biotransformation  $i = [(m, 3), (m, 4)]$  the model theoretical

### 5.3. Introducing crowding into metabolic reaction networks

---

reaction-diffusion model assumes that the effective rate constants do not change due to crowding thus  $\alpha_{m,3,j} = \alpha_{m,4,j} = 0$  for  $j \in \{\mathcal{X}, \mathcal{C}, \mathcal{E}\}$  as well as  $\beta_{m,3} = \beta_{m,4} = 0$ . To calculate the remaining local concentration and parameter sensitivities for crowded and non-crowded conditions we first use the theoretical reaction-diffusion model to calculate a reference steady-state  $X_0$  for a given substrate and product concentration, here  $[S] = K_{M,S}$  and  $[P] = 0.1 K_{M,P}$ . We then vary the individual concentrations of all the species (Figure 5.1) and finally estimate the sensitivity  $\alpha_{m,i,j}$  of the elementary rate constants with respect to the concentrations of the species at the reference concentration. To calculate the GEEK parameters, we use two different enzyme models from the previous chapter, i) the diffusion-controlled enzyme with where the ratio between the contact and diffusion-limited reaction rate constants is  $d = 10^0$  and ii) the reaction controlled enzyme where this ratio is  $d = 10^{-2}$ . The parameters for the GEEK approximation are obtained via the slope and the offset at  $[C]/[C]_0 = 1$  in a double logarithmic plot of relative changes of the reaction rate constants  $k_j^{eff}/k_j^0$  as a function of the relative change in the species concentrations  $[S]/[S]_0$ ,  $[E]/[E]_0$ ,  $[ES]/[ES]_0$ ,  $[EP]/[EP]_0$ ,  $[P]/[P]_0$  (Table 5.2).

The results show clearly that in a reaction controlled situation  $d = 10^{-2}$ , the concentration dependency vanishes. In this case, all logarithmic sensitivities  $\alpha_{i,j}$  approach zero for all concentrations. In contrast, we find that for diffusion-controlled  $d = 10^0$  situations, some of the logarithmic sensitivities significantly deviate from zero. In agreement with the analytical results from the non-equilibrium association-dissociation system, we find that only the association reaction rate constant is sensitive to a change of the concentration of its educts and products. Where increasing the respective dissociated products,  $[E]$  and  $[P]$  or  $[E]$  and  $[S]$ , leads to a reduction of the rate constant, and an increase of the respective complex,  $[ES]$  or  $[EP]$ , results in an increased association constant. As discussed in the previous chapter, this again illustrates that the law of mass action for chemical reaction kinetics does not even hold in dilute conditions if the reaction is reversible and operates far away from equilibrium. Introducing macromolecule into the system changes the reference conditions primarily, as with the same product and substrate concentration, the system is driven towards an associated state. As an effect, the macromolecular crowding alters the local logarithmic sensitivities of the association reactions for the diffusion-controlled case.

## Chapter 5. Crowded metabolic control

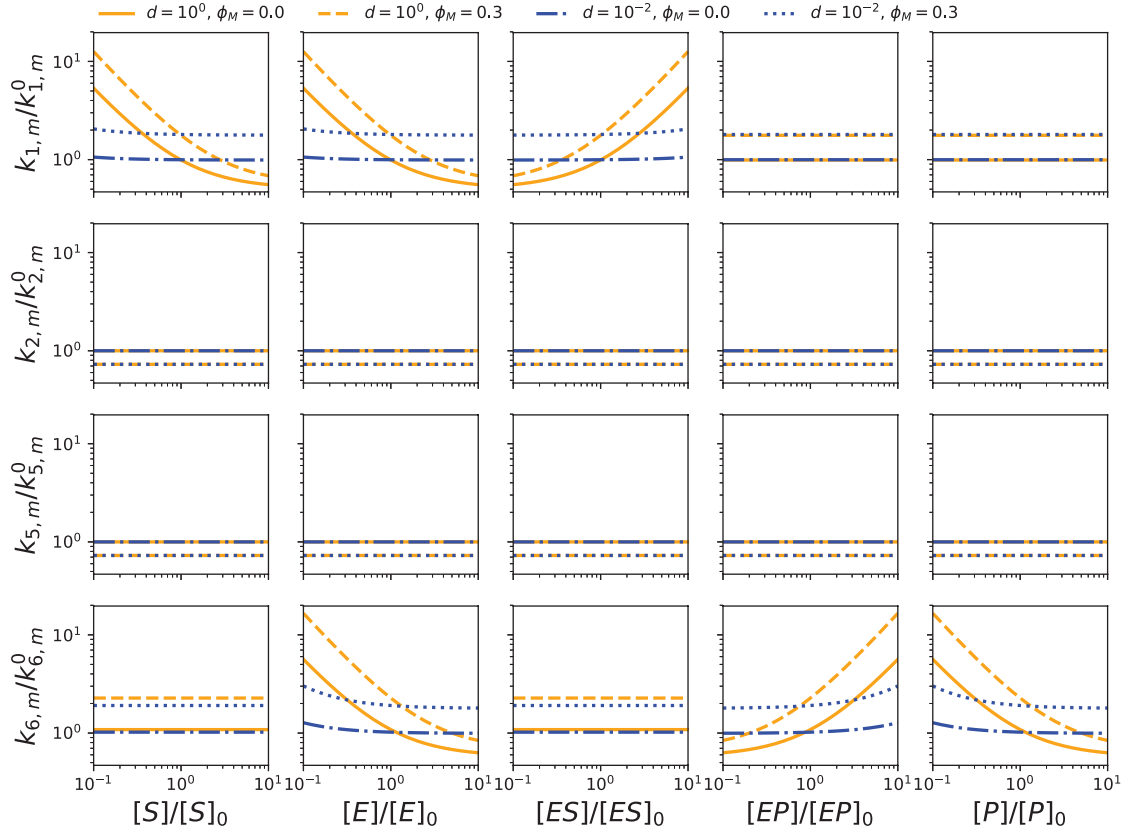


Figure 5.1 – Double logarithmic plot of the relative change of the effective reaction rate constants with respect to the dilute rate constant for the substrate association and dissociation reactions ( $m, 1$ ), ( $m, 2$ ) as well as the product dissociation and association reaction ( $m, 5$ ), ( $m, 6$ ) as a function of the enzyme species concentrations calculated using the theoretical reaction-diffusion model presented in chapter 4.

Table 5.2 – Logarithmic sensitivities  $\alpha_{m,i,j}$  for the association rate constants  $i \in [1, 6]$  in dilute and crowded  $\phi_M = 0.3$  conditions for diffusion controlled and reaction controlled enzymes.

$d$	$10^0$	$10^0$	$10^{-2}$	$10^{-2}$
$\phi_M$	0.0	0.3	0.0	0.3
$\alpha_{m,1,S}$	-0.52	-0.71	-0.01	-0.03
$\alpha_{m,1,E}$	-0.52	-0.71	-0.01	-0.03
$\alpha_{m,1,ES}$	0.46	0.66	0.01	0.02
$\alpha_{m,6,P}$	0.39	0.60	0.01	0.01
$\alpha_{m,6,E}$	-0.45	-0.65	-0.01	-0.02
$\alpha_{m,6,EP}$	-0.45	-0.65	-0.01	-0.02

### 5.3. Introducing crowding into metabolic reaction networks

Table 5.3 – Concentration elasticities of the elementary reactions for a three-step Michaelis-Menten mechanism, as denoted in equation 5.6, with  $[X_l]$  denoting all species of the system that are not involved in the enzyme mechanism

$i$	1	2	3	4	5	6
$\frac{d \ln v_{m,i}}{d \ln [X_k]}$	$\alpha_{m,1,k} + 1$	$\alpha_{m,2,k}$	$\alpha_{m,3,k}$	$\alpha_{m,4,k}$	$\alpha_{m,5,k}$	$\alpha_{m,6,k}$
$\frac{d \ln v_{m,i}}{d \ln [X_p]}$	$\alpha_{m,1,p}$	$\alpha_{m,2,p}$	$\alpha_{m,3,p}$	$\alpha_{m,4,p}$	$\alpha_{m,5,p}$	$\alpha_{m,6,p} + 1$
$\frac{d \ln v_{m,i}}{d \ln [E_j X_k]}$	$\alpha_{m,1,j,k}$	$\alpha_{m,2,j,k} + 1$	$\alpha_{m,3,j,k} + 1$	$\alpha_{m,4,j,k}$	$\alpha_{m,5,j,k}$	$\alpha_{m,6,j,k}$
$\frac{d \ln v_{m,i}}{d \ln [E_j X_p]}$	$\alpha_{m,1,j,p}$	$\alpha_{m,2,j,p}$	$\alpha_{m,3,j,p}$	$\alpha_{m,4,j,p} + 1$	$\alpha_{m,5,j,p} + 1$	$\alpha_{m,6,j,p}$
$\frac{d \ln v_{m,i}}{d \ln [E_j]}$	$\alpha_{m,1,j} + 1$	$\alpha_{m,2,j}$	$\alpha_{m,3,j}$	$\alpha_{m,4,j}$	$\alpha_{m,5,j}$	$\alpha_{m,6,j} + 1$
$\frac{d \ln v_{m,i}}{d \ln [X_l]}$	$\alpha_{m,1,l}$	$\alpha_{m,2,l}$	$\alpha_{m,3,l}$	$\alpha_{m,4,l}$	$\alpha_{m,5,l}$	$\alpha_{m,6,l}$

#### 5.3.3 Generalized enzyme elasticities

Following the (log)linear formalism introduced above we introduce the concentration and parameter elasticity matrix of the elementary-network:

$$\Xi = \left\{ (m, i), j \left| \varepsilon_j^{m,i} = \frac{\partial \ln v_{m,i}}{\partial \ln x_j} \right. \right\} \quad (5.14)$$

$$\Pi = \left\{ (m, i), j \left| \pi_j^{m,i} = \frac{\partial \ln v_{m,i}}{\partial \ln p_j} \right. \right\} \quad (5.15)$$

where  $x_j \in \{\mathcal{X}, \mathcal{E}\}$  and parameters  $p_j$  are the total enzyme concentrations  $[E_{m,T}]$  and  $(m, i)$  denote the elementary reactions  $i$  of each enzymatic reaction  $m$ . From equations 5.7 and 5.8 it can be derived that the concentration elasticities of the generalized elementary kinetics can be separated into a mass action contribution that is either one or zero and a non-ideal contribution from the partial derivative of the GEEK rate constant.

$$\varepsilon_j^{m,i} = \frac{x_j}{k_{m,i}} \frac{\partial k_{m,i}}{\partial x_j} + \frac{x_j}{\theta_{m,i}} \frac{\partial \theta_{m,i}}{\partial x_j} \quad (5.16)$$

Calculating the respective elementary concentration elasticities based on an elementary reaction network that follows the Michaelis-Menten scheme denoted in equation 5.6 yields the results shown in table 5.3.

Due to the formulation in terms of elementary steps, the elasticity with respect to total enzyme concentration is an elasticity for a conserved pool. We calculate the elementary parameter elasticity by expressing the free enzyme concentrations in terms of the independent complex concentrations (Equation 5.10). We then substitute the free enzyme concentration with these expressions and calculate the parameter elasticity via the scaled partial derivative with respect

Table 5.4 – Elementary parameter elasticities with respect to the total enzyme concentration.

$i$	1	2	3	4	5	6
$\frac{d \ln v_{m,i}}{d \ln [E_{m,T}]}$	$\frac{\alpha_{m,1,m}+1}{1-\sigma}$	$\frac{\alpha_{m,2,m}}{1-\sigma}$	$\frac{\alpha_{m,3,m}}{1-\sigma}$	$\frac{\alpha_{m,4,m}}{1-\sigma}$	$\frac{\alpha_{m,5,m}}{1-\sigma}$	$\frac{\alpha_{m,6,m}+1}{1-\sigma}$

to the total enzyme concentration  $[E_{m,T}]$ . For practical purposes, the results are expressed in terms of the enzyme saturation  $\sigma$ , see table 5.4.

In the next step, we compute the effective elementary flux elasticities  $\Xi$ :

$$\Xi = \Xi_i + \Xi_d Q_i^d \quad (5.17)$$

where  $\Xi^i$  denotes the concentration elasticities of the independent species  $\Xi^d$  the concentration elasticities of the dependent species, and  $Q_i^d$  are the relative weights derived from the conservation relations:

$$Q_i^d = \left\{ d, i \mid q_i^d = \frac{\partial \ln x_d}{\partial \ln x_i} \right\} \quad (5.18)$$

with  $x_i \in \{X^i, C\}$  and  $x_d \in \{X^d, E\}$ . From the enzyme conservation relation (Equation 5.10) we find the relative weights with respect for the substrate and product complex as:

$$\frac{\partial \ln [E_m]}{\partial \ln [E_m X_k]} = - \frac{[E_m X_k]}{[E_m, T] - [E_m X_p] - [E_m X_k]} \quad (5.19)$$

$$\frac{\partial \ln [E_m]}{\partial \ln [E_m X_p]} = - \frac{[E_m X_p]}{[E_m, T] - [E_m X_p] - [E_m X_k]} \quad (5.20)$$

Using the above-described matrices, we can calculate the concentration control coefficients as well as the flux control coefficients for the elementary reactions for an isolated enzyme mechanism:

$$C_p^X = -(M_R V (\Xi_i + Q_i^d \Xi_d))^{-1} (M_R V \Pi) + \Pi \quad (5.21)$$

$$C_p^{v_i} = -(\Xi_i + Q_i^d \Xi_d) L_p^X + \Pi \quad (5.22)$$

where  $M_R$  is the reduced stoichiometric matrix of the mechanism, and  $V$  is diagonal a matrix containing the elementary fluxes. We then introduce the thermodynamic displacement  $\gamma^n = v_b^n / v_f^n$  of the net elementary reactions as it allows us to express  $V$  in terms of the net flux of the enzyme and the displacements of the three reversible reactions.

Using the definition of  $\gamma$  and the knowledge that  $v_n = v_f - v_b$  it can be shown the local control coefficients can be rewritten as a weighted sum of the elementary forward and backward elasticity (Wang et al., 2004; Miskovic et al., 2019). We, therefore, introduce  $G$  containing the

### 5.3. Introducing crowding into metabolic reaction networks

weights for a change of the respective forward or backward flux affects the net flux:

$$G = \left\{ n, i \mid g_i^n = \frac{\partial \ln v_n}{\partial \ln v_i} \right\} \quad (5.23)$$

where  $v_n$  are the elementary net fluxes,  $v_i$  are the elementary fluxes. The elements of the matrix are

$$g_i^n = \frac{1}{1 - \gamma_n} \quad \text{if } i \in \text{forward reaction of } n \quad (5.24)$$

$$g_i^n = -\frac{\gamma_n}{1 - \gamma_n} \quad \text{if } i \in \text{reverse reaction of } n \quad (5.25)$$

$$g_i^n = 0 \quad \text{else} \quad (5.26)$$

With this, the net flux control coefficients can be calculated as follows:

$$C_p^{v_n} = G C_p^{v_i} \quad (5.27)$$

These local control coefficients can be interpreted, the effective parameter elasticities of the enzyme within a network (Miskovic et al., 2019). Treating the substrate and product concentrations as locally constant, we calculate the effective concentration elasticities in the exact same fashion as the parameter sensitivity. To calculate the local concentration and parameter sensitivities crowded and non-crowded conditions we use the theoretical model to calculate a reference steady-state  $x_0 = [[S], [E], [ES], [EP], [P]]$  for a given substrate and product concentration, here  $[S] = K_{M,S}$  and  $[P] = 0.1K_{M,P}$ . We then vary the individual concentrations of all the species to calculate the GEEK parameters of the elementary rate constants as described above (Figure 5.1). From the reference steady state of the enzyme, we are further able to extract the enzyme saturation  $\sigma$  and the thermodynamic displacements  $\gamma_m$  for crowded and non-crowded conditions. Finally, we use the enzyme parameters  $\alpha_{m,i,j}$ , the enzyme saturation  $\sigma$ , and the thermodynamic displacements  $\gamma_m$  to populate the flux and elasticity matrices to then calculate the effective elasticities with respect to substrate concentration, product concentration, and total enzyme concentration.

We calculate these local control coefficients for a diffusion-controlled and a reaction controlled scenario and compare their results to the control coefficients for the respective mass-action system (See Figure 5.2). The results show again that for diffusion-controlled enzymes, the parameters and concentration elasticities calculated with mass-action kinetics significantly deviate from the generalized elementary kinetics approximation. In contrast, the dilute reac-

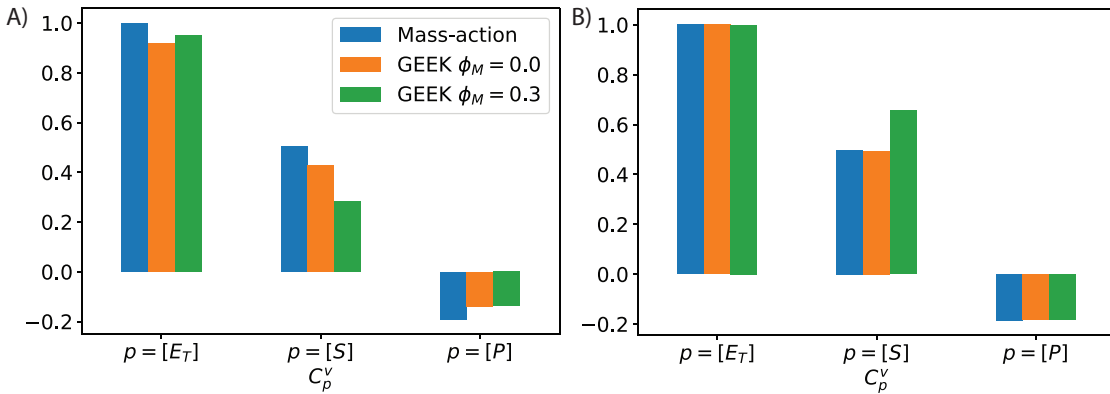


Figure 5.2 – Enzyme flux elasticities with respect to substrate, product and total enzyme concentrations calculated with mass-action kinetics (blue), dilute (orange) and crowded (green) ( $\phi_M = 0.3$ ) GEEK for A) diffusion controlled enzyme  $d = 10^0$  and B) a reaction controlled enzyme  $d = 10^{-2}$ .

tion controlled case is well approximated based on the mass action kinetics. The deviation for the diffusion-controlled case originates from the fact that even in dilute conditions, diffusion-controlled enzymes do not follow mass action kinetics in the association rate. The GEEK elasticities suggest that crowding can have adverse effects on the elasticities as we see an increase of the substrate elasticity with crowding for the reaction-controlled case  $d = 10^{-2}$  and decrease for the diffusion-controlled case. Nevertheless, we refrain from a general statement as the effect on the local elasticity is subject to various impact factors. From the discussion, in the previous chapter, we already know that for crowded conditions, the apparent Michaelis-Menten constants are reduced according to the difference in excess free energy between educts and products of the dissociation reaction. This increase in affinity leads to i) an increase in the saturation of the enzyme and ii) to a shift of the displacement towards the association of the free species [E], [S], [P] into the complexes [ES], [EP], translating to a decrease of  $\gamma_{m,1}$  and increase of  $\gamma_{m,3}$ . Additionally, we know from table 5.2, that the logarithmic rate constant sensitivities  $\alpha_{m,i,j}$  change to exhibit a stronger effect in crowded conditions. All these effects appear collectively and cause the parameter and concentration elasticities to change in a non-linear fashion. Therefore, the changes in elasticities are particularly case-specific.

## 5.4 Crowded control on prototypical networks

So far, we demonstrated how the effective enzyme sensitivities change for an isolated enzyme when considering dilute or crowded kinetics. In the next step, we apply the same methods on two prototypical networks: i) a linear pathway with three enzymes and ii) branched pathway



Table 5.5 – Enzyme parameters for the linear pathway

Enzyme $m$	$\Delta_{X_k \rightarrow X_p} G$ $RT$	$K_{D, X_k, E_m \rightarrow E_m X_k}$ [M]	$K_{D, X_p, E_m \rightarrow E_m X_p}$ [M]	$k_{ES \rightarrow EP}$ [s <sup>-1</sup> ]
1	-3	$10^{-3}$	$10^{-2}$	$10^3$
2	-2	$10^{-2.5}$	$10^{-1.5}$	$10^3$
3	-1	$10^{-2}$	$10^{-1}$	$10^3$

with three enzymes. Aim of these case studies is to compare the flux control coefficients between dilute and crowded conditions. We, consequently, calculate the control coefficients for the total enzyme concentration, as described in the previous section considering the elementary network of the respective pathway. The enzymes for these pathways are designed using the parametrization equations from section 4.5.2 in the previous chapter.

#### 5.4.1 Linear pathway

The first case study for the linear pathway is designed as a pathway where the biochemical reactions catalyze a substrate  $X_1$  to a substrate  $X_4$  with reduced volume. Each enzyme changes the substrate to a product with 10% less volume starting with  $r_{X_1} = 1$  nm. To calculate the radius of the subsequent substrate  $X_2$ ,  $X_3$ , and  $X_4$ , we assume that the reduced volume is homogenously distributed on a sphere.

Enzymes and enzyme-complexes are considered to have the same size  $R_E = 3$  nm. The enzymes in the pathway further increase in free energy and a decrease in their dissociation constants. We also create two variants of this pathway, one where all association reactions are diffusion-controlled  $d = 10^0$ , and one where all association reactions are reaction-controlled  $d = 10^{-1}$ . The parameters of the three enzymes are summarized in table 5.5.

To calculate the control coefficients we first use the theoretical model to obtain a reference steady-state here for all substrate, enzymes and enzyme complexes for a given concentration of  $X_1 = 10^{-1} K_{M,S}^{E_1}$  and  $X_4 = 10^{-3} K_{M,S}^{E_1}$ . We then use the GEEK assay to determine the local logarithmic sensitivities of each concentration on each irreversible elementary reaction  $m, i$  in the network. From the reference steady state of the network, we are further able to extract the enzyme saturations  $\sigma_m$  and the thermodynamic displacements  $\gamma_m$ . Finally, we use the enzyme parameters  $\alpha_{m,i,j}$ , the enzyme saturation  $\sigma$ , and the thermodynamic displacements  $\gamma_m$  to populate the flux and elasticity matrices to then calculate controll coefficients with respect total enzyme concentrations  $[E_{1,T}]$ ,  $[E_{2,T}]$  and  $[E_{3,T}]$  (Figure 5.3).

The results show that for the dilute reaction controlled case, the last enzyme appears to be

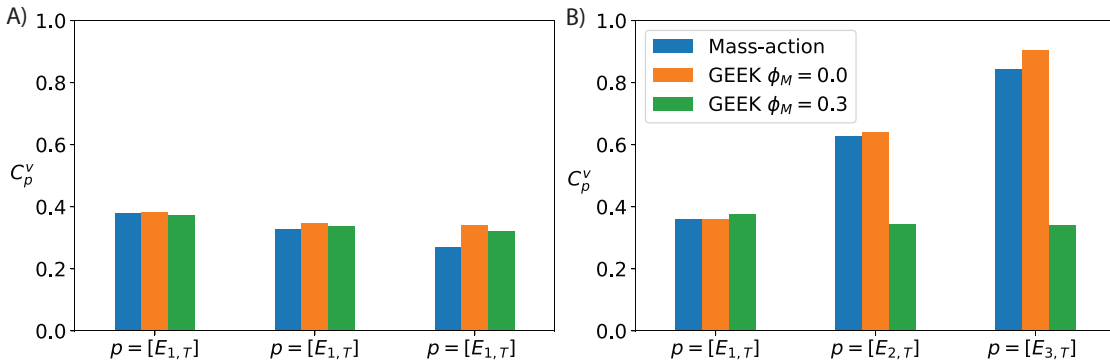


Figure 5.3 – Control coefficients of the linear pathway for the total enzyme concentrations  $[E_{1,T}]$ ,  $[E_{2,T}]$  and  $[E_{3,T}]$  calculated with mass-action kinetics (blue), dilute (orange) and crowded (green) ( $\phi_M = 0.3$ ) GEEK for A) diffusion controlled enzyme  $d = 10^0$  and B) a reaction controlled enzyme  $d = 10^{-2}$ .

the rate-limiting step as it shows the largest control coefficient, whereas, in the diffusion-controlled case, the first enzyme is the limiting factor, as the control coefficient indicated that an increase of these total enzyme concentrations would have the most substantial effect on the flux through the pathway. Also, the diffusion-controlled case appears to be less affected by crowding as the control coefficients change only minimally for  $\phi_M$ . Whereas the reaction-controlled case it is strongly impacted by the increase in the molecular volume fraction. Upon increase of the macromolecular volume fraction to  $\phi = 0.3$ , the reaction-controlled pathways behave entirely differently as the first enzyme becomes the rate-limiting step, whereas the last step becomes the least impact-full. To understand this phenomenon, we must consider that the maximal rate  $V_{max}$  of reaction-controlled enzymes appears to be stronger impacted by crowding than for diffusion-controlled enzymes, as is shown in the previous chapter as well as the fact that the last metabolite in this pathway has only 70% of the volume of the first metabolite in the pathway. Thus, crowding impacts the kinetics of the first enzyme more severely than that of the last one, driving it stronger towards saturation and reducing its maximal rate until it becomes the rate-limiting step.

### 5.4.2 Branched pathway

For the second case study, we consider a simple branched pathway with three enzymes where one of the subsequent enzymes is significantly larger than the first enzyme and the enzyme of the alternative path. Both of the subsequent enzymes are assumed to have the same dissociation constants  $K_{D,X_k,E_m \rightarrow E_m X_k}$ ,  $K_{D,X_p,E_m \rightarrow E_m X_p}$ , standard free energy of the overall reaction  $\Delta_{X_k \rightarrow X_p} G$  and the same biocatalytic rate constant  $k_{ES \rightarrow EP}$ . With this, we aim to see the

Table 5.6 – Enzyme parameters for the branched pathway

Enzyme $m$	$R_{E_m}$ [nm]	$\Delta_{X_k \rightarrow X_p} G$ $RT$	$K_{D, X_k, E_m \rightarrow E_m X_k}$ [M]	$K_{D, X_p, E_m \rightarrow E_m X_p}$ [M]	$k_{ES \rightarrow EP}$ [s <sup>-1</sup> ]
1	3	-3	$10^{-3}$	$10^{-2}$	$10^3$
2	3.5	-2	$10^{-2.5}$	$10^{-1.5}$	$10^3$
3	3	-1	$10^{-2.5}$	$10^{-1.5}$	$10^3$

effect of enzyme size on the control coefficients in crowded conditions. It is further assumed that all substrates are of the same size  $r_X = 1$  nm.

We calculate the control coefficients as described above for the linear pathway with  $[X_1] = 10^{-1} K_{M,S}^{E_1}$  and  $[X_3] = [X_4] = 10^{-2} K_{M,S}^{E_1}$ . In contrast to the linear pathway, we have three different control coefficients as the pathway splits into  $v_2$  and  $v_3$  at  $X_2$  and upregulation in the upper branch of the pathway would have a decreasing effect on the flux of the lower branch and vice versa. For the branched pathway, we find surprisingly similar results between the diffusion-controlled case (Upper row in figure 5.4) and the reaction-controlled case (Lower row in figure 5.4). Further, comparing figure C) with E) and D) with F) we find that the substantially large enzyme  $E_2$  has no significant effect on the control coefficients of  $v_2$  and  $v_3$  with respect to  $[E_{2,T}]$  and  $[E_{3,T}]$ . We find that the control coefficients between the two branches are symmetric  $C_{[E_{3,T}]}^{v_2} \approx C_{[E_{2,T}]}^{v_3}$  and  $C_{[E_{3,T}]}^{v_3} \approx C_{[E_{2,T}]}^{v_2}$  suggesting that the size difference of the  $E_2$  is not impacting the kinetics substantially although the volume of  $E_2$  is 50% increased  $V_2 = 1.5V_2$ .

## 5.5 Discussion

In this chapter, we combine the theoretical model we presented in chapter 4 with the efficient GEEK approximation presented in chapter 3. The combination of these two methods allowed us to calculate control coefficients for crowded prototypical pathways efficiently. Our results suggest that depending on the enzyme parameters, the enzyme elasticities, and with this consequently, the control coefficients can be strongly altered when considering the changes of the kinetics due to crowding and diffusion effect. As mentioned in chapter 4, we show for the first time how the effective steady-state rate constants for a diffusion influenced reaction-diffusion system change if the system is driven out of equilibrium. Here we show that for diffusion-controlled kinetics, these effects propagate to the concentration and parameter elasticities, and with this alter the expected response behavior of pathways. The difference in the expected response may have severe consequences when evaluating metabolic engineering strategies using metabolic control analysis.

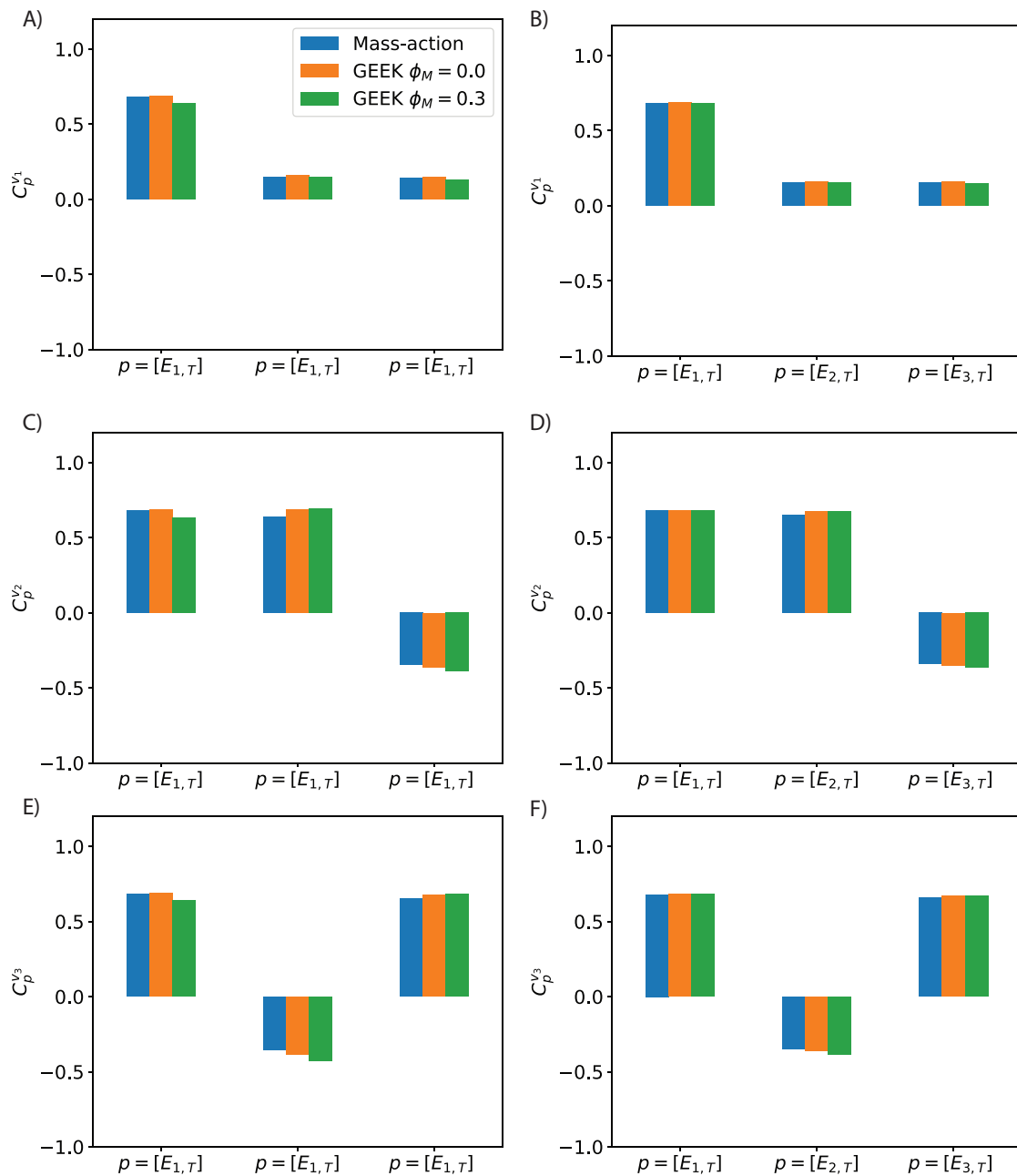


Figure 5.4 – Control coefficients of the fluxes  $v_1$ ,  $v_2$  and  $v_3$  in the branched pathway with respect to the total enzyme concentrations  $[E_{1,T}]$ ,  $[E_{2,T}]$  and  $[E_{3,T}]$  calculated with mass-action kinetics (blue), dilute (orange) and crowded (green) ( $\phi_M = 0.3$ ) GEEK for A), C) and E) a diffusion controlled enzyme  $d = 10^0$  as well as B) D) and F) for a reaction controlled enzyme  $d = 10^{-2}$

Based on the results obtained from the prototypical system, we believe that it is essential to consider crowded kinetics for the design of new pathways. The here presented formulation offers an efficient way to account for crowded kinetics in the metabolic control analysis. In future work, we aim to apply the presented formulation in large-scale metabolic models, to guide the analysis of diseased phenotype and aid the design of new pathways for the synthesis of valuable biochemicals.



## 6 Conclusions and Perspectives

This chapter outlines the conclusions of the previous chapters and suggests a path forward account for confinement effects in large scale networks. We further provide perspectives on how the methods developed in this thesis may aid in moving towards this goal and which other problems still need to be addressed on the way towards large scale reevaluation of *in vitro* data.

### 6.1 Conclusions

Computational studies, combined with *in vitro* experiments offer a powerful tool to interrogate complex biochemical systems. In **chapter 2**, we dissected the reaction kinetic landscape of protein binding to chromatin using computational modeling and *in vitro* experiments. It is well known that the intracellular compartments are a complex environment that strongly alters the effective transport mechanisms as well as the effective reaction kinetics. Such effects are not captured when investigating a system in a dilute *in vitro* setup. Mathematical modeling and computer simulation allow us to reevaluate the effective reaction kinetic parameters in under *in vivo* like conditions. We showed that enzyme essays could be corrected using approximate kinetic rate laws identified with particle simulation methods (**Chapter 3**) or mean-field approaches based on the Smouchowski equation (**Chapter 4**). Finally, we integrated the *in silico* generated knowledge of crowded enzyme kinetics into a prototypical reaction network to study their responses to enzyme overexpression (**Chapter 5**).

It is essential to understand the kinetics of the biochemical reactions within the intracellular environment to understand cellular function, diseased phenotypes, and enable the design of new biotechnological applications. Therefore, new approaches are required to identify the

## Chapter 6. Conclusions and Perspectives

---

parameters and structures most sensitive to the complexity of the intracellular environment in large scale systems. Such approaches would enable then the targeted computational analysis of the components most sensitive to the additional complexity introduced by phenomena such as macromolecular crowding, one- or two-dimensional confinement, active transport properties, or phase separation phenomena.

In **chapter 2**, we use computational modeling in combination with parameter identification of *in vitro* experimental data to identify the molecular binding mechanism of a multivalent, chromatin-binding protein (HP1). Using sensitivity analysis, we investigate how the binding mechanism is altered for the different subtypes of HP1 that are responsible for different functions. The results show that all the different HP1 subtypes shared a similar binding mechanism where unspecific DNA mediated interactions were used to guide the protein to the specific PTM binding sites where it then was retained for significantly longer times. Instead of static interactions that are governed by long retention times, our combined computational and experimental analysis (Bryan et al., 2017) suggests that effectors are generally trapped in the vicinity of the PTM regions via multiple moderate affinity interactions. Fast on and off rates lead to sequential rebinding of the effectors and thus their accumulation in the vicinity of their PTM targets. Such a dynamic binding mechanism facilitates a fast response of the epigenetic regulation system to changes in the environment or a change of the cell state (Ayoub et al., 2008; Fischle et al., 2005). The parameters provided for the computational model have been identified using a continuous deterministic model and a single parameter identification method. This procedure assumes that the characteristic time scales of the deterministic and the stochastic model are conserved. Although it was verified by stochastic simulation methods that this assumption holds for the identified models, it remains to be investigated whether parameter sets exist that exhibit the characteristic binding times only in the stochastic formulation by identifying the parameters directly on the stochastic model formulation, as in (Öcal et al., 2019). Nevertheless, we believe that the resulting computational model of *in vitro* protein-chromatin interactions can provide the bases for more advanced computational studies to account for crowding effects in the nucleus based on the methods presented throughout **chapters 3 to 5**.

In **chapters 3**, we investigate the effect of macromolecular crowding on the *in vitro* data of phosphoglycerate mutase, a well-characterized enzyme in glycolysis. We, therefore, introduce a new type of power-law kinetics to capture crowding effects in ODE type models, generalized elementary kinetics (GEEK). Using particle simulations, we identify the parameters of the approximate kinetics and subsequently create effective in-silico enzyme assays to characterize



the maximal enzyme rates  $V_{max}^{+/-}$  and the Michaelis-Menten parameters  $K_{M,S}$  and  $K_{M,P}$  at different volume fraction. We find that with increasing macromolecular volume fraction, the association rate increases, and the dissociation rate decreases for this enzyme resulting in a significant decrease of the maximal enzyme rates and the Michaelis-Menten parameters. Our results are in agreement with *in vitro* studies for equimolar enzymes (Uni-Uni, Bi-Bi) (Pastor et al., 2011; Balcells et al., 2014; Pastor et al., 2014), only for a (Uni-Bi) reaction mechanism Pastor et al. (2014) report an increase in the Michaelis-Menten parameter with increasing crowding agent concentration, such phenomena could be targets for future investigations. Although the results are in reasonable agreement with *in vitro* experiments, it shall be noted that the presented results only consider the volume exclusion of the molecules as hard-sphere, neglecting any unspecific and specific attraction or "stickiness" of the molecules and the crowding agents and among the crowding agents. Further, the simulation does not account for hydrodynamic interactions and anisotropy of the molecules. It remains thus to be determined how strong these complexities affect the reaction rate constants and if the hard-sphere contribution is, in fact, dominant.

For **chapter 4**, we extend the analysis to diffusion-controlled enzymes in crowded conditions. For such enzymes, diffusion is sufficiently slow so that it becomes a key factor for the reaction kinetics as substrates and enzymes need to be transported towards and products and enzymes away from each other. We provide a theoretical model based on the Smouchowski equation and solution thermodynamics extending the work of Gopich and Szabo (2018) and Berezhkovskii and Szabo (2016) to crowded reaction networks displaced from equilibrium. To solve the set equations for any reaction system, we further derive a FEM formulation for the problem. Further, we derive an analytical solution for the steady-state flux of reversible, bi-molecular, diffusion-controlled reactions. Our results show that the effective reaction rate constant depends on the ratio between the educt and product concentrations, as well as the dissociation rate constant, suggesting that diffusion-controlled reactions have an apparent, displacement-dependent reaction rate constant. This shows for the first time that the apparent steady-state reaction rate constant of diffusion-controlled kinetics depends on the steady-state concentrations. The model further shows that this phenomenon occurs besides, not instead, the time dependency of the apparent rate constant (Agmon and Szabo, 1990; Grima and Schnell, 2006a). Finally, we used the model to investigate the different crowding effects on reaction- and diffusion-controlled Michaelis-Menten mechanisms. The results reveal that the maximal rate of diffusion-controlled reaction mechanisms is less impacted by macromolecular crowding compared to reaction controlled mechanisms. Further, we show that the Michaelis-Menten constant changes with the activity of the respective association

## Chapter 6. Conclusions and Perspectives

---

reaction independent of reaction or diffusion limitation. This insight may offer a computationally inexpensive way to estimate changes of the effective Michaelis-Menten constant for the integration into large-scale kinetic models. Similarly to **chapter 3**, we assume only hard-sphere interactions between the molecules and neglect hydrodynamic and attractive interactions as well as their anisotropy. It thus also remains here to be investigated which of these interactions dominate in a crowded environment. We further use an approximative closure to express the thermodynamic and structural quantities of the resulting hard-sphere mixture. As the results of **chapter 3** and **chapter 4** show similar effects on the reaction rate constants for reaction controlled kinetics, we are confident that this approximation captures the crowding effects sufficiently.

Finally, in **chapter 5**, we combine the previously developed methods of the generalized elementary kinetics (**Chapter 3**) with the theoretical model (**Chapter 4**) to investigate the effects of macromolecular crowding on the sensitivities in reaction networks. Therefore, we present a framework that allows calculating the control coefficients for elementary reaction networks under crowded conditions extending the work of Kacser and Burns (1973), Hatzimanikatis and Bailey (1996, 1997) as well as Hatzimanikatis (1999). Our results on prototypical reaction networks suggest that the global sensitivity of concentrations and fluxes in a reaction network are strongly impacted by diffusion and crowding. Therefore, we suggest that for a conclusive analysis of a reaction network, detailed knowledge of the elementary *in vitro* reaction kinetics is required. The knowledge of the enzyme parameters in dilute conditions is not sufficient to determine the impact of crowding on the reaction system's parameter sensitivities. Quantitatively, these results are subject to the same theoretical assumptions described for **chapters 3** and **4** and are thus subject to the same limitations. Further, it should be noted that metabolic control analysis is based on local elasticities and giving insight into which reaction is locally rate-limiting. For large changes in the enzyme expression, the full non-linear system should be considered to analyze the respective flux and concentration responses.

In this thesis, we provided some insight into protein adsorption systems confined to 1D like domain as well as enzyme kinetics and enzymatic reaction network confined by macromolecular crowding. We developed novel methods to address crowding and non-ideal reaction kinetics in a computationally efficient way. Although more work is needed to identify and characterize the contributions of the different intermolecular interactions, these methods enable us to progress towards a large scale reevaluation of *in vitro* data for large scale kinetic models. Such models will provide an improved tool to apply computational engineering strategies to understand cellular function, diseased phenotypes, and design new biotechnological

applications.

## 6.2 Future perspectives

In order to generate reliable models of the cellular biochemistry, tailored to specific applications, the set of tools to reevaluate the results of *in vitro* experimental data need to be extended to include other phenomena in addition to macromolecular crowding in three dimensions. We propose three key areas where we consider that translating the results of *in vitro* systems into models with *in vivo* like properties is of great importance.

### 6.2.1 Membrane thermodynamics and reaction kinetics

Lipid membranes surround each biological cell and most of its various compartments. These membranes separate the biochemistry between the cell from their exterior as well as between different compartments. Further, these membranes host many different enzymes that catalyze reactions required for various biological functions such as signal transduction and transport reactions (Bondar and Keller, 2018). The proteins attached to this membrane diffuse on the fluid-like membrane rather than in an aqueous solution resulting in different effective viscosity. In addition to experiencing a different kind of viscosity, their movement is restricted to two dimensions (Bondar and Keller, 2018; Verger et al., 1973; Yogurtcu and Johnson, 2015). The various proteins attached to the membrane occupy about 15-35% of the membrane surface area resulting in macromolecular crowding effects (Zhou, 2009). We expect both the crowding effects and the two-dimensional confinement to alter the effective transport properties enzymes on the membranes. Considering those membrane-bound enzymes can react with membrane-bound species or with species that diffusion from solution to the surface, to different classes of problems, need to be addressed. Some of these enzymes catalyze further reactions that involve the lipids of the membrane (Emiola et al., 2015; Bondar and Keller, 2018). Thus these enzymes are effectively altering the nature of their solvent. We would expect this to have significant effects on the reaction thermodynamics as the activity terms of the product and educts are dependent on the solvent composition. We propose that thermodynamic models, as used in **chapter 4**, may aid in modeling this effect in a dynamic matter. Also, the theoretical model presented in **chapter 4**, can be adapted for the reactants to diffuse in two dimensions (Szabo, 1989). To address mixed problems of reaction with mixed degrees of freedom, we currently see no other option than either lattice or off-lattice methods to characterize the reaction dynamics (Schnell and Turner, 2004; Grima and Schnell, 2007, 2008;

## Chapter 6. Conclusions and Perspectives

---

Grima, 2010; Mourao et al., 2014; Sturrock, 2016; Schoneberg and Noe, 2013; Biedermann et al., 2015; Smith and Grima, 2017) and identify the approximate reaction kinetics similar to **chapter 3**.

### 6.2.2 Active processes

Processes that use chemically stored energy to drive dynamics systems out of equilibrium are called active. Such processes can induce symmetry-breaking events that are especially important in developmental biology (Goehring et al., 2011; Kruse et al., 2005; Blanchard et al., 2010). The most studied biological active systems are the microtubules and actin-myosin systems. These systems can induce direction-dependent shear forces within the intercellular fluid, creating convective flows leading to the formation of something called an active-polar gel (Kruse et al., 2004, 2005; Prost et al., 2015). These active flows strongly alter the transport properties between reactions in the cytosol and the membrane. Recent work of Xu et al. (2019) further suggests that enzyme activity can facilitate the diffusion within a crowded environment, suggesting enzymes themselves could be active particles propelled by the driving force that drives catalytic transformation (Zhang and Hess, 2019). As both these processes change the fundamental transport properties of the molecules, it is also expected that they change the effective reaction kinetics (MacDonald et al., 2019). We thus conclude that a comprehensive computational analysis of these phenomena within an *in vivo* like environment will provide further insight into their impact on the biochemical reaction kinetics. These insights will be of special interest when studying biochemical processes during cell division and development.

### 6.2.3 Phase separation

With the discovery of membrane-less compartment liquid-liquid like phase separation has been introduced as a concept of vital importance for various biological functions (Banani et al., 2017; Hyman et al., 2014). In these systems, phase-separation is often induced by weakly interacting proteins that, upon a critical concentration, separate into a liquid phase with a higher protein concentration and a phase with lower protein concentration. Upon phase separation, thermodynamic forces drive the concentrations inside and outside of the separated droplets towards the local thermodynamic equilibrium concentrations. Thus, when the number of protein molecules in the cell changes, the droplet size changes, but the concentrations inside and outside the droplets remain constant. This phenomenon could act as a possible regulatory mechanism to buffer enzyme levels in biochemical reaction networks (Hyman et al., 2014; Holehouse and Pappu, 2018; Stoeger et al., 2016; Klosin et al., 2020).

To the current day, most research on phase-separation involves the *in vitro* reconstitution of the phase-separating systems (Patel et al., 2015; Visco et al., 2016; Larson et al., 2017; Strom et al., 2017). Thus, methods to integrate this knowledge to models of the effective biochemical reaction kinetics with *in vivo* like properties would be an invaluable asset to understand how phase-separated systems interact with such reaction networks. Kinetic models of phase-separation have already been shown to be a great tool to analyze noise in engineered phase separation systems Klosin et al. (2020). Approaches to characterize the *in vitro* reconstituted interactions between different classes of proteins in combination with corrections on their free energy density would further aid the identification of phase separation systems *in vivo*.



# A Supplementary information particle methods

## A.1 Measuring the bimolecular elementary rate constants

As described in section 3.2.4, the effective bimolecular rate constant can be extracted from the effective collision frequency  $z_{A,B}$  between two species, A and B. This collision frequency is estimated as the number of collisions between A and B in an integrated time interval  $c_{A,B}(t, t + \Delta t)$  per time step  $\Delta t$ :  $z_{A,B}(t, t + \Delta t) = c_{A,B}(t, t + \Delta t) / \Delta t$  (A.1). In figure A.1, two examples for time traces of collisions per time interval for a reaction-controlled association reaction of S and E are presented. From the running mean, it can be seen that there is no obvious time dependency of the collision frequency observable. This result is enforced by the fact the distribution of the collisions at the beginning, the end, and over the complete measurement interval follow a similar distribution

## A.2 Regression for GEEK parameters

When investigating the measured relative rate constants for pgm as a function of the individual rate constants, it can be seen that there is no dependency of the rate constants with respect to the individual concentration. Only an increase in the conditional variance towards smaller concentrations can be seen, see figure A.2. Thus ordinary least squares (OLS) fitting cannot be applied as the data exhibits heteroscedasticity. We show that we obtain normally distributed residuals by weighting the data points by the inverse of the conditional standard deviation  $\sqrt{V(R|X)}$ , where  $X$  is the n-dimensional input variable of the regression model and  $R$  are the residuals of the OLS output variable. In figure A.2, it can be clearly seen that the weighted residuals resemble a normal distribution.

## Appendix A. Supplementary information particle methods

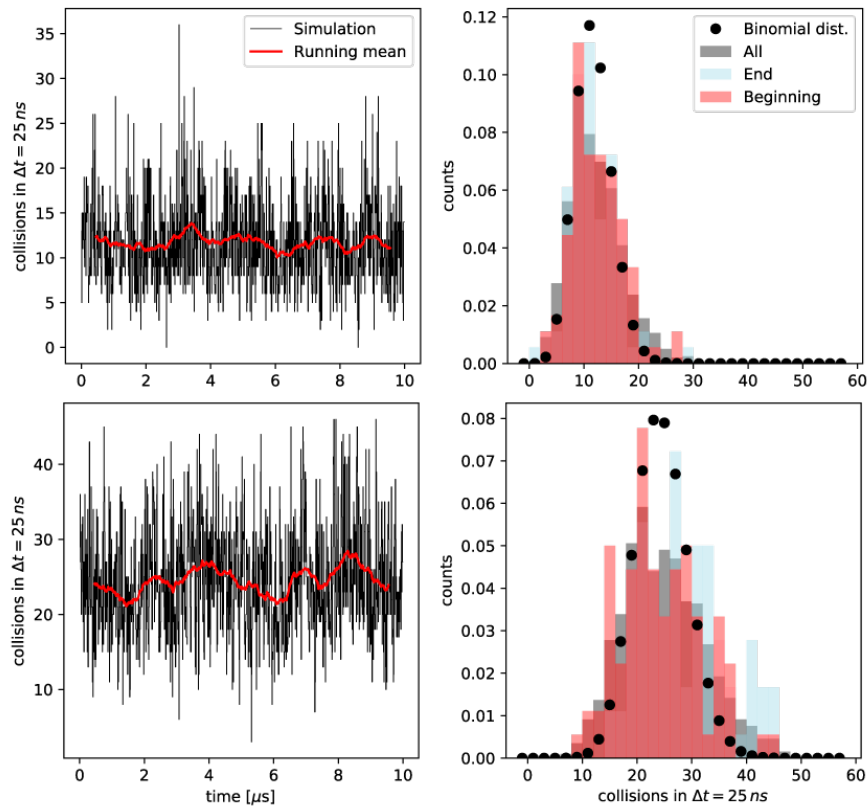


Figure A.1 – Left column time traces of collision events between E and S as a function of time and the running mean over 100 time intervals. Right column histograms of all data point of the collisions time trace (All), the first (Beginning), and the last (End) 100 data points compared with a binomial distribution where  $p = \langle c_{(E,S)} \rangle / N_E N_S$  and  $n = N_E N_S$ . The upper row show the results with  $\phi = 0\%$  the lower row for  $\phi = 40\%$  for the crowding size distribution in E. coli.



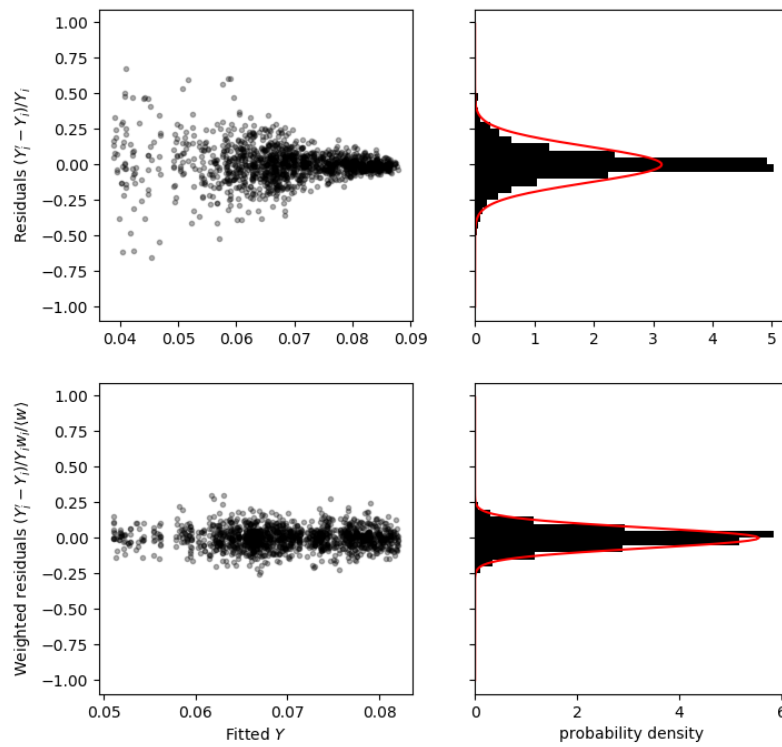


Figure A.2 – Model results for OLS and WLS for the model output  $Y_i = \log(k_{1,f,eff}/k_{1,f,0})$ . Left column: Residuals vs. fitted output values  $Y_i'$  Right column: Probability density of the residuals. Upper row: Residuals of the OLS model. Lower row: Effective residuals of the WLS model.

## Appendix A. Supplementary information particle methods

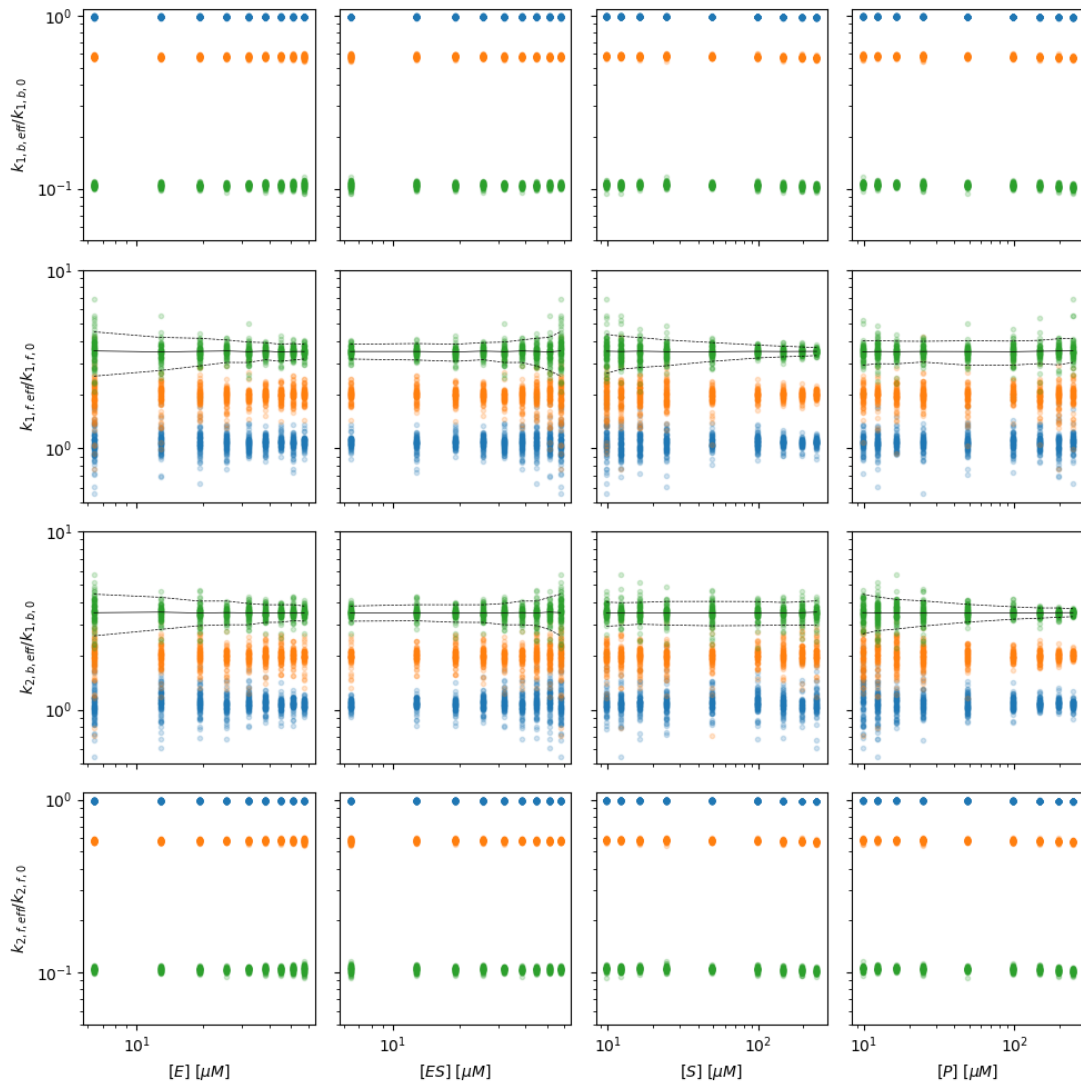


Figure A.3 – Projection of the simulated data points onto the respective concentration axis for (blue)  $\phi = 0\%$  (orange)  $\phi = 30\%$  and (green)  $\phi = 50\%$  inert volume fraction with the E. Coli size distribution. The black line denoted the conditional mean, and the dashed line denoted the conditional 5% and 95% percentiles at the corresponding concentration value for  $\phi = 50\%$  inert volume fraction.

### A.3 Validation of GEEK

In the following section, we first validated whether the results of the GEEK approximation are in agreement with detailed openbread simulations, as described in the main text. Second, we validated whether geek is also able to capture the results of the crowder free Cichocki-Hinsen algorithm (Smith and Grima, 2017). To perform these comparisons, we used a simple association-dissociation model with two different parameter sets:



#### A.3.1 Computational details of the validation simulations

The two parameter sets only differ in their association rate the remaining model parameters considered a diffusion coefficient  $D_{A/B} = 500 \mu\text{m}^2 \text{s}^{-1}$  a mass  $m_{A/B} = 10 \text{kDa}$  and a collision radius  $r_{A/B} = 2 \text{nm}$  for the species  $A$  and  $B$ , a diffusion coefficient  $D_C = 350 \mu\text{m}^2 \text{s}^{-1}$ , a mass  $m_C = 20 \text{kDa}$  and collision radius  $r_{A/B} = 3 \text{nm}$  for the species  $C$  and a cubic simulation volume  $V = 10^6 - 18) \text{L}$ . For the reaction parameters we consider a dissociation constant  $K_D = 50 \mu\text{M}$  and an association rate constant  $k_{f,diff} = 5 \times 10^9 \text{M}^{-1} \text{s}^{-1}$  ( $k_{f,diff}/\gamma_{A,B} \approx 5$ ) for the diffusion controlled case. Whereas for the reaction controlled case we consider an association rate constant  $k_{f,react} = 5 \times 10^7 \text{M}^{-1} \text{s}^{-1}$  ( $k_{f,react}/\gamma_{A,B} \approx 500$ ). To simulate crowding we introduced inert molecules of the size  $2.6 \text{nm}$  at different volume fractions. As in the case presented in the main text, the dynamics viscosity of the liquid between the particles was assumed to be water with  $0.7 \text{Pas}$  at  $T = 310.15 \text{K}$ . The system is considered to be isothermal  $T = \text{const}$ . To compare the methods we simulate ten independent time traces for an initial rate experiment with the initial concentrations  $[A] = [B] = 50 \mu\text{M}$  and  $[C] = 0 \mu\text{M}$ . To apply the GEEK framework, each timestep all possible first-order reactions are attempted  $L = 100$  times. For the regression input space, all combinations of substrate and product concentrations that were  $n_i$ -fold increased and  $n_d$ -fold decreased with respect to the reference concentrations  $[A]_0 = [B]_0 = [C]_0 = 50 \mu\text{M}$  were used, with  $n_d \in [1, 2]$  and  $n_i \in [1, 2, 4]$ . Each sampled concentration state is simulated  $1 \mu\text{s}$  where the first  $0.5 \mu\text{s}$  are not considered to fit the GEEK. Furthermore, ten independent realizations of the crowding population were used for every concentration sample to capture the variability that comes from differently sized crowding-agents drawn from the size distribution.

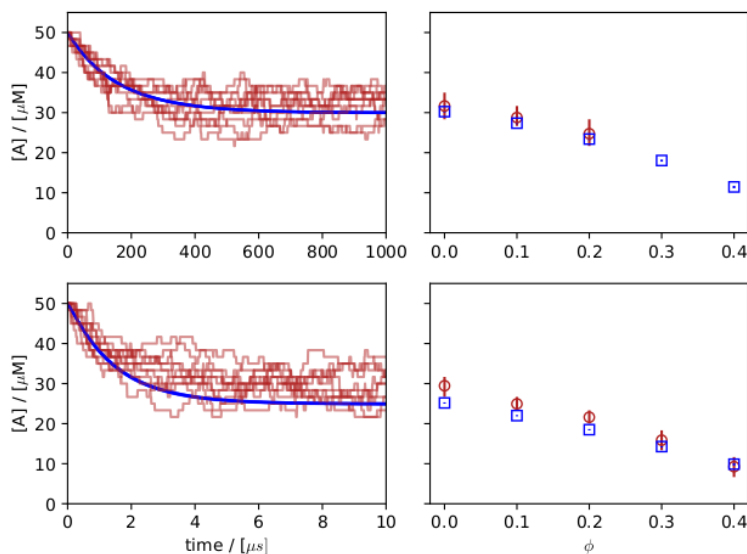


Figure A.4 – Concentration of  $[A]$  as a function of time  $t$  for  $\phi = 0$  for GEEK (blue) and openbread (red) (left column) and concentration in equilibrium for different  $\phi$  (right column). For the reaction controlled case (upper row) and the diffusion controlled case (lower row).

### A.3.2 Validation of GEEK based on hard-sphere Brownian reaction dynamics

In a first step, we compare the time traces for GEEK and openbread for the dilute case, i.e., without any inert molecules, see Supporting Figure 5 left column. The results show that for the reaction controlled case GEEK is able to capture the mean dynamics of the detailed openbread very well, for the diffusion controlled case the mean dynamics of the initial rate is captured very well, but a slight deviation of the equilibrium concentration  $[A]$  is visible. In a next step we characterized the distribution of  $[A]$  close to equilibrium, i.e.  $t \geq 500 \mu\text{s}$  in the reaction controlled and  $t \geq 5 \mu\text{s}$  in the diffusion controlled case, for different inert volume fraction, see figure A.4 right column. It can be seen that for higher volume fractions of inert molecules, both the GEEK and the openbread results show that the equilibrium is shifted towards the production of  $[C]$ , i.e., the equilibrium concentration  $[A]_{eq}$  drops with increasing volume fraction. We also observe that for higher volume fractions, the difference between the mean of  $[A]$  in openbread and GEEK is reduced.

Finally, we compared the initial reaction rate characterized as the mean change of the reactant  $[A]$  over an initial time interval  $[0, t_{init}]$ , where  $t_{init} = 0.5 \mu\text{s}$  for the diffusion controlled case and  $t_{init} = 50 \mu\text{s}$  for the reaction controlled case (see figure A.5). Similar to the equilibrium properties, we see that the GEEK model is able to capture the mean initial rate of the hard-sphere Brownian reaction dynamics model. It also can be seen that in the reaction controlled

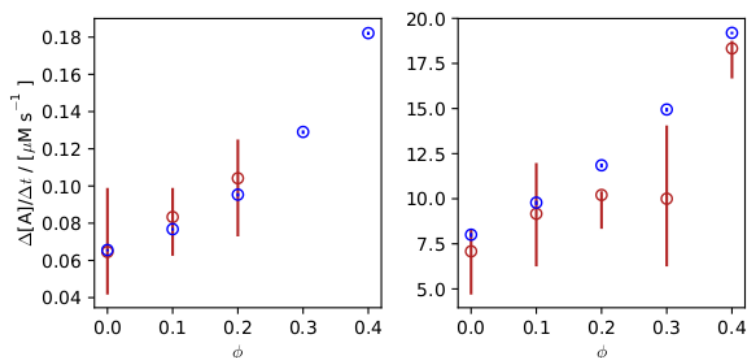


Figure A.5 – Initial reaction rate measured as the mean change of  $[A]$  for GEEK (blue) and openbread (red) measured for different  $\phi$ , for the reaction controlled case (left) and the diffusion controlled case (right).

case, the GEEK approximation is in close agreement to the detailed simulation. In both cases, GEEK captures the increase of the initial rate visible in the hard-sphere Brownian reaction dynamics.

### A.3.3 Validation of GEEK based on the crowder free Cichocki-Hinsen algorithm

To provide further evidence that GEEK is able to approximate the behavior of high-cost simulations based on the first physical principle, we simulate the association-dissociation system described above using the crowder free Cichocki-Hinsen algorithm Smith and Grima (2017). As described above we compare the concentrations for  $t \geq 500 \mu\text{s}$  in the reaction controlled and  $t \geq 5 \mu\text{s}$  in the diffusion controlled case as well as the initial reaction for  $t \leq 0.5 \mu\text{s}$  in the diffusion controlled case and  $t \leq 50 \mu\text{s}$  in the reaction controlled case. We again show that the GEEK models are able to approximate the dynamics of the high-cost model. More importantly, GEEK models are able to approximate the effects crowding has on the initial rate experiment. For both cases, GEEK is able to capture the trends of approximation for the equilibrium concentrations (see figure A.6) and the initial reaction rates (see figure A.7). When comparing the initial reaction rates, we observe that the estimated reaction limited initial reaction rates are in better agreement with the GEEK approximation than the corresponding diffusion controlled initial reaction rates (see figure A.7).

## Appendix A. Supplementary information particle methods

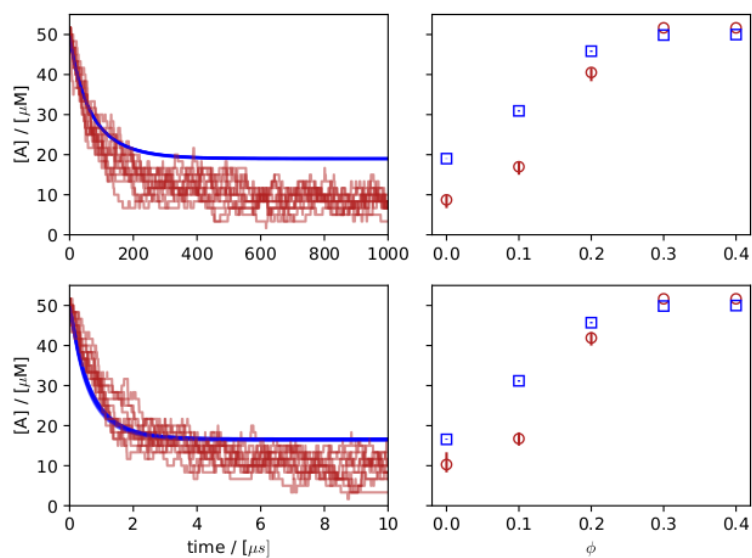


Figure A.6 – Concentration of  $[A]$  as function of time  $t$  for  $\phi = 0$  for GEEK-CFCH (blue) and CFCH (red) (left column) and concentration in equilibrium for different  $\phi$  (right column). For the reaction controlled case (upper row) and the diffusion controlled case (lower row).

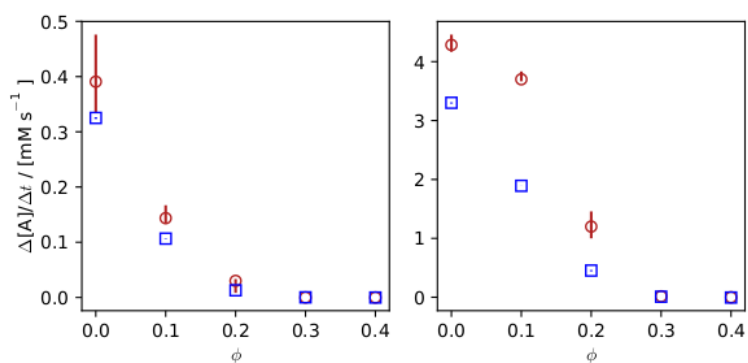


Figure A.7 – Initial reaction rate measured as the mean change of  $[A]$  for GEEK- CFCH (blue) and CFCH (red) measured for different  $\phi$ , for the reaction controlled case (left) and the diffusion controlled case (right).

#### A.3.4 Discussion on the results of the HSRD and CFCH simulations

A comparison between figures A.4 and A.5 as well as A.6 and A.7 show that the hard-sphere Brownian dynamics algorithm and the crowder free Cichoki-Hinsen algorithm are not yielding the same results for the same crowding conditions. We suspect that the difference in the crowding sensitivity originates from the difference in the collision model of the two algorithms. The hard-sphere Brownian dynamics algorithm models every non-reactive collision as an explicit elastic hard-sphere collision (see figure A.8 b) ) both the Cichoki-Hinsen algorithm and the crowder-free Cichoki-Hinsen algorithm are rejecting the propagation moves that would lead to overlap. In this work, we used the hard-sphere Brownian dynamics algorithm as described by Strating as it was successfully applied his algorithm to non-equilibrium systems of hard-spheres (Strating, 1999). The algorithm presented by Cichoki and Hinsen ?? is only valid to obtain the correct radial distribution functions in equilibrium systems. They show that for non-equilibrium systems, an additional non-overlap correction has to be implemented ?. This correction is not implemented in the crowder-free Cichoki-Hinsen algorithm (Smith and Grima, 2017). Therefore, we acknowledge that the model predictions for these simulations strongly depend on the microscopic model. Nevertheless, we showed that independent of the microscopic simulation method GEEK models are able to approximate the dynamic behavior of the complex particle simulation. Thus GEEK can be used as a reliable method to capture the dynamics of crowded enzyme kinetics and incorporate crowded behavior into larger-scale kinetic models.

## Appendix A. Supplementary information particle methods

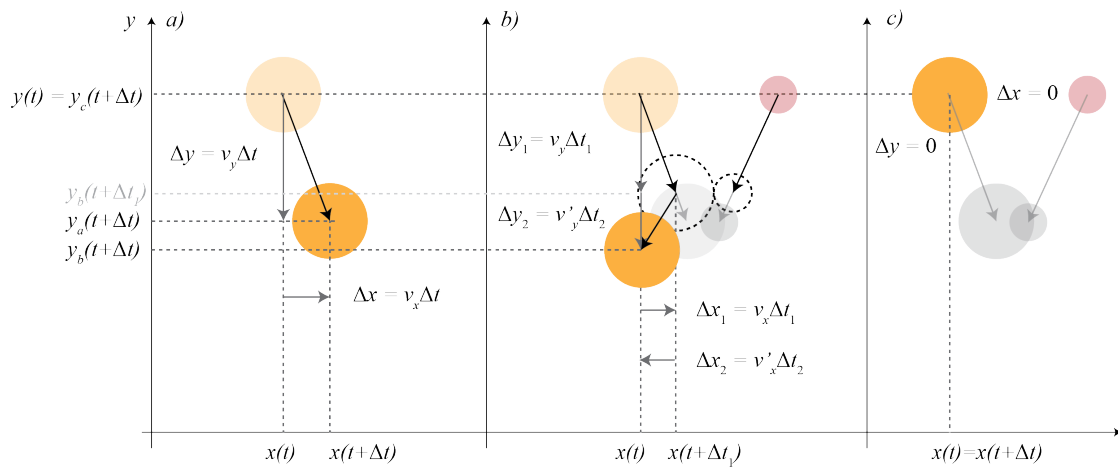


Figure A.8 – Comparison of different propagation schemes. a) Brownian motion where the propagation is simply determined by the velocity  $v$  drawn from the respective velocity distribution function. b) Explicit elastic hard-sphere collision, particles are moved with the initial velocity  $v$  until time  $t + \Delta t_1$  when the collision occurs. The velocities are updated according to the law of momentum conservation then propagated for the remaining part of the time step  $\Delta t_2 = \Delta t - \Delta t_1$ . c) Propagation according to the Cichoki-Hinsen algorithm where the collision is simply rejected if the hypothetical positions after the time  $\Delta t$  lead to overlap with another particle.



## Bibliography

- Agmon, N. and Szabo, A. (1990). Theory of reversible diffusion-influenced reactions. *The Journal of Chemical Physics*, 92(9):5270–5284.
- Alberts, B. (2014). *Essential Cell Biology*. Garland Science, New York, fourth edition.
- Allen, M. P. (1980). Brownian Dynamics Simulation of a Chemical-Reaction in Solution. *Molecular Physics*, 40(5):1073–1087.
- Andreozzi, S., Chakrabarti, A., Soh, K. C., Burgard, A., Yang, T. H., Van Dien, S., Miskovic, L., and Hatzimanikatis, V. (2016a). Identification of metabolic engineering targets for the enhancement of 1,4-butanediol production in recombinant *E. coli* using large-scale kinetic models. *Metab Eng*, 35:148–159.
- Andreozzi, S., Miskovic, L., and Hatzimanikatis, V. (2016b). iSCHRUNK - In Silico Approach to Characterization and Reduction of Uncertainty in the Kinetic Models of Genome-scale Metabolic Networks. *Metabolic Engineering*, 33:158–168.
- Andrews, S. S., Addy, N. J., Brent, R., and Arkin, A. P. (2010). Detailed Simulations of Cell Biology with Smoldyn 2.1. *Plos Computational Biology*, 6(3).
- Angeles-Martinez, L. and Theodoropoulos, C. (2015). The Influence of Crowding Conditions on the Thermodynamic Feasibility of Metabolic Pathways. *Biophysical Journal*, 109(11):2394–2405.
- Aon, M. A. and Cortassa, S. (2015). Function of metabolic and organelle networks in crowded and organized media. *Frontiers in Physiology*, 5.
- Asmus, J., Müller, C. L., and Sbalzarini, I. F. (2017). L p -Adaptation: Simultaneous Design Centering and Robustness Estimation of Electronic and Biological Systems. *Scientific Reports*, 7(1):1–12.

## Bibliography

---

- Ayoub, N., Jeyasekharan, A. D., Bernal, J. A., and Venkitaraman, A. R. (2008). HP1-beta mobilization promotes chromatin changes that initiate the DNA damage response. *Nature*, 453(7195):682–686.
- Azzaz, A. M., Vitalini, M. W., Thomas, A. S., Price, J. P., Blacketer, M. J., Cryderman, D. E., Zirbel, L. N., Woodcock, C. L., Elcock, A. H., Wallrath, L. L., and Shogren-Knaak, M. A. (2014). Human heterochromatin protein 1 $\alpha$  promotes nucleosome associations that drive chromatin condensation. *The Journal of Biological Chemistry*, 289(10):6850–6861.
- Balcells, C., Pastor, I., Vilaseca, E., Madurga, S., Cascante, M., and Mas, F. (2014). Macromolecular Crowding Effect upon in Vitro Enzyme Kinetics: Mixed Activation-Diffusion Control of the Oxidation of NADH by Pyruvate Catalyzed by Lactate Dehydrogenase. *Journal of Physical Chemistry B*, 118(15):4062–4068.
- Banani, S. F., Lee, H. O., Hyman, A. A., and Rosen, M. K. (2017). Biomolecular condensates: Organizers of cellular biochemistry. *Nature Reviews Molecular Cell Biology*, 18(5):285–298.
- Bar-Even, A., Noor, E., Savir, Y., Liebermeister, W., Davidi, D., Tawfik, D. S., and Milo, R. (2011). The Moderately Efficient Enzyme: Evolutionary and Physicochemical Trends Shaping Enzyme Parameters. *Biochemistry*, 50(21):4402–4410.
- Barker, J. A. and Henderson, D. (1976). What is "liquid"? Understanding the states of matter. *Reviews of Modern Physics*, 48(4):587–671.
- Benichou, O., Chevalier, C., Klafter, J., Meyer, B., and Voituriez, R. (2010). Geometry-controlled kinetics. *Nat Chem*, 2(6):472–7.
- Berezhkovskii, A. M. and Szabo, A. (2016). Theory of Crowding Effects on Bimolecular Reaction Rates. *Journal of Physical Chemistry B*, 120(26):5998–6002.
- Biedermann, J., Ullrich, A., Schoneberg, J., and Noe, F. (2015). ReaDDyMM: Fast interacting particle reaction-diffusion simulations using graphical processing units. *Biophys J*, 108(3):457–61.
- Blanchard, G. B., Murugesu, S., Adams, R. J., Martinez-Arias, A., and Gorfinkiel, N. (2010). Cytoskeletal dynamics and supracellular organisation of cell shape fluctuations during dorsal closure. *Development*, 137(16):2743–2752.
- Blum, L. and Hoeye, J. S. (1977). Mean spherical model for asymmetric electrolytes. 2. Thermodynamic properties and the pair correlation function. *The Journal of Physical Chemistry*, 81(13):1311–1316.

- Bondar, A.-N. and Keller, S. (2018). Lipid Membranes and Reactions at Lipid Interfaces: Theory, Experiments, and Applications. *The Journal of Membrane Biology*, 251(3):295–298.
- Boyer, P. D. (1997). The Atp Synthase—a Splendid Molecular Machine. *Annual Review of Biochemistry*, 66(1):717–749. \_eprint: <https://doi.org/10.1146/annurev.biochem.66.1.717>.
- Brooks, H. B., Geeganage, S., Kahl, S. D., Montrose, C., Sittampalam, S., Smith, M. C., and Weidner, J. R. (2004). Basics of Enzymatic Assays for HTS. In Sittampalam, G. S., Coussens, N. P., Brimacombe, K., Grossman, A., Arkin, M., Auld, D., Austin, C., Baell, J., Bejcek, B., Chung, T. D. Y., Dahlin, J. L., Devanaryan, V., Foley, T. L., Glicksman, M., Hall, M. D., Hass, J. V., Inglese, J., Iversen, P. W., Kahl, S. D., Kales, S. C., Lal-Nag, M., Li, Z., McGee, J., McManus, O., Riss, T., Trask, O. J., J., Weidner, J. R., Xia, M., and Xu, X., editors, *Assay Guidance Manual*. Bethesda (MD).
- Brown, J. P., Bullwinkel, J., Baron-Lühr, B., Billur, M., Schneider, P., Winking, H., and Singh, P. B. (2010). HP1 $\gamma$  function is required for male germ cell survival and spermatogenesis. *Epigenetics & Chromatin*, 3(1):9.
- Bryan, L. C., Weilandt, D. R., Bachmann, A. L., Kilic, S., Lechner, C. C., Odermatt, P. D., Fantner, G. E., Georgeon, S., Hantschel, O., Hatzimanikatis, V., and Fierz, B. (2017). Single-molecule kinetic analysis of HP1-chromatin binding reveals a dynamic network of histone modification and DNA interactions. *Nucleic Acids Res*, 45(18):10504–10517.
- Buchner, E. (1897). Alkoholische Gärung ohne Hefezellen. *Berichte der deutschen chemischen Gesellschaft*, 30(1):1110–1113. \_eprint: <https://onlinelibrary.wiley.com/doi/pdf/10.1002/cber.189703001215>.
- Campbell, A. (1957). SYNCHRONIZATION OF CELL DIVISION. *Bacteriological Reviews*, 21(4):263–272.
- Canzio, D., Chang, E. Y., Shankar, S., Kuchenbecker, K. M., Simon, M. D., Madhani, H. D., Narlikar, G. J., and Al-Sady, B. (2011). Chromodomain-mediated oligomerization of HP1 suggests a nucleosome-bridging mechanism for heterochromatin assembly. *Molecular Cell*, 41(1):67–81.
- Carlier, M. F. and Pantaloni, D. (1981). Kinetic analysis of guanosine 5'-triphosphate hydrolysis associated with tubulin polymerization. *Biochemistry*, 20(7):1918–1924.
- Cascante, M., Boros, L. G., Comin-Anduix, B., de Atauri, P., Centelles, J. J., and Lee, P. W.-N. (2002). Metabolic control analysis in drug discovery and disease. *Nature Biotechnology*, 20(3):243–249.

## Bibliography

---

- Cheutin, T., McNairn, A. J., Jenuwein, T., Gilbert, D. M., Singh, P. B., and Misteli, T. (2003). Maintenance of stable heterochromatin domains by dynamic HP1 binding. *Science (New York, N.Y.)*, 299(5607):721–725.
- Cianci, C., Smith, S., and Grima, R. (2017). Capturing Brownian dynamics with an on-lattice model of hard-sphere diffusion. *Physical Review E*, 95(5).
- Cichocki, B. and Hinsen, K. (1990). Dynamic Computer-Simulation of Concentrated Hard-Sphere Suspensions .1. Simulation Technique and Mean-Square Displacement Data. *Physica A*, 166(3):473–491.
- Collins, F. C. and Kimball, G. E. (1949a). Diffusion-Controlled Reaction Rates. *Journal of Colloid Science*, 4(4):425–437.
- Collins, F. C. and Kimball, G. E. (1949b). Diffusion-Controlled Reactions in Liquid Solutions. *Industrial and Engineering Chemistry*, 41(11):2551–2553.
- Cross, M., Biberacher, S., Park, S. Y., Rajan, S., Korhonen, P., Gasser, R. B., Kim, J. S., Coster, M. J., and Hofmann, A. (2018). Trehalose 6-phosphate phosphatases of *Pseudomonas aeruginosa*. *FASEB J*, 32(10):5470–5482.
- de Hoog, F. R., Knight, J. H., and Stokes, A. N. (1982). An Improved Method for Numerical Inversion of Laplace Transforms. *SIAM Journal on Scientific and Statistical Computing*, 3(3):357–366.
- Deb, K. and Jain, H. (2014). An Evolutionary Many-Objective Optimization Algorithm Using Reference-Point-Based Nondominated Sorting Approach, Part I: Solving Problems With Box Constraints. *IEEE Transactions on Evolutionary Computation*, 18(4):577–601.
- Deb, K., Pratap, A., Agarwal, S., and Meyarivan, T. (2002). A fast and elitist multiobjective genetic algorithm: NSGA-II. *Ieee Transactions on Evolutionary Computation*, 6(2):182–197.
- Debye, P. (1942). Reaction Rates in Ionic Solutions. *Transactions of The Electrochemical Society*, 82(1):265.
- Demirel, Y. (2013). *Nonequilibrium Thermodynamics: Transport and Rate Processes in Physical, Chemical and Biological Systems*. Newnes.
- Deng, D., Xu, C., Sun, P., Wu, J., Yan, C., Hu, M., and Yan, N. (2014). Crystal structure of the human glucose transporter GLUT1. *Nature*, 510(7503):121–125.

- Desai, A. and Mitchison, T. J. (1997). Microtubule polymerization dynamics. *Annual Review of Cell and Developmental Biology*, 13:83–117.
- Dialynas, G. K., Terjung, S., Brown, J. P., Aucott, R. L., Baron-Luhr, B., Singh, P. B., and Georgatos, S. D. (2007). Plasticity of HP1 proteins in mammalian cells. *Journal of Cell Science*, 120(Pt 19):3415–3424.
- Dominguez, R. and Holmes, K. C. (2011). Actin Structure and Function. *Annual Review of Biophysics*, 40(1):169–186. \_eprint: <https://doi.org/10.1146/annurev-biophys-042910-155359>.
- Eadie, G. S. (1942). The inhibition of cholinesterase by physostigmine and prostigmine. *Journal of Biological Chemistry*, 146(1):85–93.
- Einstein, A. (1905). Über die von der molekularkinetischen Theorie der Wärme geforderte Bewegung von in ruhenden Flüssigkeiten suspendierten Teilchen. *Annalen der Physik*, 322(8):549–560. \_eprint: <https://onlinelibrary.wiley.com/doi/pdf/10.1002/andp.19053220806>.
- Elgin, S. C. R. and Grewal, S. I. S. (2003). Heterochromatin: Silence is golden. *Current biology: CB*, 13(23):R895–898.
- Ellis, R. J. (2001). Macromolecular crowding: Obvious but underappreciated. *Trends in Biochemical Sciences*, 26(10):597–604.
- Ellis, R. J. and Minton, A. P. (2003). Cell biology: Join the crowd. *Nature*, 425(6953):27–8.
- Emiola, A., George, J., and Andrews, S. S. (2015). A Complete Pathway Model for Lipid A Biosynthesis in *Escherichia coli*. *Plos One*, 10(4).
- Faeder, J. R., Blinov, M. L., and Hlavacek, W. S. (2009). Rule-based modeling of biochemical systems with BioNetGen. *Methods Mol Biol*, 500:113–67.
- Feig, M. and Sugita, Y. (2013). Reaching new levels of realism in modeling biological macromolecules in cellular environments. *Journal of Molecular Graphics & Modelling*, 45:144–156.
- Ferguson, M. A. J. (1991). Lipid anchors on membrane proteins. *Current Opinion in Structural Biology*, 1(4):522–529.
- Festenstein, R., Pagakis, S. N., Hiragami, K., Lyon, D., Verreault, A., Sekkali, B., and Kioussis, D. (2003). Modulation of heterochromatin protein 1 dynamics in primary Mammalian cells. *Science (New York, N.Y.)*, 299(5607):719–721.

## Bibliography

---

- Fischle, W., Tseng, B. S., Dormann, H. L., Ueberheide, B. M., Garcia, B. A., Shabanowitz, J., Hunt, D. F., Funabiki, H., and Allis, C. D. (2005). Regulation of HP1-chromatin binding by histone H3 methylation and phosphorylation. *Nature*, 438(7071):1116–1122.
- Flemming, H.-C. and Wingender, J. (2010). The biofilm matrix. *Nature Reviews Microbiology*, 8(9):623–633.
- Francis, N. J., Kingston, R. E., and Woodcock, C. L. (2004). Chromatin compaction by a polycomb group protein complex. *Science (New York, N.Y.)*, 306(5701):1574–1577.
- Fraser, H. I., Kvaratskhelia, M., and White, M. F. (1999). The two analogous phosphoglycerate mutases of *Escherichia coli*. *Febs Letters*, 455(3):344–348.
- Galanti, M., Fanelli, D., Traytak, S. D., and Piazza, F. (2016). Theory of diffusion-influenced reactions in complex geometries (vol 18, pg 15950, 2016). *Physical Chemistry Chemical Physics*, 18(26):17757–17757.
- Gameiro, D., Perez-Perez, M., Perez-Rodriguez, G., Monteiro, G., Azevedo, N. F., and Lourenco, A. (2016). Computational resources and strategies to construct single-molecule metabolic models of microbial cells. *Briefings in Bioinformatics*, 17(5):863–876.
- Gillespie, D. T. (1977). Exact Stochastic Simulation of Coupled Chemical-Reactions. *Journal of Physical Chemistry*, 81(25):2340–2361.
- Goehring, N. W., Trong, P. K., Bois, J. S., Chowdhury, D., Nicola, E. M., Hyman, A. A., and Grill, S. W. (2011). Polarization of PAR Proteins by Advective Triggering of a Pattern-Forming System. *Science*, 334(6059):1137–1141.
- Gopich, I. V. and Szabo, A. (2002). Kinetics of reversible diffusion influenced reactions: The self-consistent relaxation time approximation. *The Journal of Chemical Physics*, 117(2):507–517.
- Gopich, I. V. and Szabo, A. (2018). Theory of Diffusion-Influenced Reaction Networks. *The Journal of Physical Chemistry B*, 122(49):11338–11354.
- Gorter, E. and Grendel, F. (1925). On bimolecular layers of lipoids on the chromocytes of the blood. *Journal of Experimental Medicine*, 41(4):439–444.
- Grima, R. (2010). Intrinsic biochemical noise in crowded intracellular conditions. *Journal of Chemical Physics*, 132(18).

- Grima, R. and Schnell, S. (2006a). How Reaction Kinetics with Time-Dependent Rate Coefficients Differs from Generalized Mass Action. *ChemPhysChem*, 7(7):1422–1424.
- Grima, R. and Schnell, S. (2006b). A systematic investigation of the rate laws valid in intracellular environments. *Biophysical Chemistry*, 124(1):1–10.
- Grima, R. and Schnell, S. (2007). A mesoscopic simulation approach for modeling intracellular reactions. *Journal of Statistical Physics*, 128(1-2):139–164.
- Grima, R. and Schnell, S. (2008). Modelling reaction kinetics inside cells. *Essays in Biochemistry: Systems Biology, Vol 45*, 45:41–56.
- Grima, R., Yaliraki, S. N., and Barahona, M. (2010). Crowding-Induced Anisotropic Transport Modulates Reaction Kinetics in Nanoscale Porous Media. *Journal of Physical Chemistry B*, 114(16):5380–5385.
- Grundke, E. W. and Henderson, D. (1972). Distribution functions of multi-component fluid mixtures of hard spheres. *Molecular Physics*, 24(2):269–281. [\\_eprint: https://doi.org/10.1080/00268977200101431](https://doi.org/10.1080/00268977200101431).
- Hall, D. and Minton, A. P. (2003). Macromolecular crowding: Qualitative and semiquantitative successes, quantitative challenges. *Biochim Biophys Acta*, 1649(2):127–39.
- Hancock, R. (2004). Internal organisation of the nucleus: Assembly of compartments by macromolecular crowding and the nuclear matrix model. *Biology of the Cell*, 96(8):595–601.
- Hansen, N., Muller, S. D., and Koumoutsakos, P. (2003). Reducing the time complexity of the de-randomized evolution strategy with covariance matrix adaptation (CMA-ES). *Evolutionary Computation*, 11(1):1–18.
- Hasnain, S., McClendon, C. L., Hsu, M. T., Jacobson, M. P., and Bandyopadhyay, P. (2014). A New Coarse-Grained Model for E. coli Cytoplasm: Accurate Calculation of the Diffusion Coefficient of Proteins and Observation of Anomalous Diffusion. *Plos One*, 9(9).
- Hattne, J., Fange, D., and Elf, J. (2005). Stochastic reaction-diffusion simulation with MesoRD. *Bioinformatics*, 21(12):2923–2924.
- Hatzimanikatis, V. (1999). Nonlinear metabolic control analysis. *Metab Eng*, 1(1):75–87.
- Hatzimanikatis, V. and Bailey, J. E. (1996). MCA has more to say. *Journal of Theoretical Biology*, 182(3):233–242.

## Bibliography

---

- Hatzimanikatis, V. and Bailey, J. E. (1997). Effects of spatiotemporal variations on metabolic control: Approximate analysis using (log)linear kinetic models. *Biotechnol Bioeng*, 54(2):91–104.
- Heineken, F. G., Tsuchiya, H. M., and Aris, R. (1967). On the mathematical status of the pseudo-steady state hypothesis of biochemical kinetics. *Mathematical Biosciences*, 1(1):95–113.
- Heinrich, R. and Rapoport, T. A. (1974). A Linear Steady-State Treatment of Enzymatic Chains. *European Journal of Biochemistry*, 42(1):89–95. \_eprint: <https://febs.onlinelibrary.wiley.com/doi/pdf/10.1111/j.1432-1033.1974.tb03318.x>.
- Heinrich, R. and Schuster, S. (1996). *The Regulation of Cellular Systems*. Chapman & Hall, New York ; London.
- Helfand, E., Reiss, H., Frisch, H. L., and Lebowitz, J. L. (1960). Scaled Particle Theory of Fluids. *Journal of Chemical Physics*, 33(5):1379–1385.
- Henry, C. S., Broadbelt, L. J., and Hatzimanikatis, V. (2007). Thermodynamics-based metabolic flux analysis. *Biophys J*, 92(5):1792–805.
- Henry, C. S., Jankowski, M., Broadbelt, L. J., and Hatzimanikatis, V. (2005). Analysis of free energy change and thermodynamic feasibility in a genome scale metabolic model. *Abstracts of Papers of the American Chemical Society*, 229:U193–U193.
- Hindmarsh, A. C., Brown, P. N., Grant, K. E., Lee, S. L., Serban, R., Shumaker, D. E., and Woodward, C. S. (2005). SUNDIALS: Suite of nonlinear and differential/algebraic equation solvers. *Acm Transactions on Mathematical Software*, 31(3):363–396.
- Hiragami-Hamada, K., Shinmyozu, K., Hamada, D., Tatsu, Y., Uegaki, K., Fujiwara, S., and Nakayama, J. (2011). N-Terminal Phosphorylation of HP1 alpha Promotes Its Chromatin Binding. *Molecular and Cellular Biology*, 31(6):1186–1200.
- Hiragami-Hamada, K., Soeroes, S., Nikolov, M., Wilkins, B., Kreuz, S., Chen, C., De La Rosa-Velazquez, I. A., Zenn, H. M., Kost, N., Pohl, W., Chernev, A., Schwarzer, D., Jenuwein, T., Lorincz, M., Zimmermann, B., Walla, P. J., Neumann, H., Baubec, T., Urlaub, H., and Fischle, W. (2016). Dynamic and flexible H3K9me3 bridging via HP1 beta dimerization establishes a plastic state of condensed chromatin. *Nature Communications*, 7.
- Hirokawa, N. and Takemura, R. (2005). Molecular motors and mechanisms of directional transport in neurons. *Nature Reviews Neuroscience*, 6(3):201–214.



- Hofling, F. and Franosch, T. (2013). Anomalous transport in the crowded world of biological cells. *Reports on Progress in Physics*, 76(4).
- Hofstee, B. H. J. (1959). Non-Inverted Versus Inverted Plots in Enzyme Kinetics. *Nature*, 184(4695):1296–1298.
- Holehouse, A. S. and Pappu, R. V. (2018). Functional Implications of Intracellular Phase Transitions. *Biochemistry*, 57(17):2415–2423.
- Hyman, A. A., Weber, C. A., and Julicher, F. (2014). Liquid-liquid phase separation in biology. *Annu Rev Cell Dev Biol*, 30:39–58.
- Igel, C., Hansen, N., and Roth, S. (2007). Covariance matrix adaptation for multi-objective optimization. *Evolutionary Computation*, 15(1):1–28.
- Imhof, A. and Dhont, J. K. G. (1995). Long-time self-diffusion in binary colloidal hard-sphere dispersions. *Physical Review E*, 52(6):6344–6357.
- Incardona, P., Leo, A., Zaluzhnyi, Y., Ramaswamy, R., and Sbalzarini, I. F. (2019). OpenFPM: A scalable open framework for particle and particle-mesh codes on parallel computers. *Computer Physics Communications*, 241:155–177.
- Ivancic, V. A., Krasinski, C. A., Zheng, Q., Meservier, R. J., Spratt, D. E., and Lazo, N. D. (2018). Enzyme kinetics from circular dichroism of insulin reveals mechanistic insights into the regulation of insulin-degrading enzyme. *Biosci Rep*, 38(6).
- Jenuwein, T. and Allis, C. D. (2001). Translating the histone code. *Science (New York, N.Y.)*, 293(5532):1074–1080.
- Jeon, J.-H., Javanainen, M., Martinez-Seara, H., Metzler, R., and Vattulainen, I. (2016). Protein Crowding in Lipid Bilayers Gives Rise to Non-Gaussian Anomalous Lateral Diffusion of Phospholipids and Proteins. *Physical Review X*, 6(2).
- Johansson, F. et al. (2013). *Mpmath: A Python Library for Arbitrary-Precision Floating-Point Arithmetic (Version 0.18)*.
- Jones, S. and Thornton, J. M. (1996). Principles of protein-protein interactions. *Proceedings of the National Academy of Sciences of the United States of America*, 93(1):13–20.
- Kacser, H. and Burns, J. A. (1973). The control of flux. *Symposia of the Society for Experimental Biology*, 27:65–104.

## Bibliography

---

- Kalwarczyk, T., Tabaka, M., and Holyst, R. (2012). Biologistics–diffusion coefficients for complete proteome of *Escherichia coli*. *Bioinformatics*, 28(22):2971–8.
- Kharchenko, P. V., Alekseyenko, A. A., Schwartz, Y. B., Minoda, A., Riddle, N. C., Ernst, J., Sabo, P. J., Larschan, E., Gorchakov, A. A., Gu, T. T., Linder-Basso, D., Plachetka, A., Shanower, G., Tolstorukov, M. Y., Luquette, L. J., Xi, R. B., Jung, Y. L., Park, R. W., Bishop, E. P., Canfield, T. K., Sandstrom, R., Thurman, R. E., MacAlpine, D. M., Stamatoyannopoulos, J. A., Kellis, M., Elgin, S. C. R., Kuroda, M. I., Pirrotta, V., Karpen, G. H., and Park, P. J. (2011). Comprehensive analysis of the chromatin landscape in *Drosophila melanogaster*. *Nature*, 471(7339):480–+.
- Khodayari, A., Zomorodi, A. R., Liao, J. C., and Maranas, C. D. (2014). A kinetic model of *Escherichia coli* core metabolism satisfying multiple sets of mutant flux data. *Metabolic Engineering*, 25:50–62.
- Kholodenko, B. N. and Westerhoff, H. V. (1993). Metabolic channelling and control of the flux. *FEBS letters*, 320(1):71–74.
- Kilic, S., Bachmann, A. L., Bryan, L. C., and Fierz, B. (2015). Multivalency governs HP1alpha association dynamics with the silent chromatin state. *Nat Commun*, 6:7313.
- Kim, M., Lee, S., and Kim, J. H. (2014). Concentration effects on the rates of irreversible diffusion-influenced reactions. *Journal of Chemical Physics*, 141(8).
- Kim, Y. C. and Mittal, J. (2013). Crowding Induced Entropy-Enthalpy Compensation in Protein Association Equilibria. *Physical Review Letters*, 110(20):208102.
- Kinjo, A. R. and Takada, S. (2002). Effects of macromolecular crowding on protein folding and aggregation studied by density functional theory: Statics. *Phys Rev E Stat Nonlin Soft Matter Phys*, 66(3 Pt 1):031911.
- Kirkwood, J. G. (1935). Statistical Mechanics of Fluid Mixtures. *The Journal of Chemical Physics*, 3(5):300–313.
- Klann, M. T., Lapin, A., and Reuss, M. (2011). Agent-based simulation of reactions in the crowded and structured intracellular environment: Influence of mobility and location of the reactants. *Bmc Systems Biology*, 5.
- Klosin, A., Oltsch, F., Harmon, T., Honigmann, A., Jülicher, F., Hyman, A. A., and Zechner, C. (2020). Phase separation provides a mechanism to reduce noise in cells. *Science*, 367(6476):464–468.

- Kornberg, T. B. and Tabata, T. (1993). Segmentation of the *Drosophila* embryo. *Current Opinion in Genetics & Development*, 3(4):585–593.
- Kouzarides, T. (2007). Chromatin modifications and their function. *Cell*, 128(4):693–705.
- Kruse, K., Joanny, J. F., Jülicher, F., Prost, J., and Sekimoto, K. (2004). Asters, Vortices, and Rotating Spirals in Active Gels of Polar Filaments. *Physical Review Letters*, 92(7):078101.
- Kruse, K., Joanny, J. F., Jülicher, F., Prost, J., and Sekimoto, K. (2005). Generic theory of active polar gels: A paradigm for cytoskeletal dynamics. *The European Physical Journal E*, 16(1):5–16.
- Larson, A. G., Elnatan, D., Keenen, M. M., Trnka, M. J., Johnston, J. B., Burlingame, A. L., Agard, D. A., Redding, S., and Narlikar, G. J. (2017). Liquid droplet formation by HP1 $\alpha$  suggests a role for phase separation in heterochromatin. *Nature*, 547(7662):236–240.
- Larson, M. G. and Bengzon, F. (2013). *The Finite Element Method: Theory, Implementation, and Applications*. Texts in Computational Science and Engineering. Springer-Verlag, Berlin Heidelberg.
- Lebowitz, J. L. (1964). Exact Solution of Generalized Percus-Yevick Equation for a Mixture of Hard Spheres. *Physical Review*, 133(4A):A895–A899.
- Lebowitz, J. L., Helfand, E., and Praestgaard, E. (1965). Scaled Particle Theory of Fluid Mixtures. *Journal of Chemical Physics*, 43(3):774–+.
- Lebowitz, J. L. and Rowlinson, J. S. (1964). Thermodynamic Properties of Mixtures of Hard Spheres. *The Journal of Chemical Physics*, 41(1):133–138.
- Leegwater, J. A. and Szamel, G. (1992). Dynamical properties of hard-sphere suspensions. *Physical Review A*, 46(8):4999–5011.
- Leonard, P. J., Henderson, D., and Barker, J. A. (1971). Calculation of the radial distribution function of hard-sphere mixtures in the Percus-Yevick approximation. *Molecular Physics*, 21(1):107–111.
- Li, G.-W., Berg, O. G., and Elf, J. (2009). Effects of macromolecular crowding and DNA looping on gene regulation kinetics. *Nature Physics*, 5(4):294–297.
- Lombard, J. (2014). Once upon a time the cell membranes: 175 years of cell boundary research. *Biology Direct*, 9(1):32.

## Bibliography

---

- Luger, K., Dechassa, M. L., and Tremethick, D. J. (2012). New insights into nucleosome and chromatin structure: An ordered state or a disordered affair? *Nature Reviews Molecular Cell Biology*, 13(7):436–447.
- Maarleveld, T. R., Olivier, B. G., and Bruggeman, F. J. (2013). StochPy: A Comprehensive, User-Friendly Tool for Simulating Stochastic Biological Processes. *Plos One*, 8(11).
- MacDonald, T. S. C., Price, W. S., Astumian, R. D., and Beves, J. E. (2019). Enhanced Diffusion of Molecular Catalysts is Due to Convection. *Angewandte Chemie*, 131(52):19040–19043.   
\_eprint: <https://onlinelibrary.wiley.com/doi/pdf/10.1002/ange.201910968>.
- Maison, C. and Almouzni, G. (2004). HP1 and the dynamics of heterochromatin maintenance. *Nature Reviews. Molecular Cell Biology*, 5(4):296–304.
- Mayer, J., Khairy, K., and Howard, J. (2010). Drawing an elephant with four complex parameters. *American Journal of Physics*, 78(6):648–649.
- McGuffee, S. R. and Elcock, A. H. (2010). Diffusion, crowding & protein stability in a dynamic molecular model of the bacterial cytoplasm. *PLoS Comput Biol*, 6(3):e1000694.
- Michaelis, L. and Menten, M. L. (1913). The kinetics of the inversion effect. *Biochemische Zeitschrift*, 49:333–369.
- Mikhlin, S. G. (1964). *Variational Methods in Mathematical Physics*. Pergamon Press; [distributed by Macmillan, New York, Oxford; New York. OCLC: 567691266.
- Miller, T. C. R., Simon, B., Rybin, V., Grötsch, H., Curtet, S., Khochbin, S., Carlomagno, T., and Müller, C. W. (2016). A bromodomain-DNA interaction facilitates acetylation-dependent bivalent nucleosome recognition by the BET protein BRDT. *Nature Communications*, 7:13855.
- Minton, A. P. (1981). Excluded Volume as a Determinant of Macromolecular Structure and Reactivity. *Abstracts of Papers of the American Chemical Society*, 182(Aug):32–&.
- Minton, A. P. (2001). The influence of macromolecular crowding and macromolecular confinement on biochemical reactions in physiological media. *Journal of Biological Chemistry*, 276(14):10577–10580.
- Miskovic, L., Tokic, M., Savoglidis, G., and Hatzimanikatis, V. (2019). Control Theory Concepts for Modeling Uncertainty in Enzyme Kinetics of Biochemical Networks. *Industrial & Engineering Chemistry Research*, 58(30):13544–13554.

- Monod, J. (1949). The Growth of Bacterial Cultures. *Annual Review of Microbiology*, 3(1):371–394. [\\_eprint: https://doi.org/10.1146/annurev.mi.03.100149.002103](https://doi.org/10.1146/annurev.mi.03.100149.002103).
- Morelli, M. J. and ten Wolde, P. R. (2008). Reaction Brownian dynamics and the effect of spatial fluctuations on the gain of a push-pull network. *Journal of Chemical Physics*, 129(5).
- Mourao, M., Kreitman, D., and Schnell, S. (2014). Unravelling the impact of obstacles in diffusion and kinetics of an enzyme catalysed reaction. *Phys Chem Chem Phys*, 16(10):4492–503.
- Müller, K. P., Erdel, F., Caudron-Herger, M., Marth, C., Fodor, B. D., Richter, M., Scaranaro, M., Beaudouin, J., Wachsmuth, M., and Rippe, K. (2009). Multiscale analysis of dynamics and interactions of heterochromatin protein 1 by fluorescence fluctuation microscopy. *Biophysical Journal*, 97(11):2876–2885.
- Müller, M. M., Fierz, B., Bittova, L., Liszczak, G., and Muir, T. W. (2016). A two-state activation mechanism controls the histone methyltransferase Suv39h1. *Nature Chemical Biology*, 12(3):188–193.
- Nishibuchi, G., Machida, S., Osakabe, A., Murakoshi, H., Hiragami-Hamada, K., Nakagawa, R., Fischle, W., Nishimura, Y., Kurumizaka, H., Tagami, H., and Nakayama, J. (2014). N-terminal phosphorylation of HP1 alpha increases its nucleosome-binding specificity. *Nucleic Acids Research*, 42(20):12498–12511.
- Northrup, S. H., Allison, S. A., and Mccammon, J. A. (1984). Brownian Dynamics Simulation of Diffusion-Influenced Bimolecular Reactions. *Journal of Chemical Physics*, 80(4):1517–1526.
- Öcal, K., Grima, R., and Sanguinetti, G. (2019). Parameter estimation for biochemical reaction networks using Wasserstein distances. *Journal of Physics A: Mathematical and Theoretical*, 53(3):034002.
- Orth, J. D., Thiele, I., and Palsson, B. O. (2010). What is flux balance analysis? *Nat Biotechnol*, 28(3):245–8.
- Pastor, I., Pitulice, L., Balcells, C., Vilaseca, E., Madurga, S., Isvoran, A., Cascante, M., and Mas, F. (2014). Effect of crowding by Dextran in enzymatic reactions. *Biophysical Chemistry*, 185:8–13.
- Pastor, I., Vilaseca, E., Madurga, S., Garcés, J. L., Cascante, M., and Mas, F. (2011). Effect of Crowding by Dextran on the Hydrolysis of N-Succinyl-L-phenyl-Ala-p-nitroanilide Catalyzed by  $\alpha$ -Chymotrypsin. *The Journal of Physical Chemistry B*, 115(5):1115–1121.

## Bibliography

---

- Patel, A., Lee, H. O., Jawerth, L., Maharana, S., Jahnel, M., Hein, M. Y., Stoynov, S., Mahamid, J., Saha, S., Franzmann, T. M., Pozniakovski, A., Poser, I., Maghelli, N., Royer, L. A., Weigert, M., Myers, E. W., Grill, S., Drechsel, D., Hyman, A. A., and Alberti, S. (2015). A Liquid-to-Solid Phase Transition of the ALS Protein FUS Accelerated by Disease Mutation. *Cell*, 162(5):1066–1077.
- Pauly, M. and Keegstra, K. (2016). Biosynthesis of the Plant Cell Wall Matrix Polysaccharide Xyloglucan. *Annual Review of Plant Biology*, 67(1):235–259. \_eprint: <https://doi.org/10.1146/annurev-arplant-043015-112222>.
- Peppin, S. S. L. (2019). Theory of tracer diffusion in concentrated hard-sphere suspensions. *Journal of Fluid Mechanics*, 870:1105–1126.
- Perry, R. H. (1973). *Chemical Engineers' Handbook*. MacGraw-Hill Handbooks. McGraw-Hill, New York [etc.], fifth edition.
- Pieters, B. J. G. E., van Eldijk, M. B., Nolte, R. J. M., and Mecinović, J. (2015). Natural supramolecular protein assemblies. *Chemical Society Reviews*, 45(1):24–39.
- Pivovarov, A. S., Calahorra, E., and Walker, R. J. (2018). Na<sup>+</sup>/K<sup>+</sup>-pump and neurotransmitter membrane receptors. *Invertebrate neuroscience: IN*, 19(1):1.
- Poggi, C. G. and Slade, K. M. (2015). Macromolecular crowding and the steady-state kinetics of malate dehydrogenase. *Biochemistry*, 54(2):260–7.
- Prost, J., Jülicher, F., and Joanny, J.-F. (2015). Active gel physics. *Nature Physics*, 11(2):111–117.
- Reder, C. (1988). Metabolic Control-Theory - a Structural Approach. *Journal of Theoretical Biology*, 135(2):175–201.
- Rhee, H. S., Bataille, A. R., Zhang, L., and Pugh, B. F. (2014). Subnucleosomal structures and nucleosome asymmetry across a genome. *Cell*, 159(6):1377–1388.
- Rivas, G. and Minton, A. P. (2018). Toward an understanding of biochemical equilibria within living cells. *Biophys Rev*, 10(2):241–253.
- Robyt, J. F. (2001). Polysaccharides: Energy Storage. In *eLS*. American Cancer Society. \_eprint: <https://onlinelibrary.wiley.com/doi/pdf/10.1038/npg.els.0000700>.
- Salvy, P. and Hatzimanikatis, V. (2020). The ETFL formulation allows multi-omics integration in thermodynamics-compliant metabolism and expression models. *Nature Communications*, 11(1):1–17.

- Sánchez, B. J., Zhang, C., Nilsson, A., Lahtvee, P.-J., Kerkhoven, E. J., and Nielsen, J. (2017). Improving the phenotype predictions of a yeast genome-scale metabolic model by incorporating enzymatic constraints. *Molecular Systems Biology*, 13(8):935.
- Schnell, S. and Turner, T. E. (2004). Reaction kinetics in intracellular environments with macromolecular crowding: Simulations and rate laws. *Progress in Biophysics & Molecular Biology*, 85(2-3):235–260.
- Schomburg, I., Chang, A., Placzek, S., Söhngen, C., Rother, M., Lang, M., Munaretto, C., Ulas, S., Stelzer, M., Grote, A., Scheer, M., and Schomburg, D. (2013). BRENDA in 2013: Integrated reactions, kinetic data, enzyme function data, improved disease classification: New options and contents in BRENDA. *Nucleic Acids Research*, 41(Database issue):D764–772.
- Schoneberg, J. and Noe, F. (2013). ReaDDy - A Software for Particle-Based Reaction-Diffusion Dynamics in Crowded Cellular Environments. *Plos One*, 8(9).
- Schuster, S. (1999). Use and Limitations of Modular Metabolic Control Analysis in Medicine and Biotechnology. *Metabolic Engineering*, 1(3):232–242.
- Seabold, S. and Perktold, J. (2010). Statsmodels: Econometric and statistical modeling with python. *9th Python in Science Conference*.
- Šegota, S. and Težak, D. (2006). Spontaneous formation of vesicles. *Advances in Colloid and Interface Science*, 121(1-3):51–75.
- Serban, R. and Hindmash, A. C. (2005). CVODES, the sensitivity-enabled ODE solver in SUNDIALS. *Proceedings of the ASME International Design Engineering Technical Conferences and Computers and Information in Engineering Conference, Vol 6, Pts A-C*, pages 257–269.
- Shannon, C. E. (1948). A mathematical theory of communication. *The Bell System Technical Journal*, 27(3):379–423.
- Shaw, A. S., Chalupny, J., Whitney, J. A., Hammond, C., Amrein, K. E., Kavathas, P., Sefton, B. M., and Rose, J. K. (1990). Short related sequences in the cytoplasmic domains of CD4 and CD8 mediate binding to the amino-terminal domain of the p56lck tyrosine protein kinase. *Molecular and Cellular Biology*, 10(5):1853–1862.
- Shim, A. R., Almassalha, L., Matsuda, H., Nap, R., and Szleifer, I. (2017). Dynamic modeling shows long-term gene expression is highly dependent on macromolecular crowding. *Faseb Journal*, 31.
- Singh, P. B. (2010). HP1 proteins—what is the essential interaction? *Genetika*, 46(10):1424–1429.

## Bibliography

---

- Skou, J. C. (1957). The influence of some cations on an adenosine triphosphatase from peripheral nerves. *Biochimica Et Biophysica Acta*, 23(2):394–401.
- Smith, E. and Shilatifard, A. (2010). The Chromatin Signaling Pathway: Diverse Mechanisms of Recruitment of Histone-Modifying Enzymes and Varied Biological Outcomes. *Molecular Cell*, 40(5):689–701.
- Smith, S., Cianci, C., and Grima, R. (2017). Macromolecular crowding directs the motion of small molecules inside cells. *Journal of the Royal Society Interface*, 14(131).
- Smith, S. and Grima, R. (2017). Fast simulation of Brownian dynamics in a crowded environment. *Journal of Chemical Physics*, 146(2).
- Smith, W. R. (1992). *Chemical Reaction Equilibrium Analysis : Theory and Algorithms /*. Wiley, New York .:
- Smoluchowski, M. (1927). Versuch einer mathematischen Theorie der Koagulationskinetik kolloider Lösungen. *Pisma Mariana Smoluchowskiego*, 2(1):595–639.
- Son, J., Shen, S. S., Margueron, R., and Reinberg, D. (2013). Nucleosome-binding activities within JARID2 and EZH1 regulate the function of PRC2 on chromatin. *Genes & Development*, 27(24):2663–2677.
- Spitzer, J. and Poolman, B. (2013). How crowded is the prokaryotic cytoplasm? *Febs Letters*, 587(14):2094–2098.
- Stoeger, T., Battich, N., and Pelkmans, L. (2016). Passive Noise Filtering by Cellular Compartmentalization. *Cell*, 164(6):1151–1161.
- Strating, P. (1999). Brownian dynamics simulation of a hard-sphere suspension. *Physical Review E*, 59(2):2175–2187.
- Strom, A. R., Emelyanov, A. V., Mir, M., Fyodorov, D. V., Darzacq, X., and Karpen, G. H. (2017). Phase separation drives heterochromatin domain formation. *Nature*, 547(7662):241–245.
- Sturrock, M. (2016). Stochastic reaction-diffusion algorithms for macromolecular crowding. *Phys Biol*, 13(3):036010.
- Su, X., Ditlev, J. A., Hui, E., Xing, W., Banjade, S., Okrut, J., King, D. S., Taunton, J., Rosen, M. K., and Vale, R. D. (2016). Phase separation of signaling molecules promotes T cell receptor signal transduction. *Science (New York, N.Y.)*, 352(6285):595–599.



- Sumner, J. B. (1935). Enzymes. *Annual Review of Biochemistry*, 4(1):37–58. \_eprint: <https://doi.org/10.1146/annurev.bi.04.070135.000345>.
- Sweeney, H. L. and Houdusse, A. (2010). Structural and Functional Insights into the Myosin Motor Mechanism. *Annual Review of Biophysics*, 39(1):539–557. \_eprint: <https://doi.org/10.1146/annurev.biophys.050708.133751>.
- Szabo, A. (1989). Theory of diffusion-influenced fluorescence quenching. *The Journal of Physical Chemistry*, 93(19):6929–6939.
- Szabo, A. (1991). Theoretical approaches to reversible diffusion-influenced reactions: Monomer–excimer kinetics. *The Journal of Chemical Physics*, 95(4):2481–2490.
- Szabo, A. and Zhou, H.-X. (2012). Role of diffusion in the kinetics of reversible enzyme-catalyzed reactions. *Bulletin of the Korean Chemical Society*, 33(3):925–928.
- Tabita, F. R., Hanson, T. E., Li, H., Satagopan, S., Singh, J., and Chan, S. (2007). Function, Structure, and Evolution of the RubisCO-Like Proteins and Their RubisCO Homologs. *Microbiology and Molecular Biology Reviews*, 71(4):576–599.
- Tang, Y. and Lu, B. C.-Y. (1995). Improved expressions for the radial distribution function of hard spheres. *The Journal of Chemical Physics*, 103(17):7463–7470.
- Thiru, A., Nietlispach, D., Mott, H. R., Okuwaki, M., Lyon, D., Nielsen, P. R., Hirshberg, M., Verreault, A., Murzina, N. V., and Laue, E. D. (2004). Structural basis of HP1/PXVXL motif peptide interactions and HP1 localisation to heterochromatin. *The EMBO journal*, 23(3):489–499.
- Tokic, M., Hatzimanikatis, V., and Miskovic, L. (2020). Large-scale kinetic metabolic models of *Pseudomonas putida* KT2440 for consistent design of metabolic engineering strategies. *Biotechnology for Biofuels*, 13(1):33.
- Trovato, F. and Tozzini, V. (2014). Diffusion within the cytoplasm: A mesoscale model of interacting macromolecules. *Biophys J*, 107(11):2579–91.
- Vallino, J. J. and Stephanopoulos, G. (1993). Metabolic flux distributions in *Corynebacterium glutamicum* during growth and lysine overproduction. *Biotechnology and Bioengineering*, 41(6):633–646. \_eprint: <https://onlinelibrary.wiley.com/doi/pdf/10.1002/bit.260410606>.
- van den Berg, B., Ellis, R. J., and Dobson, C. M. (1999). Effects of macromolecular crowding on protein folding and aggregation. *EMBO J*, 18(24):6927–33.

## Bibliography

---

- van Zon, J. S. and ten Wolde, P. R. (2005). Green's-function reaction dynamics: A particle-based approach for simulating biochemical networks in time and space. *Journal of Chemical Physics*, 123(23).
- Varma, A. and Palsson, B. O. (1993a). Metabolic Capabilities of Escherichia coli: I. Synthesis of Biosynthetic Precursors and Cofactors. *Journal of Theoretical Biology*, 165(4):477–502.
- Varma, A. and Palsson, B. O. (1993b). Metabolic Capabilities of Escherichia coli II. Optimal Growth Patterns. *Journal of Theoretical Biology*, 165(4):503–522.
- Verger, R., Mieras, M. C., and de Haas, G. H. (1973). Action of phospholipase A at interfaces. *The Journal of Biological Chemistry*, 248(11):4023–4034.
- Vijaykumar, A., ten Wolde, P. R., and Bolhuis, P. G. (2017). The magnitude of the intrinsic rate constant: How deep can association reactions be in the diffusion limited regime? *Journal of Chemical Physics*, 147(18).
- Vinothkumar, K. R. and Henderson, R. (2010). Structures of membrane proteins. *Quarterly Reviews of Biophysics*, 43(1):65–158.
- Visco, I., Hoege, C., Hyman, A. A., and Schwille, P. (2016). In vitro Reconstitution of a Membrane Switch Mechanism for the Polarity Protein LGL. *Journal of Molecular Biology*, 428(24):4828–4842.
- Voigt, P., LeRoy, G., Drury, W. J., Zee, B. M., Son, J., Beck, D. B., Young, N. L., Garcia, B. A., and Reinberg, D. (2012). Asymmetrically modified nucleosomes. *Cell*, 151(1):181–193.
- Wang, L. and Hatzimanikatis, V. (2006a). Metabolic engineering under uncertainty-II: Analysis of yeast metabolism. *Metab Eng*, 8(2):142–59.
- Wang, L. Q., Birol, I., and Hatzimanikatis, V. (2004). Metabolic control analysis under uncertainty: Framework development and case studies. *Biophysical Journal*, 87(6):3750–3763.
- Wang, L. Q. and Hatzimanikatis, V. (2006b). Metabolic engineering under uncertainty. I: Framework development. *Metabolic Engineering*, 8(2):133–141.
- Wang, M. C. and Uhlenbeck, G. E. (1945). On the Theory of the Brownian Motion-II. *Reviews of Modern Physics*, 17(2-3):323–342.
- Wang, Y., Guo, L., Golding, I., Cox, E. C., and Ong, N. P. (2009). Quantitative transcription factor binding kinetics at the single-molecule level. *Biophysical Journal*, 96(2):609–620.

- Watterson, S., Guerriero, M. L., Blanc, M., Mazein, A., Loewe, L., Robertson, K. A., Gibbs, H., Shui, G. H., Wenk, M. R., Hillston, J., and Ghazal, P. (2013). A model of flux regulation in the cholesterol biosynthesis pathway: Immune mediated graduated flux reduction versus statin-like led stepped flux reduction. *Biochimie*, 95(3):613–621.
- Weilandt, D. R. and Hatzimanikatis, V. (2019). Particle-Based Simulation Reveals Macromolecular Crowding Effects on the Michaelis-Menten Mechanism. *Biophysical Journal*, 117(2):355–368.
- Westerhoff, H. V. and Welch, G. R. (1992). Enzyme Organization and the Direction of Metabolic Flow - Physicochemical Considerations. *Current Topics in Cellular Regulation*, 33:361–390.
- Wilson, D. B., Byrne, H., and Bruna, M. (2018). Reactions, diffusion, and volume exclusion in a conserved system of interacting particles. *Physical Review E*, 97(6).
- Wittig, U., Kania, R., Golebiewski, M., Rey, M., Shi, L., Jong, L., Alga, E., Weidemann, A., Sauer-Danzwith, H., Mir, S., Krebs, O., Bittkowski, M., Wetsch, E., Rojas, I., and Müller, W. (2012). SABIO-RK—database for biochemical reaction kinetics. *Nucleic Acids Research*, 40(Database issue):D790–D796.
- Woodcock, C. L. and Ghosh, R. P. (2010). Chromatin higher-order structure and dynamics. *Cold Spring Harbor Perspectives in Biology*, 2(5):a000596.
- Xu, G. H., Zhao, J. J., Cheng, K., Wu, Q., Liu, X. L., Liu, M. L., and Li, C. G. (2017). The Effects of Macromolecular Crowding on Calmodulin Structure and Function. *Chemistry-a European Journal*, 23(28):6736–6740.
- Xu, M., Ross, J. L., Valdez, L., and Sen, A. (2019). Direct Single Molecule Imaging of Enhanced Enzyme Diffusion. *Physical Review Letters*, 123(12):128101.
- Yadav, J. K. (2013). Macromolecular Crowding Enhances Catalytic Efficiency and Stability of alpha-Amylase. *ISRN Biotechnol*, 2013:737805.
- Yogurtcu, O. N. and Johnson, M. E. (2015). Theory of bi-molecular association dynamics in 2D for accurate model and experimental parameterization of binding rates. *The Journal of Chemical Physics*, 143(8):084117.
- Yuste, S. B., Santos, A., and López de Haro, M. (1998). Structure of multi-component hard-sphere mixtures. *The Journal of Chemical Physics*, 108(9):3683–3693.
- Zhang, Y. and Hess, H. (2019). Enhanced Diffusion of Catalytically Active Enzymes. *ACS Central Science*, 5(6):939–948.

## Bibliography

---

- Zhao, Y. H., Abraham, M. H., and Zissimos, A. M. (2003). Fast calculation of van der Waals volume as a sum of atomic and bond contributions and its application to drug compounds. *J Org Chem*, 68(19):7368–73.
- Zhen, C. Y., Tatavosian, R., Huynh, T. N., Duc, H. N., Das, R., Kokotovic, M., Grimm, J. B., Lavis, L. D., Lee, J., Mejia, F. J., Li, Y., Yao, T., and Ren, X. (2016). Live-cell single-molecule tracking reveals co-recognition of H3K27me3 and DNA targets polycomb Cbx7-PRC1 to chromatin. *eLife*, 5.
- Zhou, H.-X. (2009). Crowding Effects of Membrane Proteins. *The journal of physical chemistry. B*, 113(23):7995–8005.
- Zhou, H. X. and Qin, S. (2013). Simulation and Modeling of Crowding Effects on the Thermodynamic and Kinetic Properties of Proteins with Atomic Details. *Biophys Rev*, 5(2):207–215.
- Zhou, H. X., Rivas, G., and Minton, A. P. (2008). Macromolecular crowding and confinement: Biochemical, biophysical, and potential physiological consequences. *Annu Rev Biophys*, 37:375–97.
- Zimmerman, S. B. and Trach, S. O. (1991). Estimation of Macromolecule Concentrations and Excluded Volume Effects for the Cytoplasm of Escherichia-Coli. *Journal of Molecular Biology*, 222(3):599–620.

# Daniel Weilandt

## Resumé

Ch. de la Ripe 2

1131 Tolochenaz – Switzerland

☎ (+41) 77 40 10 827

✉ daniel.weilandt@epfl.ch

🌐 [www.linkedin.com/in/daniel-weilandt](http://www.linkedin.com/in/daniel-weilandt)

### Education

- 2016–now **Doctor of Science**, *École Polytechnique Fédérale de Lausanne*, Switzerland.  
Doctoral School of Chemistry and Chemical Engineering
- 2013–2016 **Master of Science**, *Albert-Ludwigs University*, Freiburg, Germany.  
Microsystems Engineering
- 2010–2013 **Bachelor of Engineering**, *Cooperative State University*, Stuttgart, Germany.  
Mechanical Engineering

### Professional experience

- 2016–now **Doctoral assistant**, *École Polytechnique Fédérale de Lausanne*, Switzerland.  
Laboratory of Computational Systems Biotechnology under the supervision of Prof. Vassily Hatzimanikatis. Development of new computational methods to assess the effects of spatial confinement on metabolic networks.
- 2015–2016 **Research assistant**, *Albert-Ludwigs University*, Freiburg, Germany.  
Master thesis: "Dissipative Particle Dynamics simulations of colloids near membranes".  
Software development for a particle simulation software <http://symppler.org/>.
- 2013–2014 **Student employee**, *Daimler AG*, Stuttgart.  
Programming, analysis of measurement data, support in developing a software in the loop simulation environment.
- 2010–2013 **Cooperative student**, *Daimler AG*, Stuttgart (Germany) / Portland (OR, USA).  
Cooperative studies at the *DHBW* Stuttgart and on-the-job training within the Daimler AG.  
Two internships and Bachelor thesis in the R&D department for manual transmissions and an internship in advanced engineering at Daimler Trucks North America LLC.

### Teaching experience

- 2016–now **Teaching assistant**, *École Polytechnique Fédérale de Lausanne*.  
*Principles and Applications of Systems Biology*. Supervised by Prof. Vassily Hatzimanikatis.  
*Bioreactor Modeling and Simulation*. Supervised by Prof. Vassily Hatzimanikatis.  
*Numerical Methods in Chemistry*. Supervised by Dr. Ljubisa Miskovic.
- 2015 **Guest lecture**, *University of Applied Sciences Juvaneum*, Graz.  
Two-day seminar within the module: *Advanced Design and Mechanical Components*.
- 2013–2016 **Freelance trainer**, *Altair GmbH*, Germany.  
Software trainer for structural analysis and optimization with HyperWorks in the *Altair* academic program.

---

## Personal Skills

- Languages** German, mother tongue  
English, fully fluent  
French, basic knowledge
- Software** Expert in programming Python, C++, Matlab, and Julia. Basic skills in other languages like HTML, CSS and Java.  
Expert skills in  $\text{\LaTeX}$  and MS-Office
- Methods** Deterministic and stochastic modelling of biochemical reaction networks  
Spatial modelling of biochemical reactions using particle simulation methods such as Brownian reaction dynamics and grid based methods based on the reaction diffusion master equation and the stochastic simulation algorithm  
Application of global optimization methods such as GA and CMA-ES  
Formulation of constraint based optimization problems, e.g. LP and MILP
- Management** Experience in mentoring Bachelor and Master students.  
Passionate about teaching and sharing knowledge

---

## Publications

\* these authors contributed equally

Bryan, L. C.\*, **Weilandt, D. R.\***, Bachmann, A. L., Kilic, S., Lechner, C. C., Odermatt, P. D., Fanter, G. E., Georgeon, S., Hatzimanikatis, V., Fierz, B. "Single-molecule kinetic analysis of HP1-chromatin binding reveals a dynamic network of histone modification and DNA interactions." *Nucleic acids research* 45.18 (2017): 10504-1051

**Weilandt, D. R.**, Hatzimanikatis, V., "Particle-based simulation reveals macromolecular crowding effects on the Michaelis-Menten mechanism." *Biophysical Journal* 117.2 (2019): 355-368

---

## Cover Art



*Biophysical Journal* 117.2 (2019):

"Abstract illustration of the interior of an *E. coli* cell, highlighting the high macromolecular content of the cell. The zoom-in shows an enzymatic reaction in this crowded environment."